NASA TECHNICAL MEMORANDUM

NASA TM X-3548

NASA TM X-3548

EFFECT OF ROTOR WAKE ON AERODYNAMIC CHARACTERISTICS OF A 1/6-SCALE MODEL OF THE ROTOR SYSTEMS RESEARCH AIRCRAFT

Raymond E. Mineck

Langley Directorate,
U.S. Army Air Mobility R&D Laboratory

Langley Research Center
Hampton, Va. 23665

NATIONAL AERONAUTICS AND SPACE ADMINISTRATION · WASHINGTON, D. C. · SEPTEMBER 1977

1. Report No.	2. Government Accession No.	3. Recipient's Catalog No.
NASA TM X-3548		

4. Title and Subtitle	5. Report Date
EFFECT OF ROTOR WAKE ON AERODYNAMIC CHARACTERISTICS OF A 1/6-SCALE MODEL OF THE ROTOR SYSTEMS RESEARCH AIRCRAFT	September 1977
	6. Performing Organization Code
7. Author(s)	8. Performing Organization Report No.
Raymond E. Mineck	L-11515
	10. Work Unit No.
9. Performing Organization Name and Address	505-10-21-05
Langley Directorate, USAAMRDL NASA Langley Research Center Hampton, VA 23665	11. Contract or Grant No.
	13. Type of Report and Period Covered
12. Sponsoring Agency Name and Address	Technical Memorandum
National Aeronautics and Space Administration Washington, DC 20546 and U.S. Army Air Mobility R&D Laboratory Moffett Field, CA 94035	14. Army Project No. 1L161102AH45

15. Supplementary Notes

16. Abstract

A wind-tunnel investigation was conducted to determine the effect of the main-rotor wake on the aerodynamic characteristics of the rotor systems research aircraft (RSRA). A 1/6-scale model with a 4-blade articulated rotor was used to determine the effect of the rotor wake for the compound configuration. Data were obtained over a range of angles of attack, angles of sideslip, auxiliary engine thrusts, rotor collective pitch angles, and rotor tip-path plane angles for several main-rotor advance ratios. Separate results are presented for the forces and moments on the airframe, the wing, and the tail.

The results of this investigation indicate that the aerodynamic characteristics are significantly changed by the rotor wake. The rotor wake increases the longitudinal static stability, the effective dihedral, and the lateral static stability of the airframe. The rotor induces a downwash on the wing. This downwash decreases the wing lift and increases the drag. The asymmetrical rotor wake induces a differential lift across the wing and a subsequent rolling moment. These rotor induced effects on the wing become smaller with increasing forward speed.

17. Key Words (Suggested by Author(s))	18. Distribution Statement
Rotor systems research aircraft (RSRA) Compound helicopters Rotor wake	Unclassified - Unlimited Subject Category 02

19. Security Classif. (of this report)	20. Security Classif. (of this page)	21. No. of Pages	22. Price*
Unclassified	Unclassified	118	$5.50

*For sale by the National Technical Information Service, Springfield, Virginia 22161

EFFECT OF ROTOR WAKE ON AERODYNAMIC CHARACTERISTICS OF A 1/6-SCALE MODEL OF THE ROTOR SYSTEMS RESEARCH AIRCRAFT

Raymond E. Mineck*
Langley Research Center

SUMMARY

A wind-tunnel investigation was conducted to determine the effect of the main-rotor wake on the aerodynamic characteristics of the rotor systems research aircraft (RSRA). A 1/6-scale model with a 4-blade articulated rotor was used to determine the effect of the rotor wake for the compound configuration. Data were obtained over a range of angles of attack, angles of sideslip, auxiliary engine thrusts, rotor collective pitch angles, and rotor tip-path plane angles for several main-rotor advance ratios. Separate results are presented for the forces and moments on the airframe, the wing, and the tail.

The results of this investigation indicate that the aerodynamic characteristics are significantly changed by the rotor wake. The rotor wake increases the longitudinal static stability, the effective dihedral, and the lateral static stability of the airframe. The rotor induces a downwash on the wing. This downwash decreases the wing lift and increases the drag. The asymmetrical rotor wake induces a differential lift across the wing and a subsequent rolling moment. These rotor induced effects on the wing become smaller with increasing forward speed.

INTRODUCTION

Rotor wake effects complicate the prediction of helicopter stability and performance and often must be determined experimentally. This complication is especially true for rotor systems research aircraft (RSRA) developed by NASA and the U.S. Army. The RSRA is a unique compound helicopter designed to obtain accurate data for evaluating advanced rotor systems and for developing and verifying rotorcraft theories. The RSRA is equipped with a variable-incidence wing to load and unload the rotor, auxiliary thrust engines and drag brakes to cover a wide range of rotor propulsive force, and fly-by-wire controls to evaluate advanced flight-control systems. The RSRA can be flown as a fixed-wing aircraft, a pure helicopter, or a compound helicopter. Additional details of the RSRA may be found in reference 1.

---

*Langley Directorate, U.S. Army Air Mobility R&D Laboratory.

Four phases of wind-tunnel tests were conducted to determine and refine the aerodynamic characteristics of the RSRA. The aerodynamic characteristics of the original configuration were obtained in the Phase I tests. The results, presented in reference 2, indicated potential longitudinal- and lateral-stability problems with the rotors removed. The problems were associated with the tail configuration and with the modeling of the auxiliary thrust engines. The tail configuration was refined in Phase II to provide the desired stability levels with the rotors removed (see ref. 2). Two tail configurations were developed: one for the pure helicopter and another for the compound helicopter. The available engine simulators did not permit the auxiliary thrust engine nacelles and pylons to be properly scaled. Therefore, the auxiliary thrust engine support pylons were refined in Phase III by using geometrically scaled nacelles. The results, presented in reference 3, indicated that the longitudinal stability with the rotors removed is greater for the scaled engine nacelles. However, none of these investigations considered the rotor wake effects. Therefore, the Phase IV tests included measurements with and without a main rotor. Data were obtained for loads on the airframe, the wing, the tail, and the rotor. The results are presented in reference 4.

This report analyzes the data of reference 4 to determine the effect of the rotor wake on the compound configuration. The effect of the rotor wake on the airframe was determined by comparing the rotor-off data with the rotor-on data with the rotor forces and moments removed. The effect of the rotor lift on the wing and the tail was measured directly. Data were obtained at several forward speeds for two wing incidence/flap deflection settings. The angle of attack, the angle of sideslip, the rotor collective pitch, the rotor tip-path plane angle, and the auxiliary engine thrust were varied from estimated trim conditions

SYMBOLS

The units used for the physical quantities defined in this paper are given in the International System of Units (SI) and parenthetically in U.S. Customary Units. Conversion factors for the SI system are presented in reference 5. All measurements and calculations were made in U.S. Customary Units.

The longitudinal data on the airframe, wing, and tail are resolved in the stability-axis system and the lateral data in the body-axis system. (See figs. 1(a) and 1(b).) The moment reference center for the airframe, wing, and tail was located 3.81 cm (1.50 in.) behind and 35.14 cm (13.83 in.) below the center of the rotor hub, which is the nominal aft center of gravity of the RSRA. Sign conventions used for the control angles of the rotor and aerodynamic surfaces are shown in figures 1(c) and 1(d).

A area of main rotor, πR^2, 7.791 m^2 (83.86 ft^2)

a_0 main-rotor coning angle, deg

a_{1s} first-harmonic rotor longitudinal flapping angle in shaft-axis system, deg

b wing span, 2.286 m (90.0 in.)

b_R number of blades, 4

b_{1s} first-harmonic rotor lateral flapping angle in shaft-axis system, deg

c_R main-rotor blade chord, 10.77 cm (4.24 in.)

$\bar{c}$ wing mean geometric chord, 0.423 m (16.67 in.)

C_D airframe drag coefficient, $\frac{D}{q_\infty S}$

$C_{D,w}$ wing drag coefficient, $\frac{D_w}{q_\infty S}$

C_L airframe lift coefficient, $\frac{L}{q_\infty S}$

$C_{L,R}/\sigma$ rotor lift coefficient to solidity ratio, $\frac{L_R}{\rho_\infty A V_T^2 \sigma}$

$C_{L,t}$ tail lift coefficient, $\frac{L_t}{q_\infty S_t}$

$C_{L,w}$ wing lift coefficient, $\frac{L_w}{q_\infty S}$

C_{L_α} airframe lift-curve slope, $\frac{dC_L}{d\alpha}$, deg^{-1}

C_m airframe pitching-moment coefficient, $\frac{M_Y}{q_\infty S \bar{c}}$

$C_{m_{C_L}}$ airframe longitudinal-stability parameter, $\frac{dC_m}{dC_L}$

$C_{m,t}$ tail pitching-moment coefficient, $\frac{M_{Y,t}}{q_\infty S \bar{c}}$

$C_{m,w}$ wing pitching-moment coefficient, $\frac{M_{Y,w}}{q_\infty S \bar{c}}$

C_n airframe yawing-moment coefficient, $\frac{M_Z}{q_\infty S b}$

C_{n_β} airframe directional-stability parameter, $\frac{dC_n}{d\beta}$, deg^{-1}

$C_{T,J}$ auxiliary jet engine thrust coefficient, $\frac{T_J}{q_\infty S}$

C_Y airframe side-force coefficient, $\frac{F_Y}{q_\infty S}$

C_l airframe rolling-moment coefficient, $\frac{M_X}{q_\infty Sb}$

$C_{l,w}$ wing rolling-moment coefficient, $\frac{M_{X,w}}{q_\infty Sb}$

C_{l_β} airframe effective dihedral parameter, $\frac{dC_l}{d\beta}$, deg^{-1}

D airframe drag, N (lbf)

D_w wing drag, N (lbf)

d rotor diameter, 3.149 m (10.333 ft)

F_Y airframe side force, N (lbf)

g acceleration due to gravity $\left(1g = 9.8\ m/sec^2\ (32.2\ ft/sec^2)\right)$

h height of rotor hub above tunnel floor, m (ft)

i_t horizontal-tail incidence with respect to fuselage reference line, deg

i_w wing incidence with respect to fuselage reference line, deg

k constant of proportionality

L airframe lift, N (lbf)

L_R rotor lift, N (lbf)

L_T total lift on vehicle, $L + L_R$, N (lbf)

L_t tail lift, N (lbf)

L_w wing lift, N (lbf)

M_X airframe rolling moment, N-m (lbf-in.)

$M_{X,w}$ wing rolling moment, N-m (lbf-in.)

M_Y airframe pitching moment, N-m (lbf-in.)

$M_{Y,t}$ tail pitching moment, N-m (lbf-in.)

$M_{Y,w}$ wing pitching moment, N-m (lbf-in.)

M_Z airframe yawing moment, N-m (lbf-in.)

q_∞ free-stream dynamic pressure, Pa (lbf/ft^2)

R main-rotor radius, 1.575 m (5.167 ft)

S	wing area, 0.954 m^2 (10.272 ft^2)
S_t	tail area, compound tail, 0.274 m^2 (2.93 ft^2)
T_J	auxiliary jet engine thrust, N (lbf)
V_T	rotor tip speed, ΩR, m/sec (ft/sec)
V_∞	free-stream velocity, m/sec (ft/sec)
z	distance from rotor to wing, m (ft)
α	fuselage angle of attack, deg
β	fuselage angle of sideslip, deg
$\Delta\alpha$	change in wing aerodynamic angle of attack due to rotor lift, deg
$\frac{\partial C_{l,w}}{\partial C_{L,R}/\sigma}$	wing asymmetrical loading parameter
δ_f	flap deflection, deg
δ_3	rotor pitch-flap coupling angle, deg
θ_c	main-rotor collective pitch angle, deg
μ	advance ratio, $\frac{V_\infty}{V_T}$
ρ_∞	free-stream density, kg/m^3 ($slugs/ft^3$)
σ	rotor solidity, $\frac{b_R c_R}{\pi R}$
ψ	main-rotor azimuth angle, deg
Ω	main-rotor rotational speed, rad/sec

MODEL AND APPARATUS

The general rotor model system (GRMS) developed at Langley Research Center was used in this wind-tunnel investigation. The external configuration was a 1/6-scale model of the RSRA. A photograph of the model installed in the tunnel is shown in figure 2. Detailed three-view and internal component layouts of the model are presented in figures 3(a) and 3(b). The geometric characteristics of the model components may be found in table I.

The various components of the model, such as the wing, the auxiliary thrust engine nacelles, and the horizontal and vertical tails were removable to simulate the RSRA in either the helicopter or compound helicopter configuration.

The compound configuration had the wing and the auxiliary thrust engine nacelles. Transition grit was used on the wings, the horizontal tail, the vertical tail, and the nose of the model. No. 80 carborundum grit was located at the 5-percent chord or 3.81 cm (1.50 in.) (whichever was greater) from the leading edge on both the upper and lower surfaces.

The variable-incidence wing, which pivoted about the three-quarter root chord, could be set at -9°, 0°, and 7.5° incidence. The partial-span, single-slotted flaps were deflectable to 30°. For these tests, end plates were attached at the wing roots in lieu of wing-root-to-fuselage sealing to allow the wing to be mounted on a six-component, strain-gage balance. By having the wing mounted on this balance, wing loads were measured directly.

The empennage was attached to the GRMS main structure with a strain-gage balance to measure the empennage loads directly. (See fig. 3(b).) Loads on the empennage included loads on the vertical and horizontal tails and on the tail cone from fuselage station 231.78 cm (91.25 in.) aft. (See fig. 3(c).) At that point, a 0.3-cm (0.11-in.) gap between the tail cone and the rest of the fuselage skin allowed clearance for balance deflections.

Details of the horizontal and vertical tails may be found in figure 3(c). A combination tail consisting of a small upper horizontal tail with an area of 0.046 m^2 (0.48 ft^2) and the lower horizontal tail with an area of 0.228 m^2 (2.45 ft^2) was used for the compound helicopter.

Two removable auxiliary thrust engine nacelles were mounted on the fuselage. Each nacelle contained a removable fan used to simulate the jet thrust. These fans, nacelles, and engine pylon fairings were the same as those used in reference 3. The engine pylon fairings were the modified minimum fairings shown in figure 3(d).

Each fan had a stator and a rotor. A ring with turbine blades was attached to the rotor. Dry, high-pressure air, directed onto the turbine blades, drove the fan to produce thrust. Each nacelle had one static-pressure orifice and three total-pressure probes mounted in the fan exit of each engine. The three total-pressure probes were manifolded together. A pressure transducer was used to measure the difference between the total pressure and the static pressure to obtain an average reference dynamic pressure at the exit. The exit velocity was low enough to insure that no correction for compressibility was necessary. This reference exit dynamic pressure was used to calibrate the engine thrust. During the investigation, the fans were removed from the nacelles for a "flow-through" mode as an engine thrust calibration reference condition.

The main rotor used in this investigation had four untwisted blades, a solidity of 0.087, a diameter of 3.149 m (10.333 ft), a root cutout of 33 percent, and a mast tilt of 0°. This main rotor differs from the RSRA rotor which has 5 blades, -8° of twist, a solidity of 0.077, and a mast tilt of 2°.

The rotor hub was fully articulated. Pitch-horn geometry was variable to allow for changes in pitch-flap coupling angle δ_3. Cyclic and collective pitch on the blades were controlled with a swashplate driven by remotely

controlled actuators. The flapping and lagging hinge offsets were 0.076 m (0.25 ft). The main-rotor hub was located 1.27 cm (0.5 in.) above the scale location for the RSRA.

The rotor was driven by two 67-kW (90-hp) electric motors driving a common transmission. These variable-speed electric motors were water cooled through an umbilical from an external water source. The transmission was cooled and lubricated by oil pumped into the model through the umbilical. The entire rotor-transmission-motor system was mounted on a six-component strain-gage balance within the model to measure the rotor forces and moments.

The model was mounted on the airframe balance supported by a special sting model support system. This system positions the airframe balance near the center of the test section during pitch, roll, and yaw excursions. High-pressure air is piped into the model from an air plenum mounted directly below the airframe balance. (See fig. 3(b).) This plenum is fed by an air line running through the center of the sting. A coiled section in the air line minimizes pressure effects and mechanical tare effects on the airframe balance.

TEST CONDITIONS AND CORRECTIONS

This investigation was conducted in the Langley V/STOL tunnel, which is a closed-return atmospheric tunnel. The tunnel test section measures 4.42 m (14.50 ft) high by 6.63 m (21.75 ft) wide. Tunnel wind speed was varied from 0 to 130 knots. All testing was done with the model close to the center line of the test section. This position corresponds to an h/d of 0.92.

The auxiliary engine thrust was calibrated at several forward speeds with the model at 0° angle of attack. The thrust was measured as the difference in drag of the airframe with the fans installed and removed. This thrust was calibrated as a function of the free-stream dynamic pressure and the fan-exit dynamic pressure. After calibration, the engine thrusts were balanced for zero yawing moment at maximum engine thrust and zero tunnel speed.

Testing of the model was carried out with the rotor off and rotor on. For the rotor-off testing, the angle of attack and the angle of sideslip were varied to establish a baseline for rotor effects. The fuselage was tested with several combinations of the tail, wing, and jets to determine the aerodynamic contribution of each component. When the jets were installed, several different thrust levels were tested. The lower horizontal-tail incidence was set to 0° for most of the rotor-off testing.

For rotor-on testing, angle of attack, angle of sideslip, main-rotor collective pitch angle, tip-path plane angle, and auxiliary engine thrust were varied from estimated trim conditions. The main-rotor controls were fixed for angle of attack, angle of sideslip, and auxiliary engine thrust variations; the main-rotor controls were varied to maintain a tip-path plane angle for the collective pitch angle variations. The trim conditions were obtained for 1g level

flight from an analytical simulation program. The nominal rotor speed was 1290 rpm which is equivalent to a tip speed of 213 m/sec (700 ft/sec). Two values of δ_3 were tested: -27.7° and -2.0°.

The compound helicopter was tested with two wing incidence/flap deflection settings: $0^\circ/0^\circ$ and $7.5^\circ/30^\circ$. Each wing incidence/flap deflection setting was tested at one or more values of rotor lift. The different values may be identified by the ratio of airframe lift to total lift L/L_T. The lower horizontal-tail incidence was set to 3° for rotor-on testing with the compound horizontal tail except for the tests with the wing and the auxiliary thrust nacelles off.

The rotor wake effect was defined as the difference between the rotor-off data and the rotor-on data with the rotor forces and moments removed. The removal of the rotor forces and moments was possible because the rotor forces and moments were measured directly by the rotor balance. The test conditions for the rotor-on data were not always the same as those for the rotor-off data. The horizontal-tail incidence, angle of attack, and auxiliary engine thrust coefficient differed for the rotor-on and rotor-off tests. Since the rotor-off test conditions bracketed the rotor-on test conditions, a linear interpolation was used to adjust the rotor-off results.

Several corrections were made in the data reduction procedure to compensate for certain identifiable mechanical and aerodynamic interferences. Correction factors were obtained for: (1) the effect of the air line crossing the airframe balance, (2) the effect of the model support system, and (3) the effects of the wind-tunnel walls. The effect of the air line was determined by loading the balance statically with the air line attached and the air line off. The effect of the model support system was caused by the asymmetrical configuration of the support system and the proximity of the sting to the bottom of the fuselage. The effect of the asymmetrical configuration was determined by rotating the joints of the model support system to maintain a constant model attitude. Then, variations of model loads could be attributed to tunnel flow alterations caused by joint position. The effect of the proximity of the sting was estimated from unpublished data from Phase III tests. In these tests, the model was post-mounted. Data were taken with and without a large tube attached in the same position as the sting mount of Phase IV. The wall effects were accounted for by using the methods described in reference 6.

PRESENTATION OF RESULTS

The results of the wind-tunnel investigation have been presented in coefficient form. The longitudinal data on the airframe, wing, and tail are resolved in the stability-axis system and the lateral data in the body-axis system. (See figs. 1(a) and 1(b).) The moment reference center for the airframe, wing, and tail was located 3.81 cm (1.50 in.) behind and 35.14 cm (13.83 in.) below the center of the rotor hub which is the nominal aft center of gravity (c.g.) of the RSRA. The aft center-of-gravity location was chosen because the stability was most critical there. Because of the aft center of gravity,

the trim attitude was generally nose up, and the rotor did not provide any propulsive force. The results are presented as follows:

DISCUSSION OF RESULTS

The direct rotor loads measured on the rotor balance have been removed from the airframe rotor-on data, and the results are discussed in the following sections.

Airframe Data With Direct Rotor Effects Removed

Longitudinal data.- The variation of the airframe longitudinal aerodynamic characteristics with angle of attack from an estimated trim condition is presented in figures 4 and 5 for several advance ratios. As the advance ratio decreases, the angle of attack required to maintain a given lift coefficient increases. This effect usually occurs when the downwash from the rotor decreases the aerodynamic angle of attack of the wing. (This effect is discussed in more detail in the section entitled "Effect of the Rotor on the Wing.") There is only a slight reduction in the lift-curve slope at the lower advance ratios and higher angles of attack. The data for the various advance ratios differ in drag primarily because of the difference in auxiliary engine thrust coefficient. The difference in static longitudinal stability $C_{m_{C_L}}$ results from the different thrust coefficients and the rotor wake effect.

The variation of the airframe aerodynamic characteristics with rotor collective pitch angle from an estimated trim condition is presented in figures 6 and 7 for several advance ratios. Increasing the rotor collective pitch

angle decreases the airframe lift. This effect is expected because increasing the collective pitch angle increases both the rotor lift and the downwash on the airframe. The rate of decrease of the airframe lift with collective pitch angle decreases as the advance ratio increases because the momentum of the rotor wake becomes smaller in comparison with the momentum of the free stream. In general, increasing the collective pitch angle slightly reduced the airframe drag for positive tip-path plane angles of attack $\left(\alpha + a_{1_s}\right)$ and increased the airframe drag for negative tip-path plane angles of attack.

The variation of the airframe longitudinal aerodynamic characteristics with the rotor longitudinal flapping from an estimated trim condition is presented in figures 8 and 9. In general, decreasing the longitudinal flapping decreases the airframe lift and provides a nose-up increment to the pitching moment. The airframe drag was not significantly changed for the range of flapping angles tested.

The auxiliary engine thrust has a direct as well as an induced effect on the airframe longitudinal aerodynamics. The component of the thrust vector in the lift and drag direction provides the direct effect on lift and drag (see fig. 3(a)). The $0.07\bar{1}c$ displacement of the thrust line from the center of gravity causes the direct effect on pitching moment. In addition, the jet exhaust can induce a change in the lift, drag, and pitching-moment contributions from the wing, the tail, and the fuselage. The induced effect on lift and drag was small; on the other hand, the measured induced effect on the pitching moment was significant. The effect of engine thrust on the pitching moment of the airframe, wing, and tail is presented in figure 10. The results show that the jet exhaust induces a significant change in the pitching-moment contribution of the tail, but has little or no effect on the pitching-moment contribution of the wing.

Lateral data.- The variation of the airframe lateral aerodynamic characteristics with angle of sideslip is presented in figures 11 and 12. The results indicate that the lateral forces and moments would not be zero at 0° sideslip because of the induced effect of the rotor wake and asymmetries in the model. The two wing panels had a slightly different incidence, and the flap contours were not identical. In general, the directional stability $\left(\text{positive } C_{n_\beta}\right)$ increases, and the effective dihedral $\left(\text{negative } C_{l_\beta}\right)$ decreases as the advance ratio increases. However, for the test conditions used in this investigation, the angle of attack decreased as the advance ratio increased. Reference 4 contains results showing that the directional stability increased and that the effective dihedral decreased as the angle of attack decreased. Therefore, at least some of these effects result from changes in angle of attack for each advance ratio.

The variation of the lateral aerodynamic characteristics of the airframe with rotor lateral flapping is presented in figures 13 and 14. Increasing the lateral flapping made the side force and the yawing moment more negative. The flapping changes the direction of the wake and thereby induces a sidewash on the airframe. The sidewash then produces the change in the side force and yawing moment. There is no significant change in the rolling moment.

Comparison of Rotor-Off Results With Rotor-On Results

With Rotor Effect Removed

Longitudinal data.- The results from reference 4 indicated that the longitudinal-stability parameter $C_{m_{C_L}}$ was dependent on the lift coefficient and the auxiliary engine thrust coefficient. The effects of both of these parameters are present in the results of figures 4 and 5. Therefore, the comparison of rotor-off and rotor-on measurements for similar lift coefficients and engine thrust coefficients have been presented in figures 15 and 16. The rotor-off data have been adjusted to account for the different test conditions. Both C_{L_α} and $C_{m_{C_L}}$ were computed from measured data at the rotor-on trim lift coefficient; these results are presented in table II. It should be noted that the rotor-off results would be different if they were computed at the rotor-on trim angle of attack instead of at the rotor-on trim lift coefficient.

For the $0^\circ/0^\circ$ wing incidence/flap deflection setting, the lift-curve slope is significantly less for the rotor-on than for the rotor-off data. The lift-curve slope is generally smaller at the lower advance ratios. The rotor wake increases the static longitudinal stability. For the $7.5^\circ/30^\circ$ wing incidence/flap deflection setting, the results for the lift-curve slope are similar to those for the $0^\circ/0^\circ$ wing incidence/flap deflection setting. However, the static longitudinal stability for the rotor on and rotor off is much smaller for the $7.5^\circ/30^\circ$ setting than for the $0^\circ/0^\circ$ setting. Also, the rotor wake sometimes decreases the static longitudinal stability slightly.

Lateral data.- The results from reference 4 indicated that the lateral-directional stability $\left(\text{positive } C_{n_\beta}\right)$ and the effective dihedral $\left(\text{negative } C_{l_\beta}\right)$ were dependent on the trim angle of attack and auxiliary engine thrust coefficient. The effect of both of these parameters is present in the results of figures 11 and 12. Therefore, the comparisons of the rotor-on and rotor-off measurements for similar angles of attack and engine thrust coefficients are presented in figures 17 and 18. The rotor-off data have not been adjusted for the difference in lower horizontal-tail incidence. However, this effect should be very small. The results have been interpolated to the proper angle of attack and engine thrust coefficient. Both C_{n_β} and C_{l_β} were computed at 0° sideslip, and the results are presented in table III. The results from table III indicate that, in general, the rotor wake increases both the effective dihedral and the directional stability. None of the configurations tested showed unstable effective dihedral or directional stability.

Effect of the Rotor on the Wing

The placement of a lifting wing near a lifting rotor leads to a mutual interference. Theoretical analysis of the interference is an extremely difficult problem. An experimental analysis providing some insight into the effect of the rotor wake on the wing is presented in the following section. Here a procedure similar to that in reference 7 is used.

Longitudinal data.- The rotor wake induces a change in the aerodynamic angle of attack of the wing. To determine this change, the rotor lift was varied by changing either the collective pitch angle or the longitudinal rotor flapping angle. These results are presented in figures 19 and 20. Generally, when collective pitch angle is varied (fig. 19), the slopes of the wing lift against rotor lift curves are parallel at a given advance ratio and wing incidence/flap deflection setting. Increasing the rotor lift decreases the wing lift because the rotor downwash decreases the wing aerodynamic angle of attack. Increasing the rotor lift also increases the wing drag. These two effects decrease the wing-lift-to-drag ratio. These effects decrease as forward speed increases. These trends are the same as those in reference 7. Similar trends are exhibited when the rotor lift is varied by changing the longitudinal flapping angle (fig. 20).

The results from figure 19 have been cross-plotted in figure 21 at constant values of rotor lift coefficient. As expected, increasing the rotor lift decreases the wing aerodynamic angle of attack and lift. The change in wing angle of attack $\Delta\alpha$ was computed for each advance ratio and wing incidence, and the results are presented in figure 22.

Reference 7 suggested that

$$\Delta\alpha = k \frac{\sigma}{2\mu^2} \left(\frac{C_{L,R}}{\sigma} \right) \times 57.3$$

where k is a proportionality constant. However, for large changes in wing aerodynamic angle of attack (small advance ratios), the small angle assumption should not be used, and the expression should be rewritten

$$\tan \Delta\alpha = k \frac{\sigma}{2\mu^2} \left(\frac{C_{L,R}}{\sigma} \right)$$

This equation has been plotted in figure 22 for several values of k. For the $7.5^\circ/30^\circ$ and the $0^\circ/0^\circ$ wing incidence/flap deflection settings, average values are $k = 0.52$ and $k = 0.25$, respectively. These values are much smaller than the $k = 0.94$ that would be predicted from reference 7 for a z/d of 0.17. If the results from the rotor longitudinal flapping sweeps (fig. 20) were used to compute k, the results would be even smaller. The reason for these discrepancies is not known at the present. Possible explanations are that the auxiliary thrust nacelles and fairings may block the downwash on the wing, or the engine wake may distort the rotor wake.

Lateral data.- The momentum distribution of the rotor wake is not the same on the advancing side of the rotor disk as on the retreating side. This difference in induced downwash induces a rolling moment due to the differential lift on the two wing panels. The variation of the rolling moment on the wing with rotor lift is presented in figures 23 and 24 for the same conditions as those

in figures 19 and 20. Increasing the rotor lift increases the rolling moment on the wing. For the collective pitch angle variation, the slopes are usually parallel for a given advance ratio and wing incidence/flap deflection setting. The slope decreases with increasing advance ratio. For the longitudinal flapping angle variation, the slopes are very nearly parallel for both wing incidence/flap deflection settings at a given advance ratio. These slopes, presented in figure 25, are significantly less for the collective pitch angle variation. The rolling-moment coefficient and the rotor-lift coefficient have been nondimensionalized by different velocities. Multiplying the slope by the advance ratio squared tends to give parallel results.

Effect of the Rotor on the Tail

The rotor should induce a downwash on the tail as it does on the wing. To verify this downwash effect, the model was tested with the compound tail but without the wing or the auxiliary thrust engines. The rotor lift was varied by changing the rotor collective pitch angle; the results are presented in figure 26. As expected, an increase in the rotor lift induces a download on the tail, and the effect diminishes with increasing advance ratio.

SUMMARY OF RESULTS

The effect of a rotor wake on a 1/6-scale model of the rotor systems research aircraft may be summarized as follows:

1. The rotor wake increases the longitudinal static stability of the airframe. The increase is larger for the $0^\circ/0^\circ$ wing incidence/flap deflection setting than for the $7.5^\circ/30^\circ$ setting.

2. Generally, the rotor wake increases the effective dihedral and the static directional stability of the airframe.

3. The rotor wake induces a downwash on the wing which decreases the wing lift-drag ratio. The effect decreases with increasing forward speed.

4. The rotor wake induces a downwash on the tail, and a download on the tail results.

5. The rotor induces an asymmetrical loading on the wing and a subsequent rolling moment. This effect decreases with increasing advance ratio.

Langley Research Center
National Aeronautics and Space Administration
Hampton, VA 23665
June 2, 1977

REFERENCES

1. Linden, A. W.; and Hellyar, M. W.: The Rotor Systems Research Aircraft - A Flying Wind Tunnel. AIAA Paper No. 74-1277, Oct. 1974.

2. Flemming, R.; and Ruddell, A.: RSRA Sixth Scale Wind Tunnel Test - Final Report. Doc. No. SER-72011 (Contract NAS1-13000), Sikorsky Aircraft Div., United Aircraft Corp., Dec. 4, 1974. (Available as NASA CR-144964.)

3. Mineck, Raymond E.; Freeman, Carl E.; and Hassell, James L., Jr.: Aerodynamic Characteristics of a 1/6-Scale Model of the Rotor Systems Research Aircraft With the Rotors Removed. NASA TN D-8198, 1976.

4. Mineck, Raymond E.; and Freeman, Carl E.: Aerodynamic Characteristics of a 1/6-Scale Powered Model of the Rotor Systems Research Aircraft. NASA TM X-3489, 1977.

5. Mechtly, E. A.: The International System of Units - Physical Constants and Conversion Factors (Second Revision). NASA SP-7012, 1973.

6. Heyson, Harry H.: Use of Superposition in Digital Computers To Obtain Wind-Tunnel Interference Factors for Arbitrary Configurations, With Particular Reference to V/STOL Models. NASA TR R-302, 1969.

7. Bain, Lawrence J.; and Landgrebe, Anton J.: Investigation of Compound Helicopter Aerodynamic Interference Effects. USAAVLABS Tech. Rep. 67-44, U.S. Army, Nov. 1967. (Available from DDC as AD 665 427.)

TABLE I.- CHARACTERISTICS OF GENERAL ROTOR MODEL SYSTEM AND ROTOR

Fuselage:	
Length, m (ft)	3.057 (10.03)
Frontal area, m^2 (ft^2)	0.172 (1.85)
Wing:	
Airfoil section	NACA 63_2415
Area, m^2 (ft^2)	0.954 (10.272)
Span, m (ft)	2.286 (7.500)
Mean geometric chord, m (ft)	0.423 (1.40)
Aspect ratio	5.52
Taper ratio	0.66
Sweep of 25-percent chord line, deg	3.0
Dihedral, deg	7.0
Flaps (each):	
Area, m^2 (ft^2)	0.0743 (0.80)
Span, percent of wing semispan	49.0
Chord, percent of local wing chord	33.0
Vertical stabilizer:	
Airfoil section	NACA 0015
Area, m^2 (ft^2)	0.294 (3.164)
Span, m (ft)	0.813 (2.67)
Aspect ratio	2.25
Root chord, m (ft)	0.476 (1.56)
Compound upper horizontal tail:	
Airfoil section	NACA 0015
Area, m^2 (ft^2)	0.046 (0.48)
Span, m (ft)	0.44 (1.43)
Aspect ratio	4.29
Root chord, m (ft)	0.128 (0.42)
Taper ratio	0.60
Compound lower horizontal tail:	
Airfoil section	NACA 0015
Area, m^2 (ft^2)	0.228 (2.45)
Span, m (ft)	1.14 (3.75)
Aspect ratio	5.75
Root chord, m (ft)	0.197 (0.65)
Taper ratio	1.00
Main rotor:	
Number of blades	4
Airfoil section	NACA 0012
Radius, m (ft)	1.575 (5.167)
Chord, m (ft)	0.108 (0.353)
Twist, deg	0
Solidity	0.087
Disk area, m^2 (ft^2)	7.791 (83.86)
Hinge offset, m (ft)	0.076 (0.25)
Pitch-flap coupling, deg	-27.6 or -2.0
Blade Lock number	10.3

TABLE II.- MEASURED VALUES FOR C_{L_α} AND $C_{m_{C_L}}$

μ	Figure	C_L	C_{L_α} (deg^{-1})		$C_{m_{C_L}}$	
			Rotor off	Rotor on	Rotor off	Rotor on
$i_w = 0^\circ$; $\delta_f = 0^\circ$						
0.14	15(a)	0.46	0.088	0.064	-0.103	-0.333
0.19	15(b)	0.47	0.089	0.061	-0.055	-0.146
		.51	.089	.066	-.052	-.230
		.25	.083	.074	-.078	-.135
0.27	15(c)	0.55	0.089	0.079	-0.063	-0.104
		.45	.091	.074	-.050	-.099
		.52	.092	.065	-.051	-.138
		.17	.089	.077	-.069	-.080
0.32	15(d)	0.40	0.089	0.077	-0.060	-0.110
		.14	.091	.073	-.078	-.093
$i_w = 7.5^\circ$; $\delta_f = 30^\circ$						
0.14	16(a)	0.87	0.089	0.055	-0.079	-0.091
		.85	.092	.058	-.052	-.051
0.20	16(b)	1.35	0.079	0.059	-0.068	-0.155
		1.30	.078	.064	-.090	-.084
		.92	.090	.065	-.079	-.213
		.89	.092	.063	-.039	-.088
		1.24	.085	.051	-.016	-.043
0.27	16(c)	1.20	0.081	0.069	-0.073	-0.109
		1.10	.090	.070	-.005	-.006
		1.12	.094	.070	-.011	.011
		1.10	.094	.067	-.011	.011
		.88	.092	.072	-.088	-.206
		.81	.094	.075	-.070	-.074
		.81	.094	.075	-.070	-.101
0.32	16(d)	1.06	0.088	0.078	0.022	0.009
		.77	.096	.077	-.040	-.040

TABLE III.- MEASURED VALUES FOR C_{l_β} AND C_{n_β}

μ	Figure	α, deg	C_{l_β} (deg^{-1})		C_{n_β} (deg^{-1})	
			Rotor off	Rotor on	Rotor off	Rotor on
$i_w = 0^\circ$; $\delta_f = 0^\circ$						
0.14	17(a)	9.1	-0.0006	-0.0012	0.0008	0.0031
0.19	17(b)	7.6 4.6	-0.0003 -.0002	-0.0007 -.0008	0.0005 .0012	0.0015 .0026
0.27	17(c)	4.8 4.5 5.2 1.4	-0.0004 -.0003	 -0.0005 -.0005 -.0005	0.0010 .0016	 0.0023 .0016 .0022
0.32	17(d)	3.1 1.3	-0.0004 -.0001	-0.0002 -.0003	0.0013 .0017	0.0021 .0025
$i_w = 7.5^\circ$; $\delta_f = 30^\circ$						
0.20	18(a)	3.3 3.4 -.5	 -0.0010 -.0011	-0.0012 -.0015 -.0012	 0.0026 .0044	0.0033 .0033 .0048
0.27	18(b)	-0.9 -3.8	-0.0006 -.0006	-0.0008 -.0006	0.0043 .0050	0.0052 .0045
0.32	18(c)	-1.8 -4.8	-0.0008 -.0003	-0.0008 -.0006	0.0047 .0054	0.0041 .0043

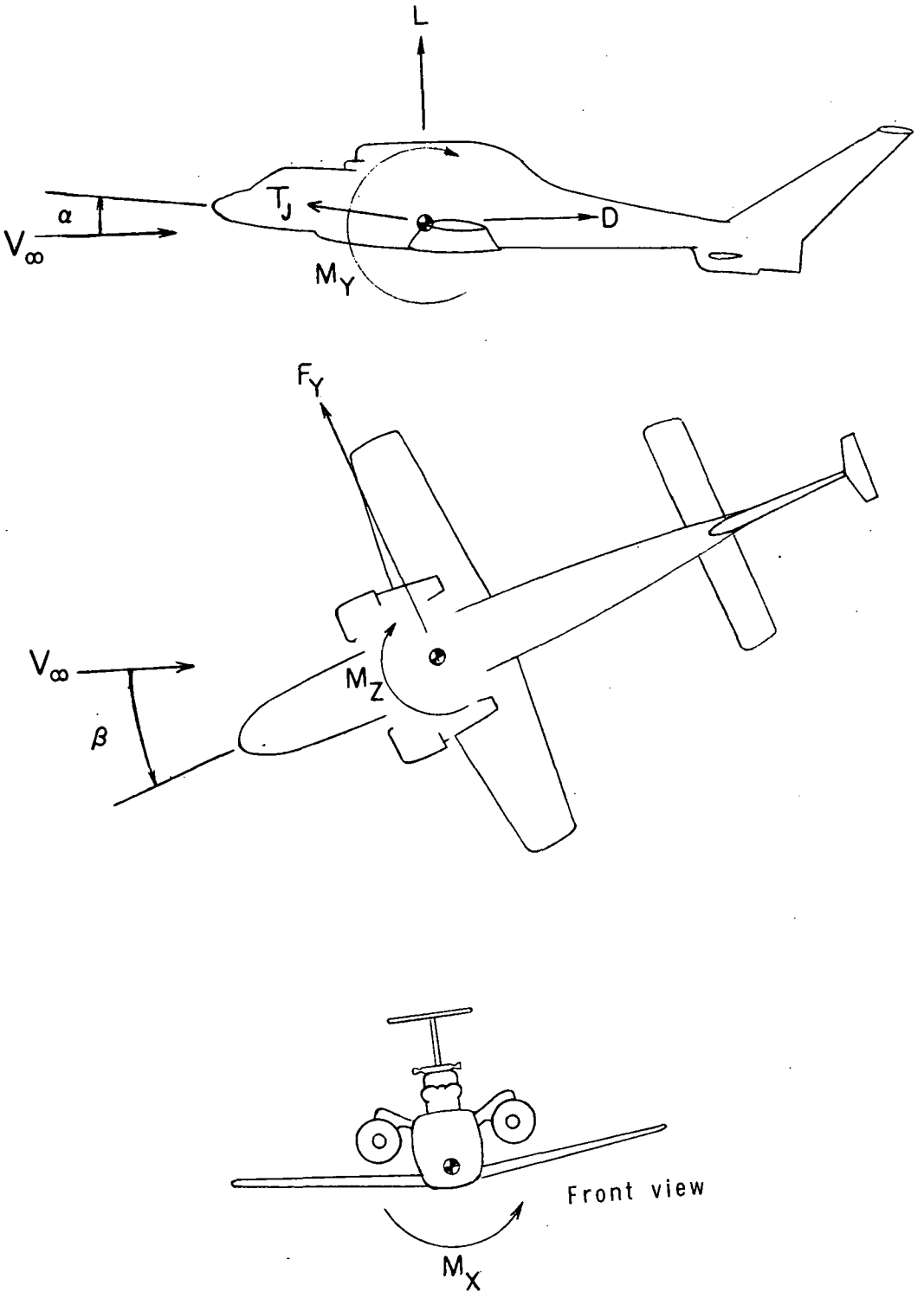

(a) Airframe system of axes.

Figure 1.- Axes and sign conventions. Positive directions are indicated by arrows.

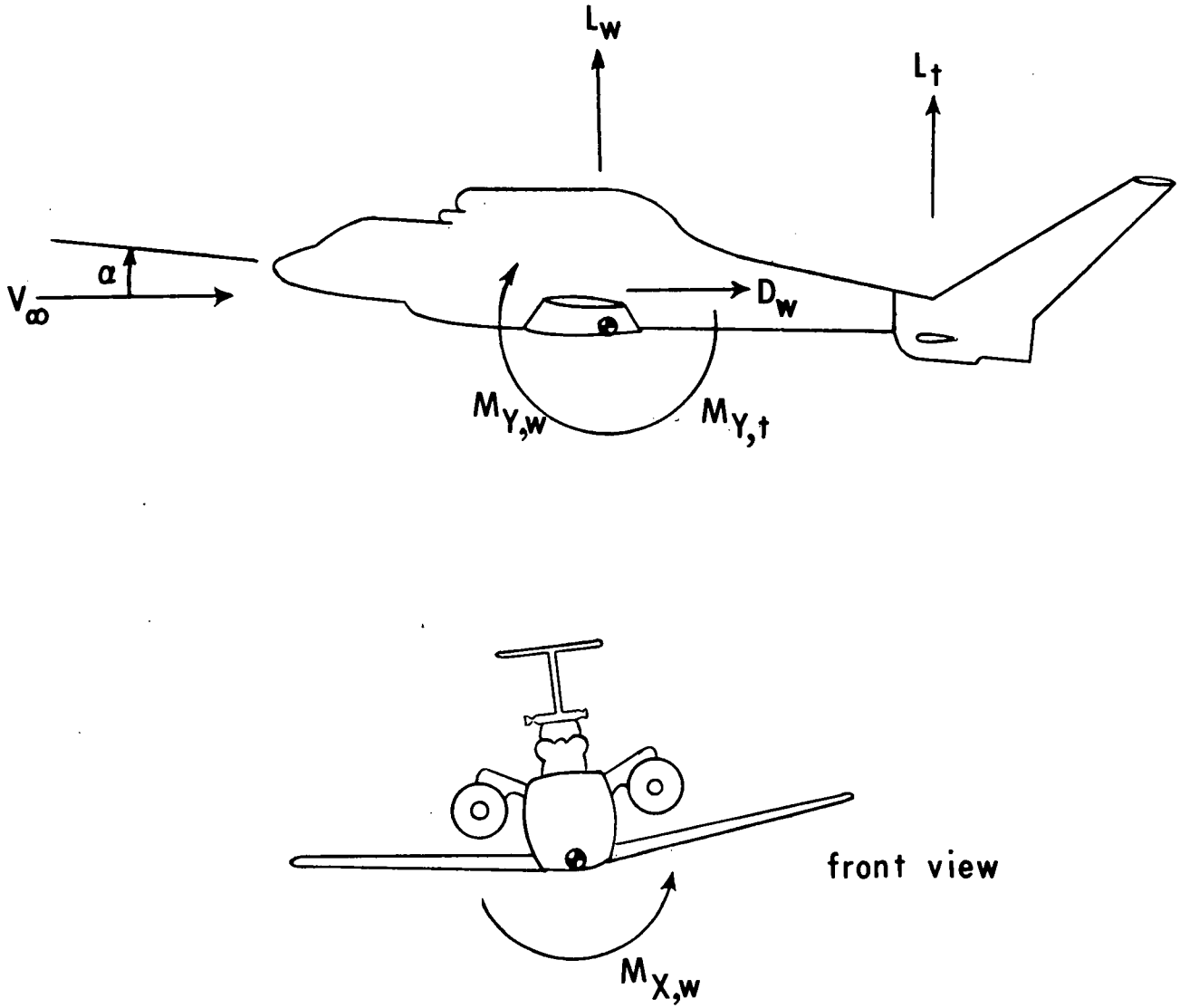

(b) Wing and tail system of axes.

Figure 1.- Continued.

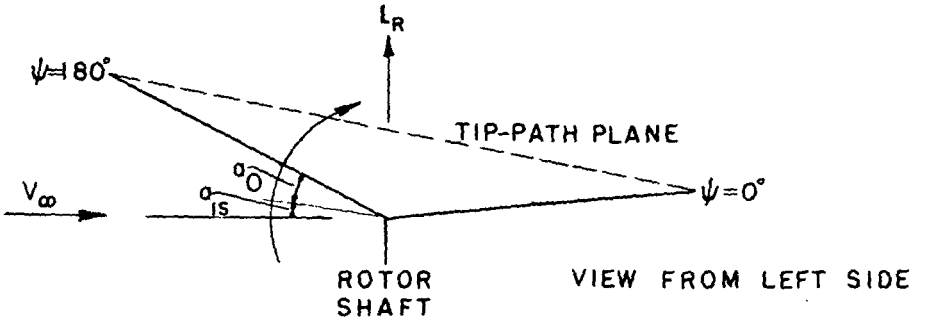

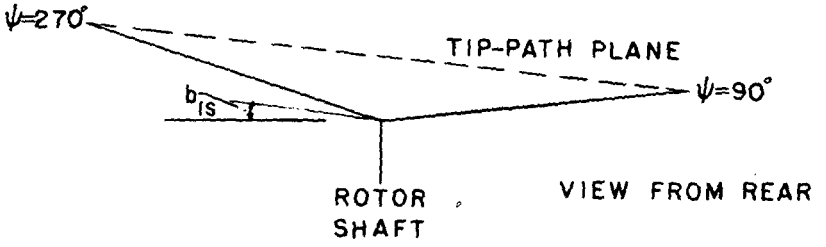

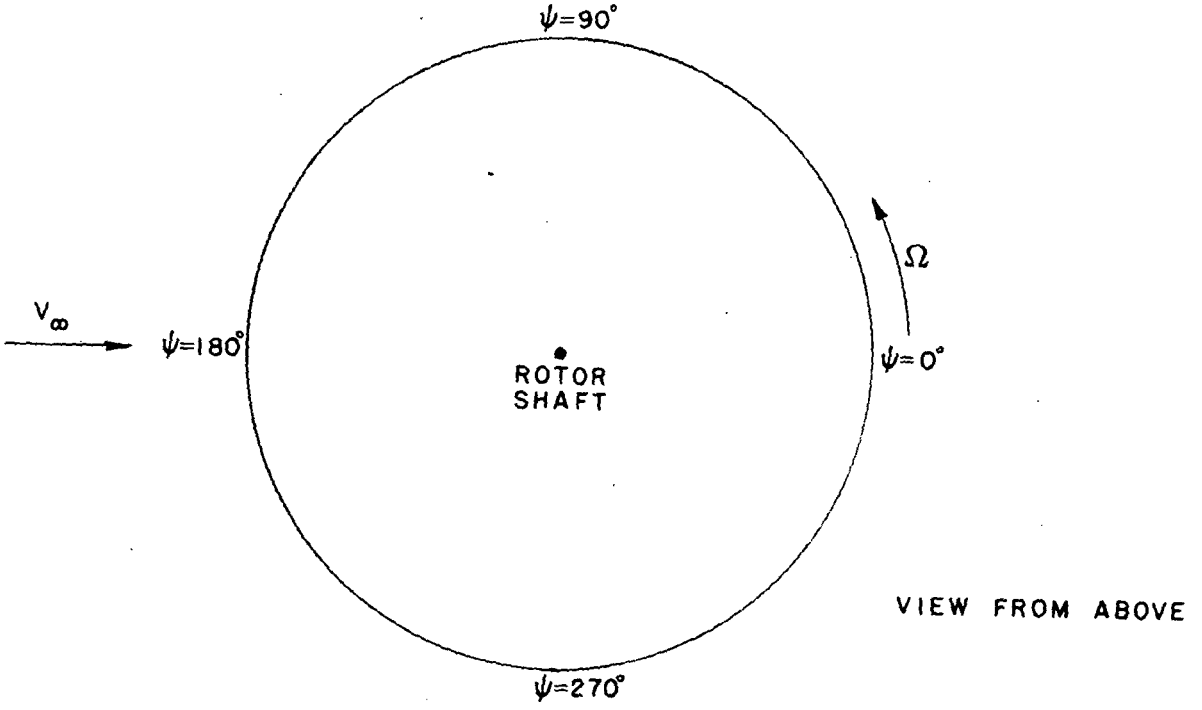

(c) Rotor system of axes.

Figure 1.- Continued.

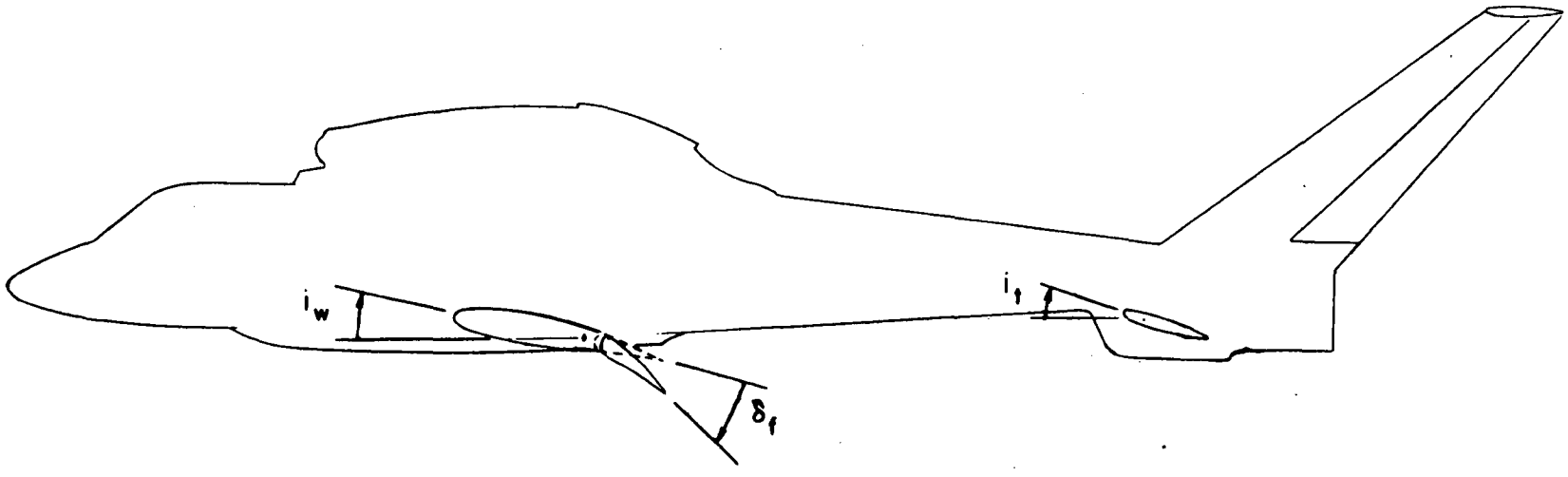

(d) Sign conventions for aerodynamic surfaces.

Figure 1.- Concluded.

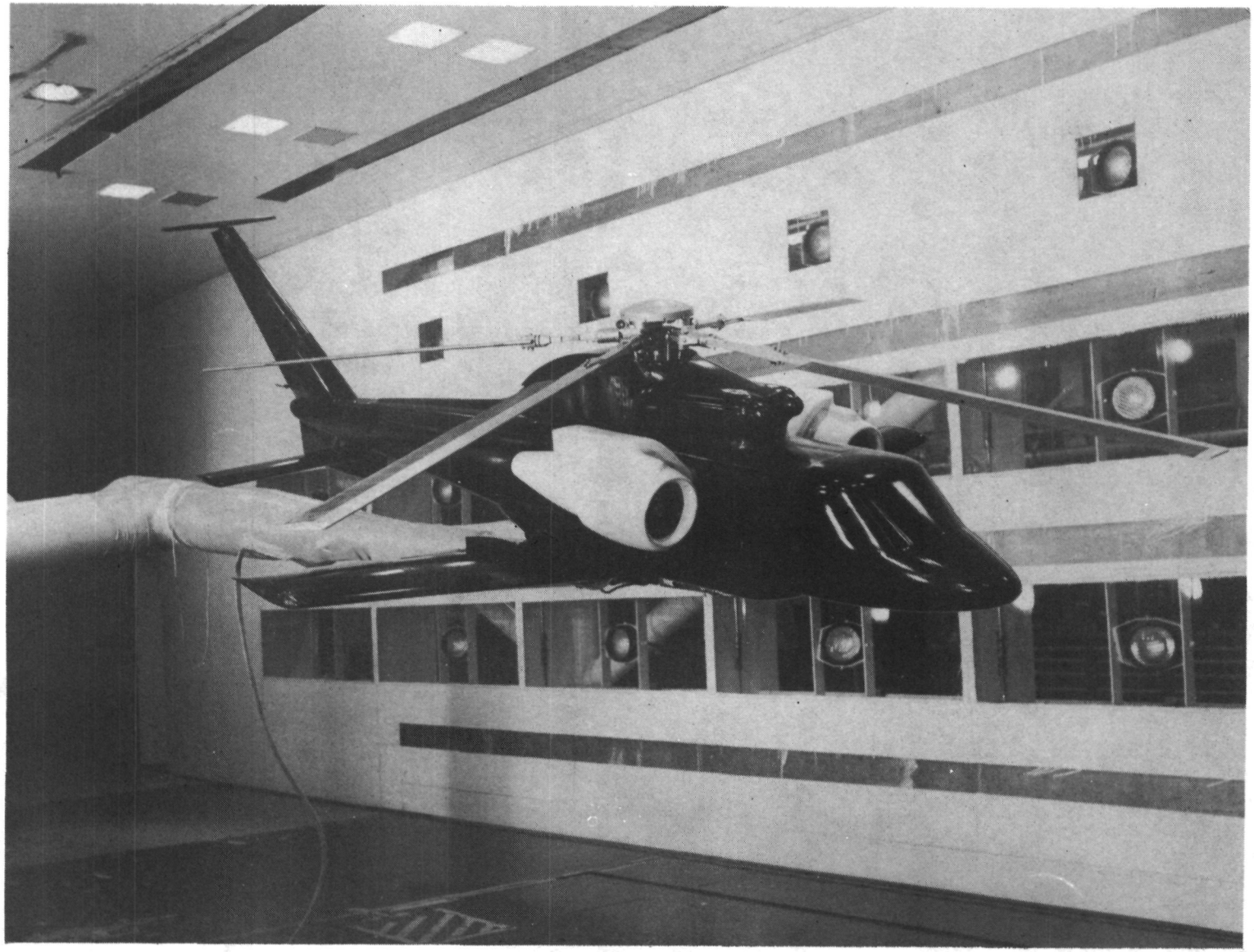

L-75-7510

Figure 2.- Model in Langley V/STOL tunnel.

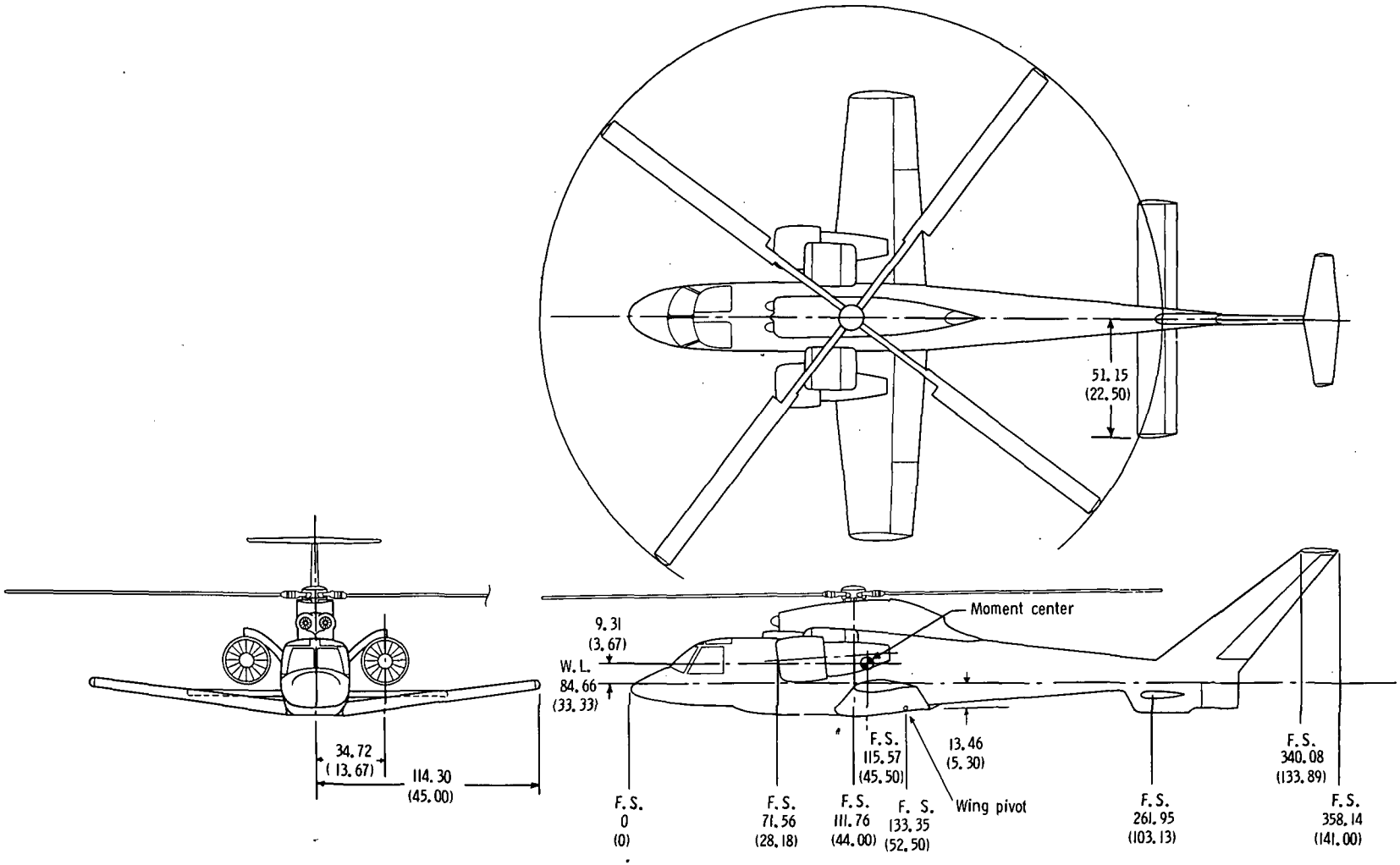

(a) Three-view sketch.

Figure 3.- Details of model. All dimensions are in cm (in.) unless specified otherwise. (F.S., fuselage station; W.L., water line.)

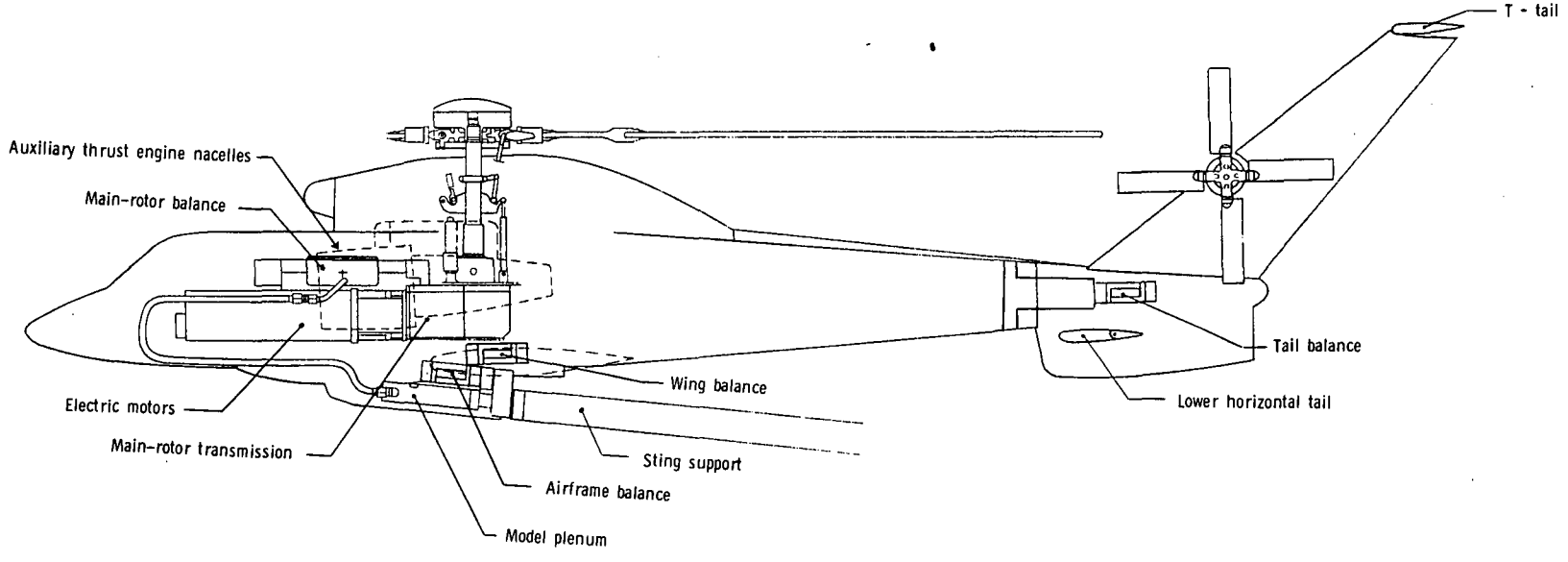

(b) Internal component layout.

Figure 3.- Continued.

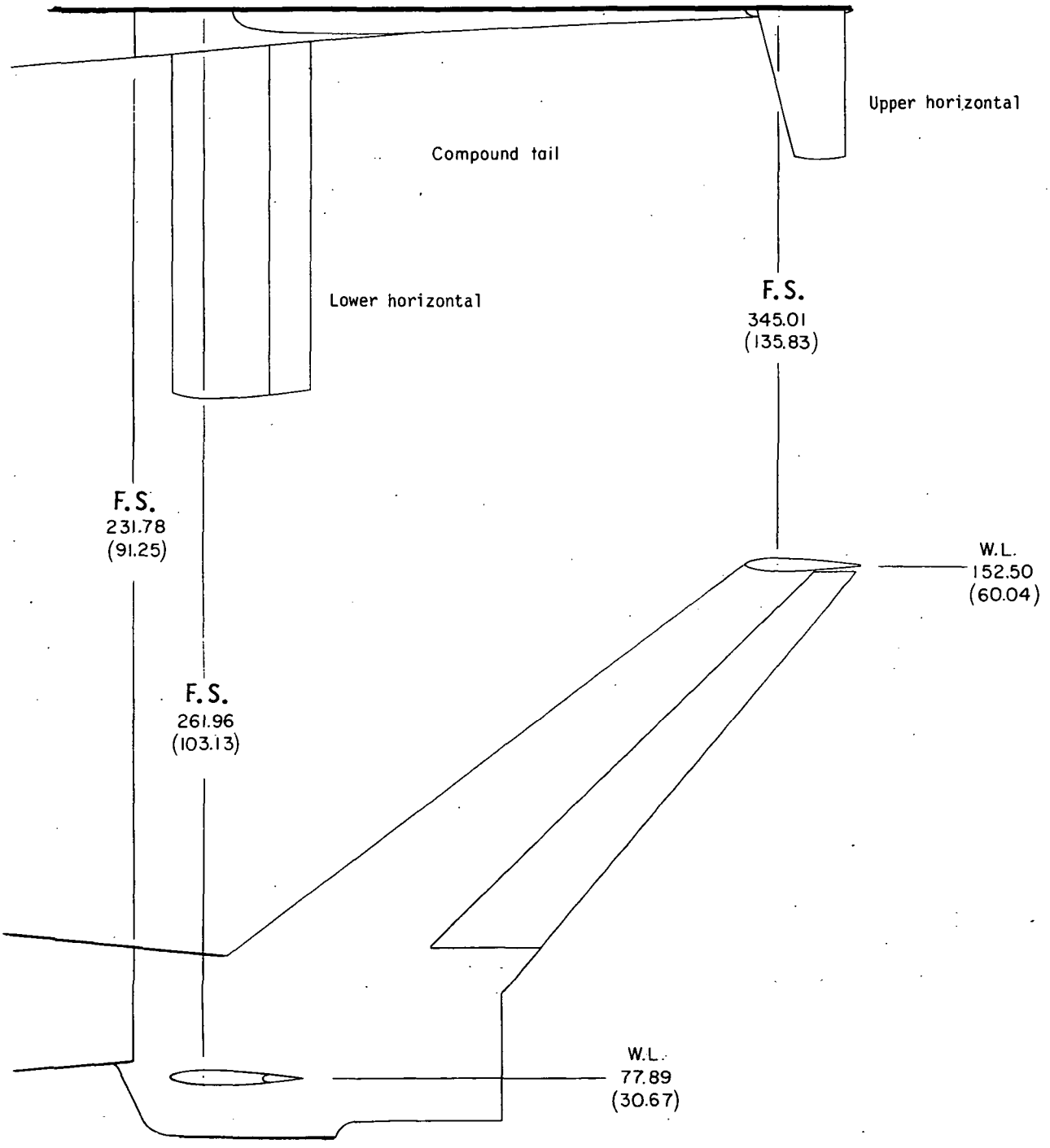

(c) Details of horizontal and vertical tails.

Figure 3.- Continued.

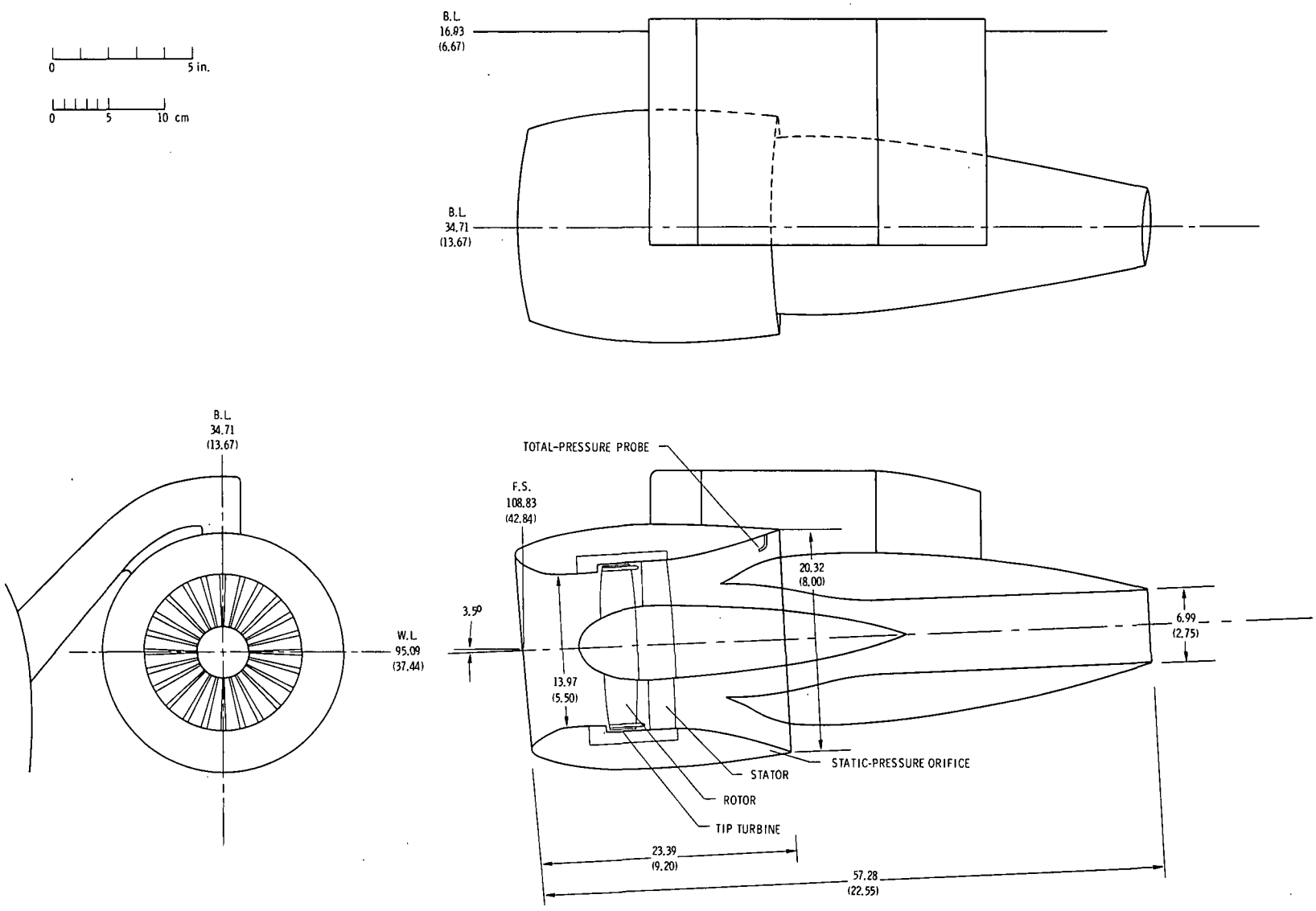

(d) Details of auxiliary thrust engine simulators. (B.L., buttock line.)

Figure 3.- Concluded.

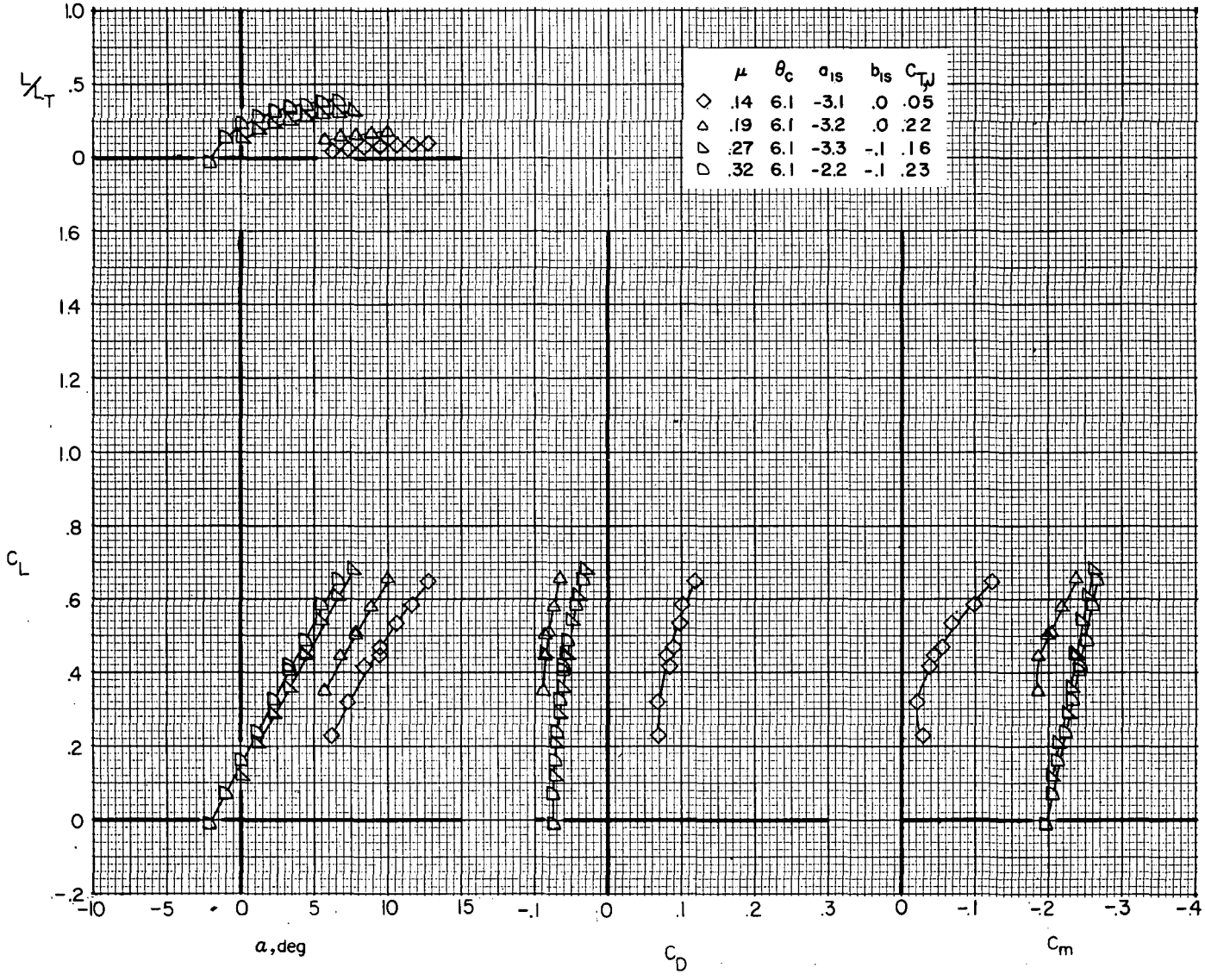

(a) $i_w = 0^\circ$; $\delta_f = 0^\circ$.

Figure 4.- Variation of airframe longitudinal aerodynamic characteristics for compound helicopter (rotor forces and moments removed) with angle of attack. $\delta_3 = -26.7^\circ$; $i_t = 3^\circ$. (θ_c, a_{1s}, and b_{1s} are in degrees.)

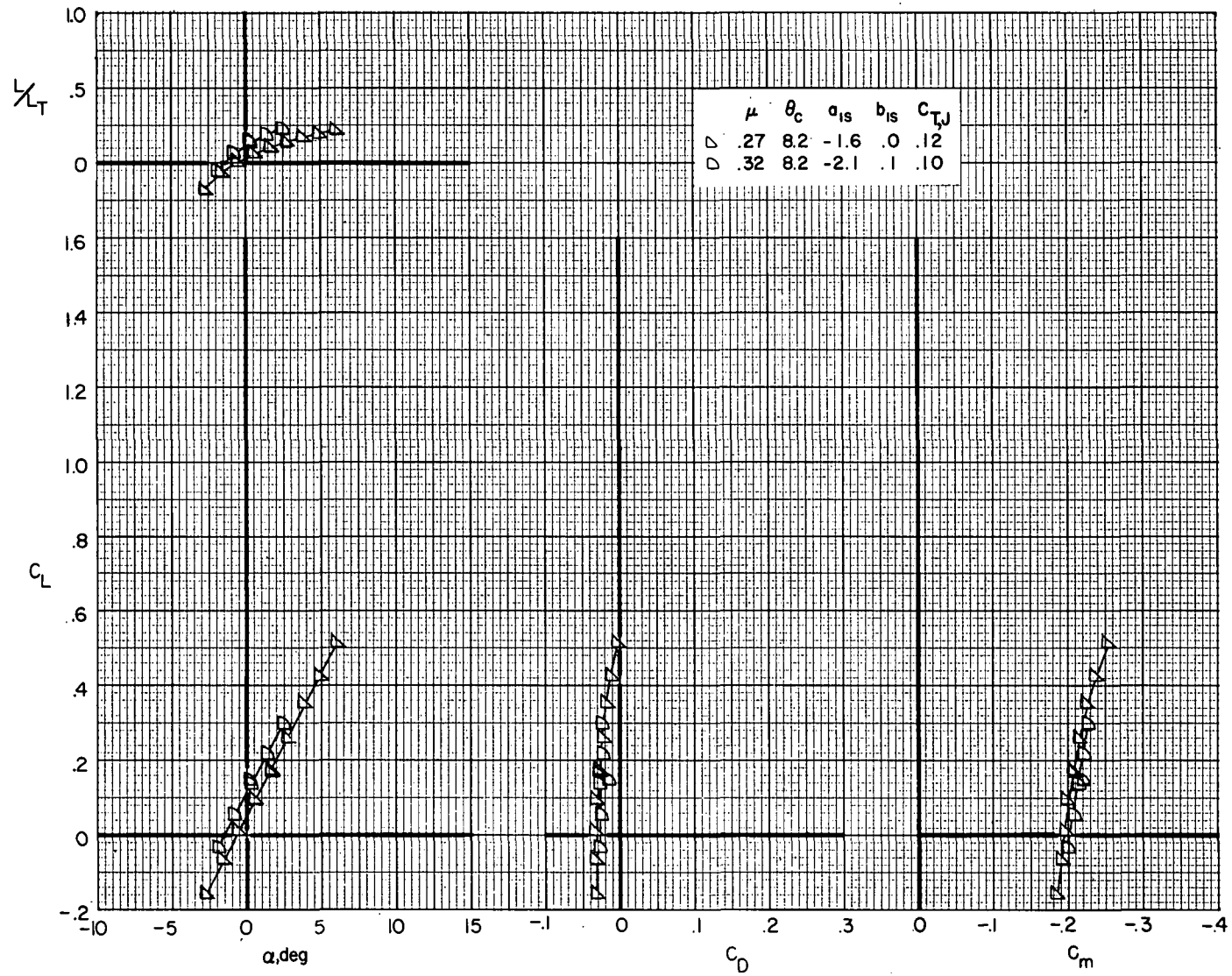

(a) Concluded.

Figure 4.- Continued.

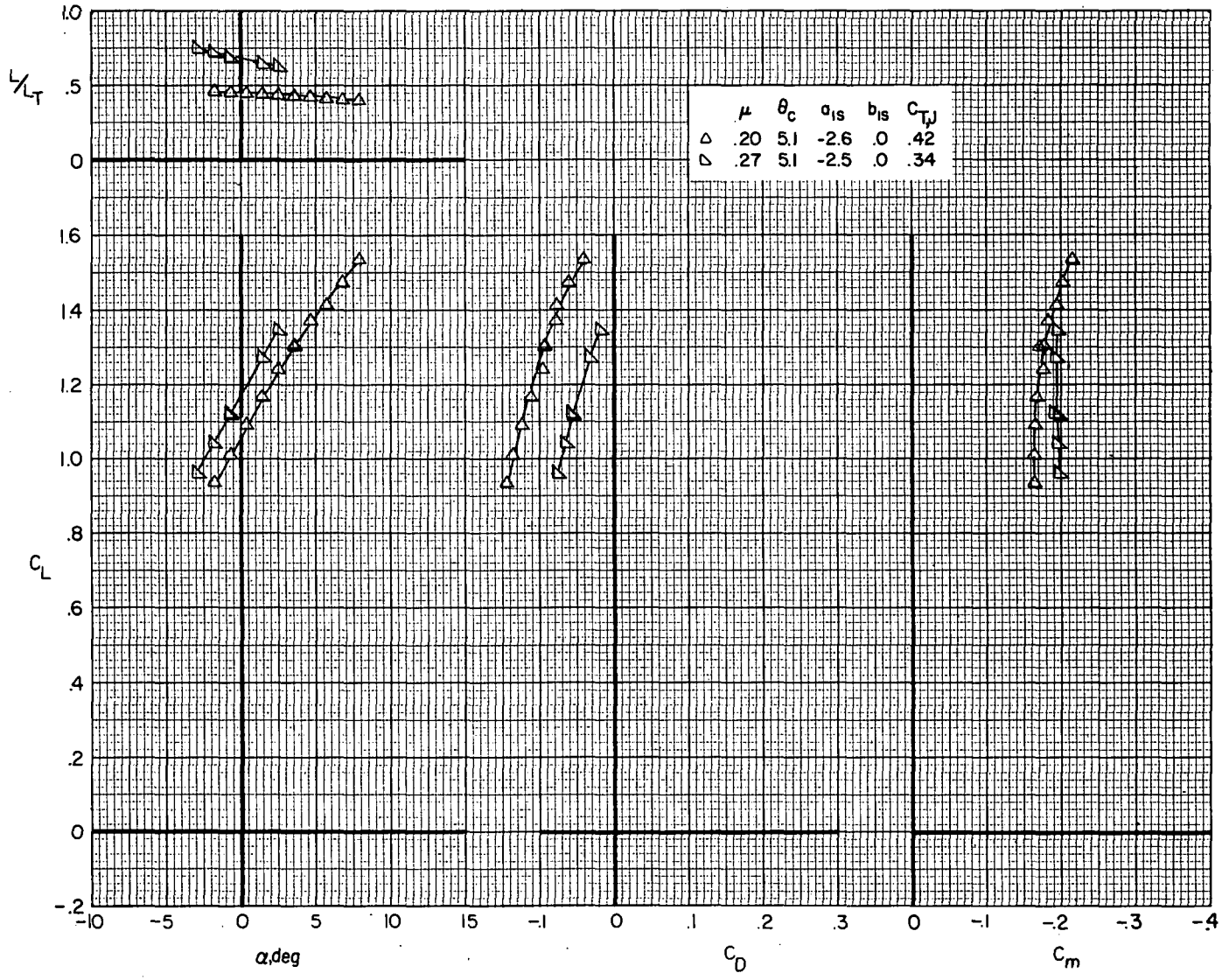

(b) $i_w = 7.5^\circ$; $\delta_f = 30^\circ$.

Figure 4.- Continued.

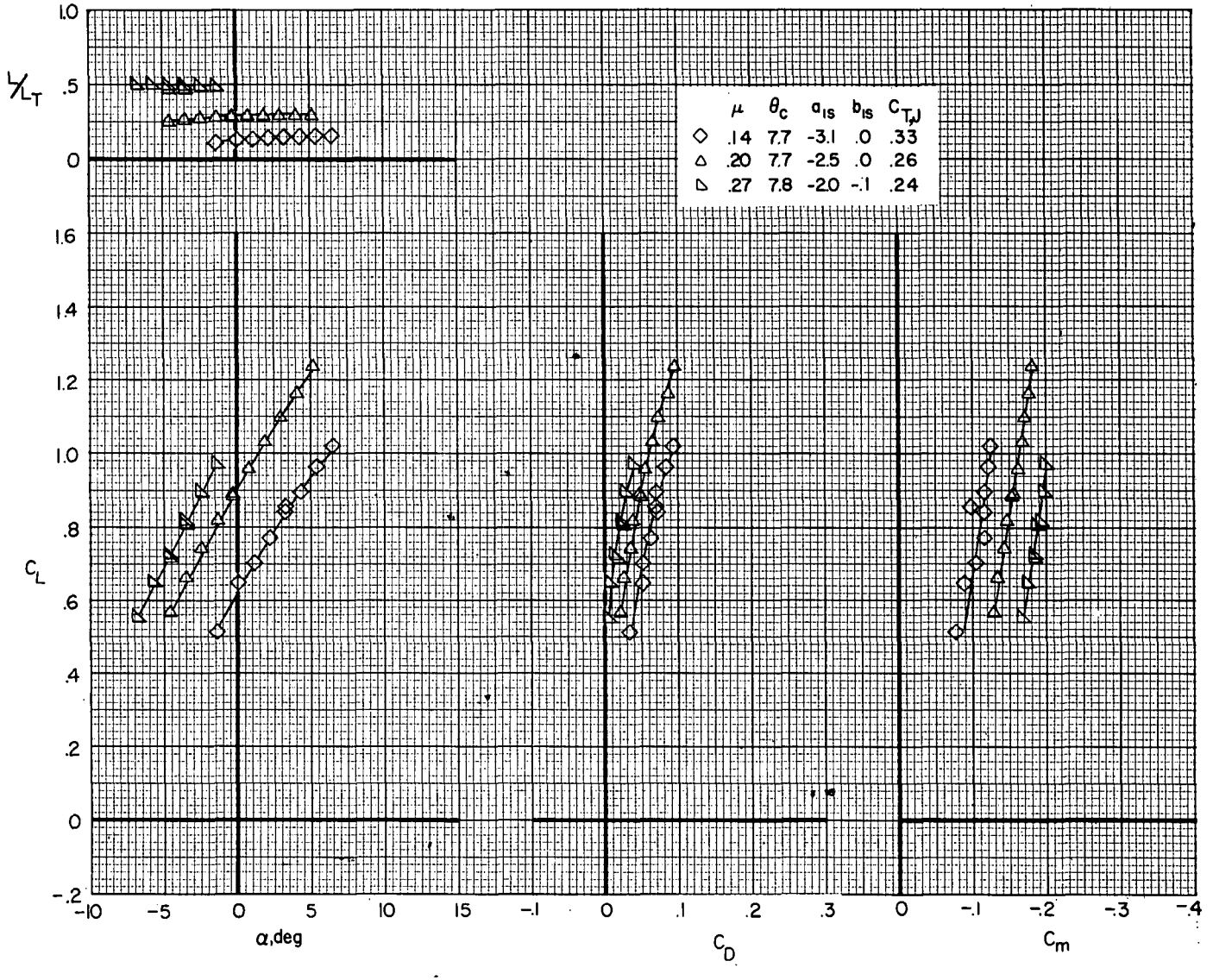

(b) Concluded.

Figure 4.- Concluded.

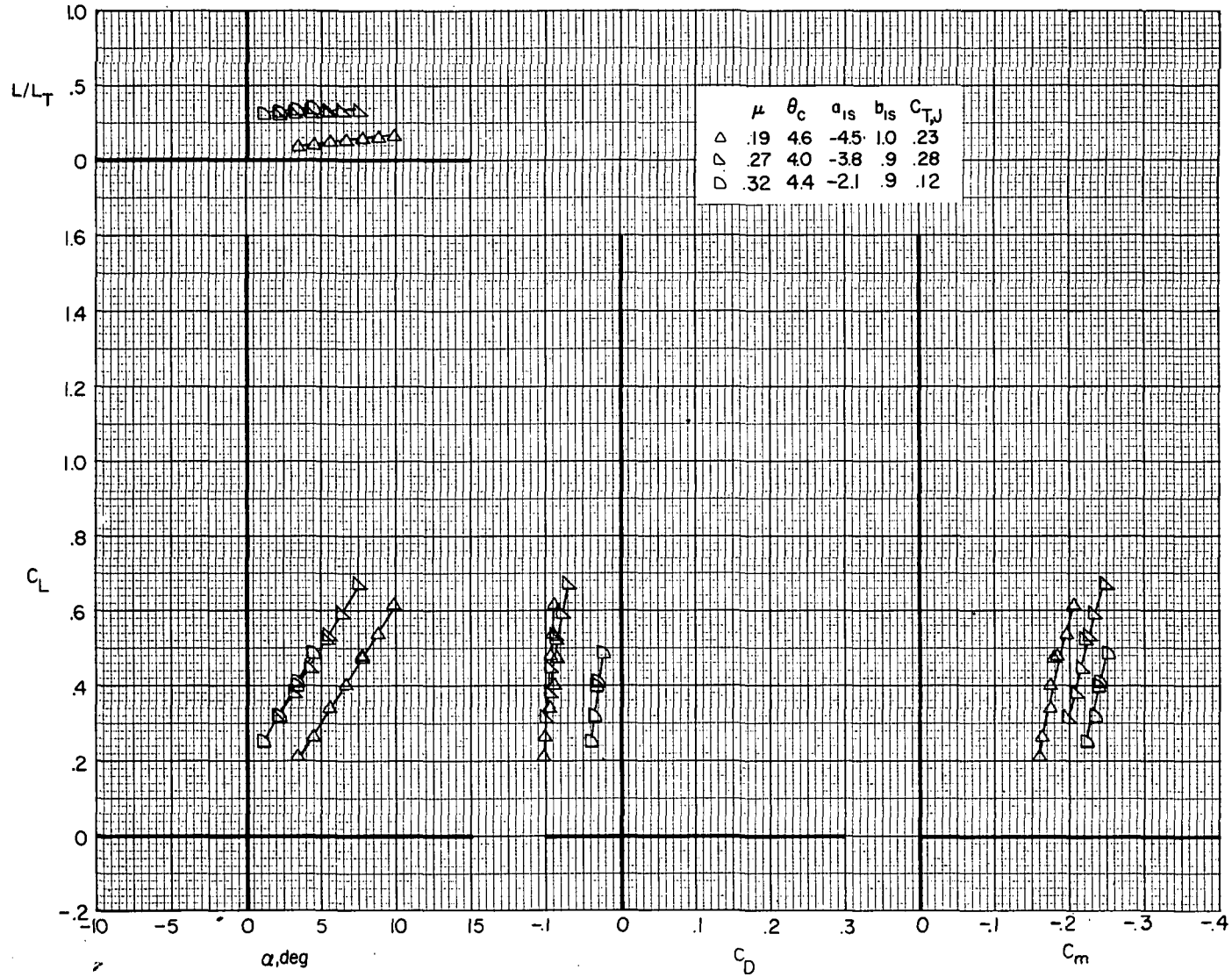

(a) $i_w = 0^\circ$; $\delta_f = 0^\circ$.

Figure 5.- Variation of airframe longitudinal aerodynamic characteristics for compound helicopter (rotor forces and moments removed) with angle of attack. $\delta_3 = -2^\circ$; $i_t = 3^\circ$. (θ_c, a_{ls}, and b_{ls} are in degrees.)

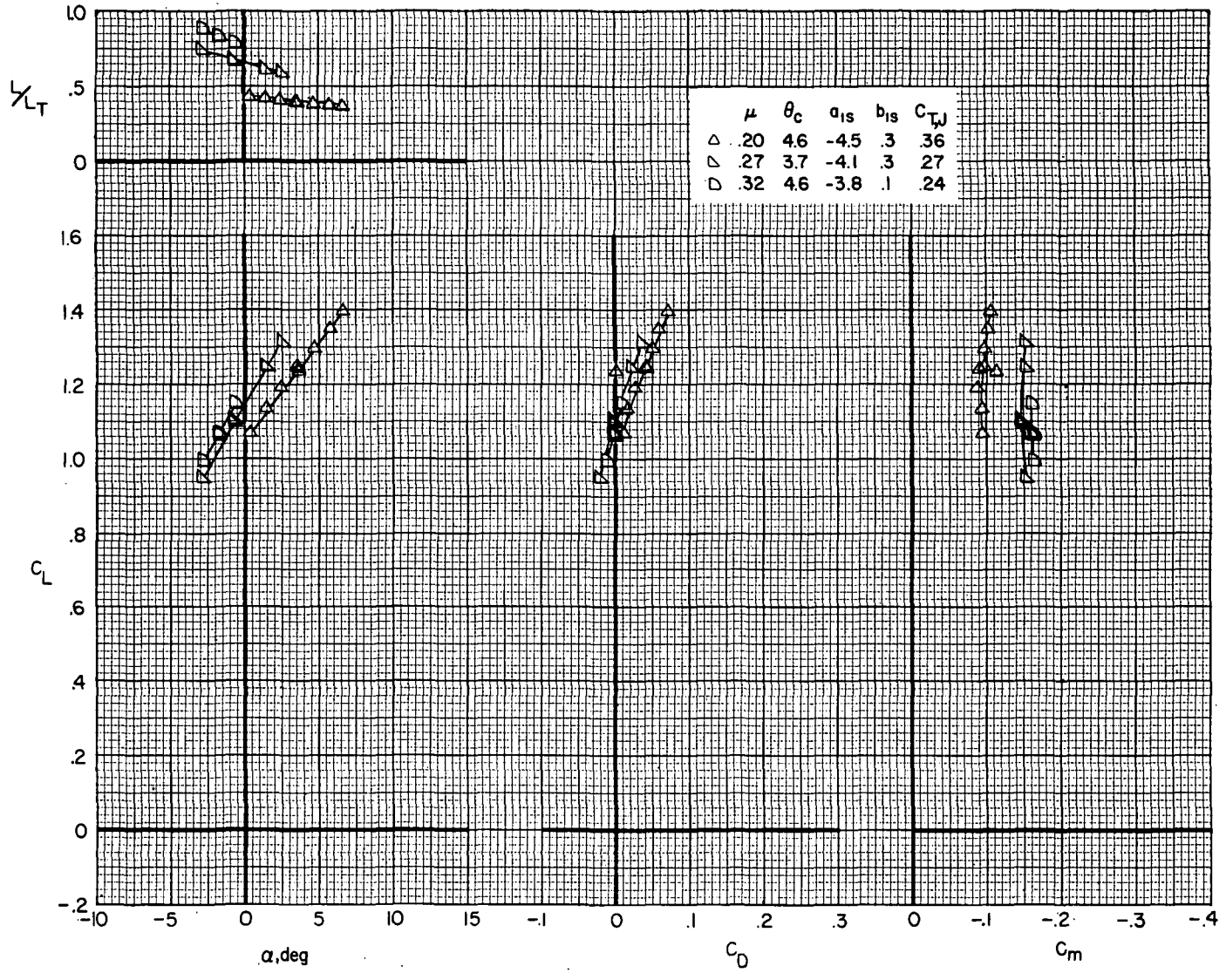

(b) $i_w = 7.5^\circ$; $\delta_f = 30^\circ$.

Figure 5.- Continued.

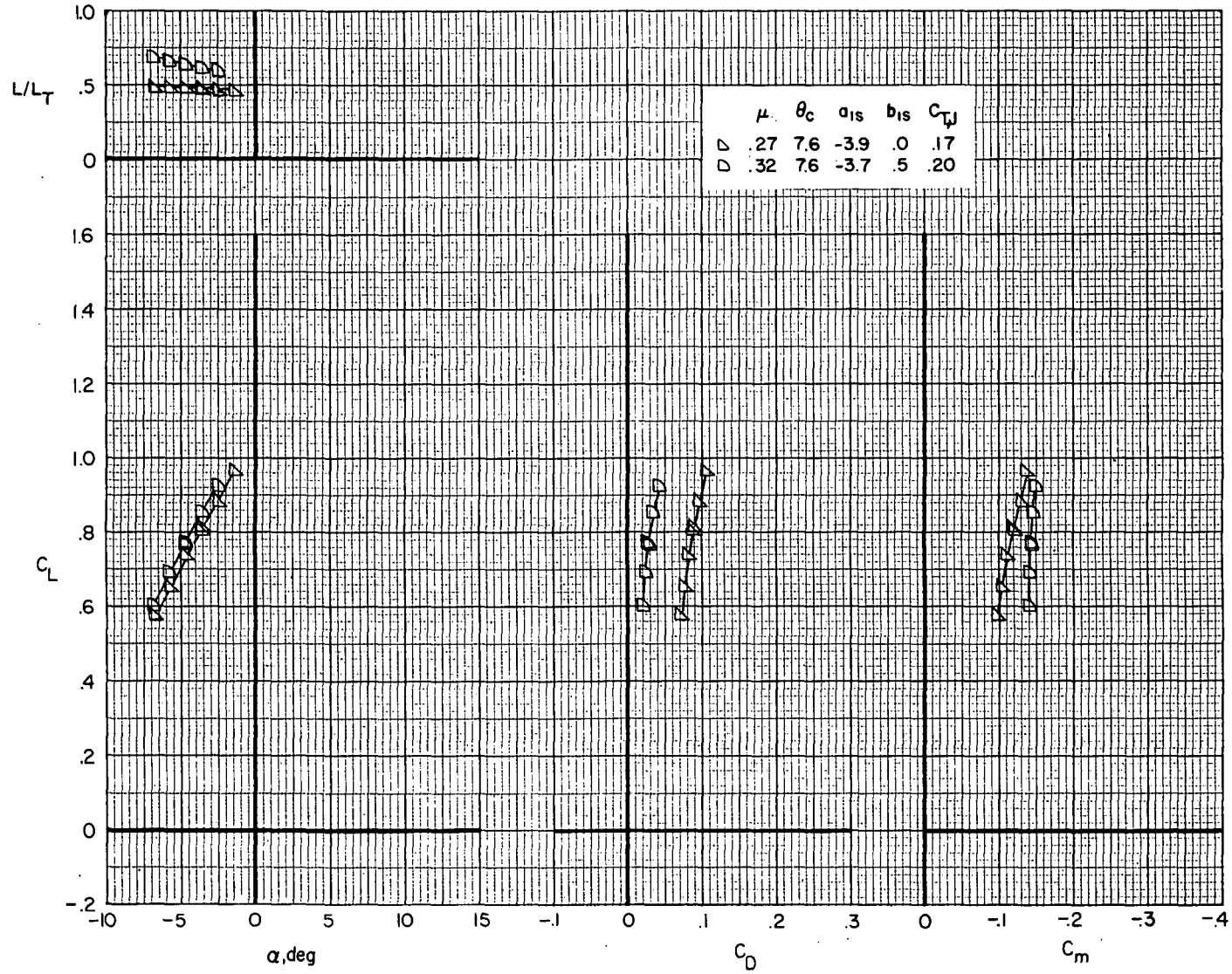

(b) Concluded.

Figure 5.- Concluded.

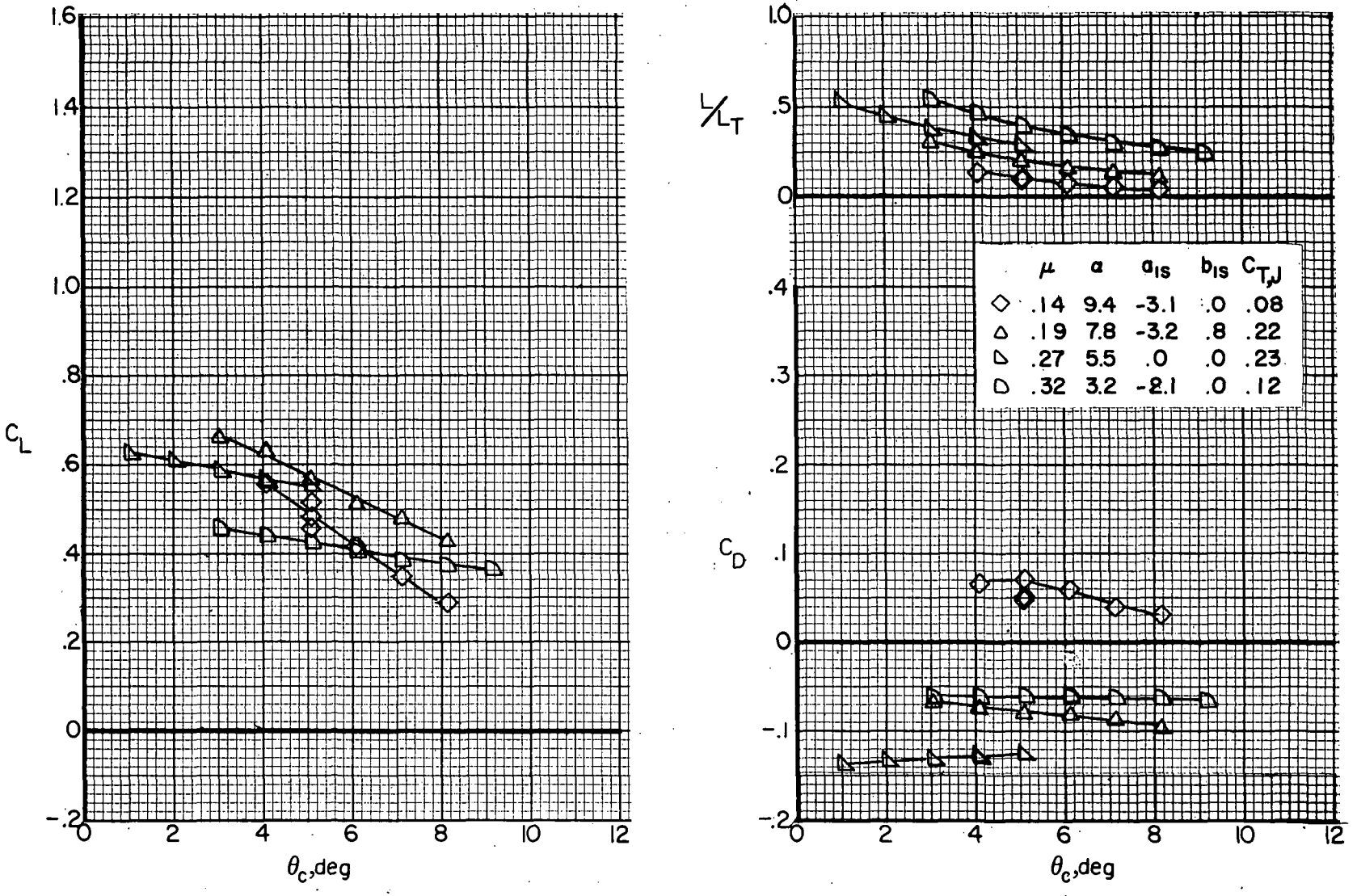

(a) $i_w = 0^\circ$; $\delta_f = 0^\circ$.

Figure 6.- Variation of airframe longitudinal aerodynamic characteristics for compound helicopter (rotor forces and moments removed) with collective pitch for several advance ratios. $\delta_3 = -26.7^\circ$; $i_t = 3^\circ$. (a_{1s} and b_{1s} are in degrees.)

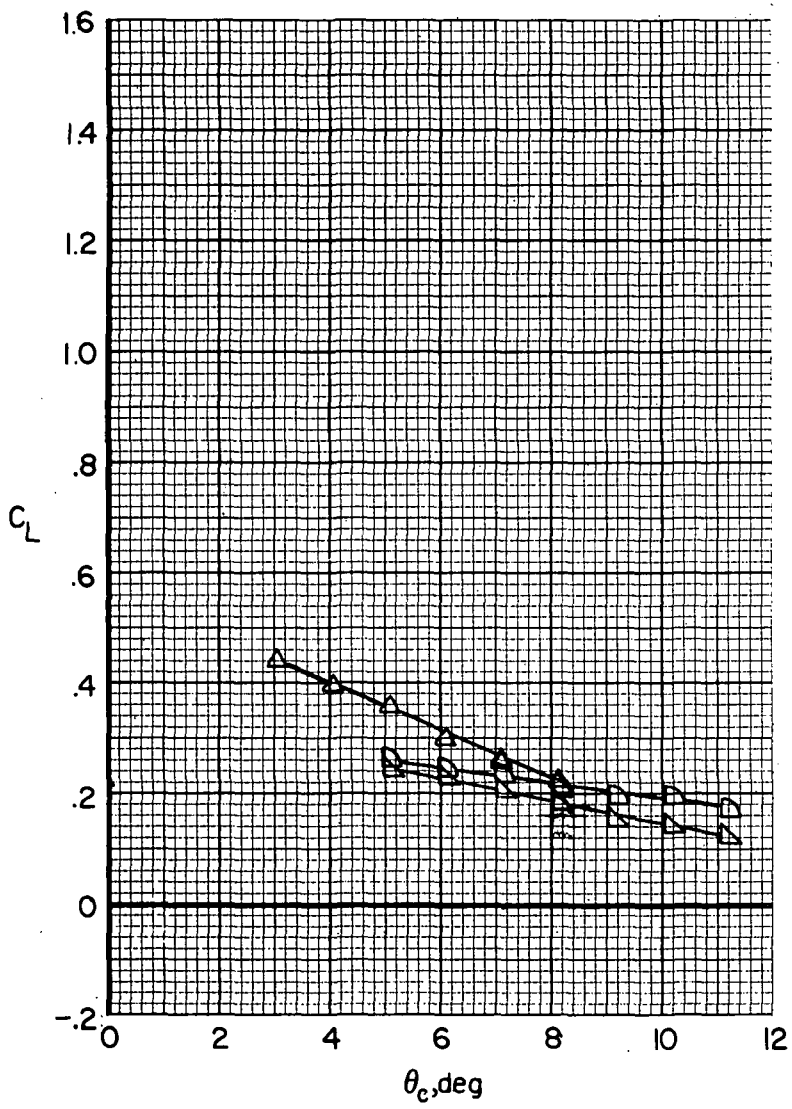

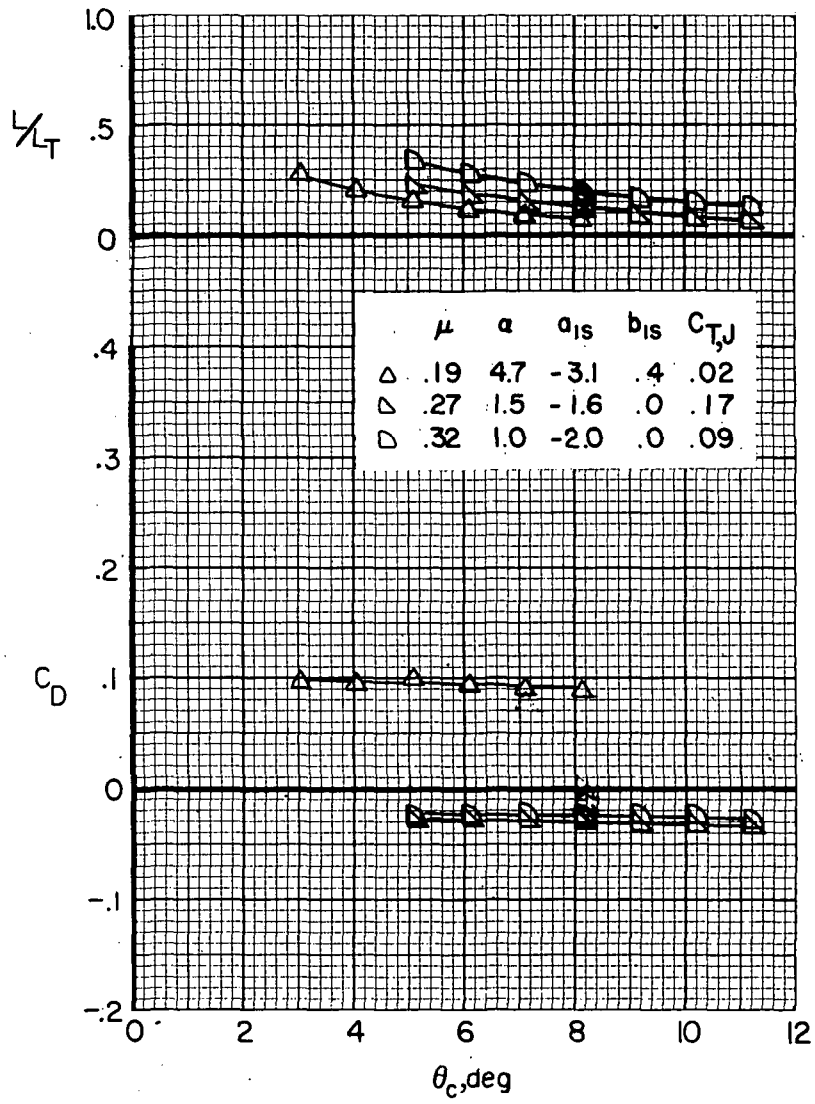

(a) Concluded.

Figure 6.- Continued.

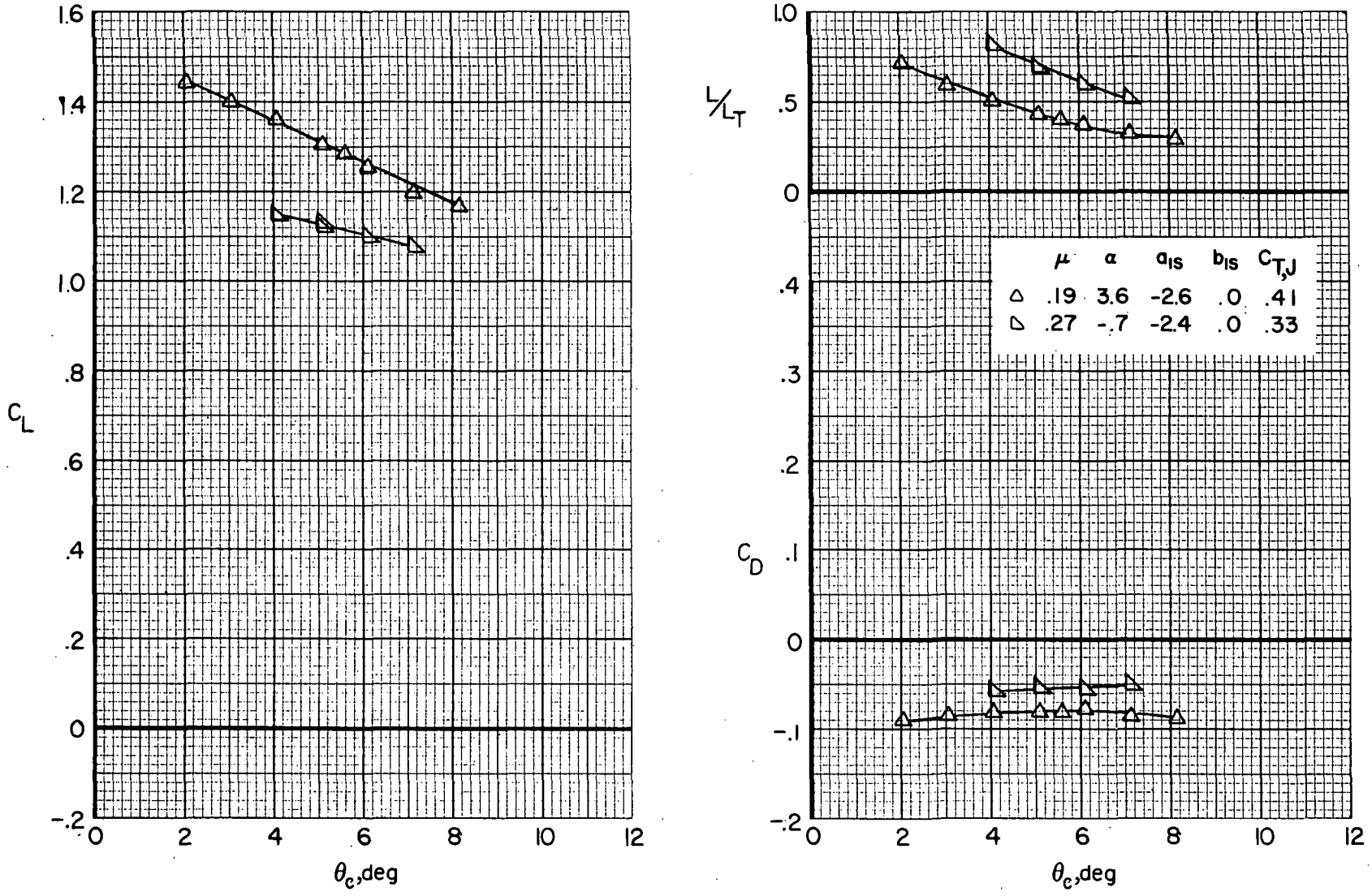

(b) $i_w = 7.5^\circ$; $\delta_f = 30^\circ$.

Figure 6.- Continued.

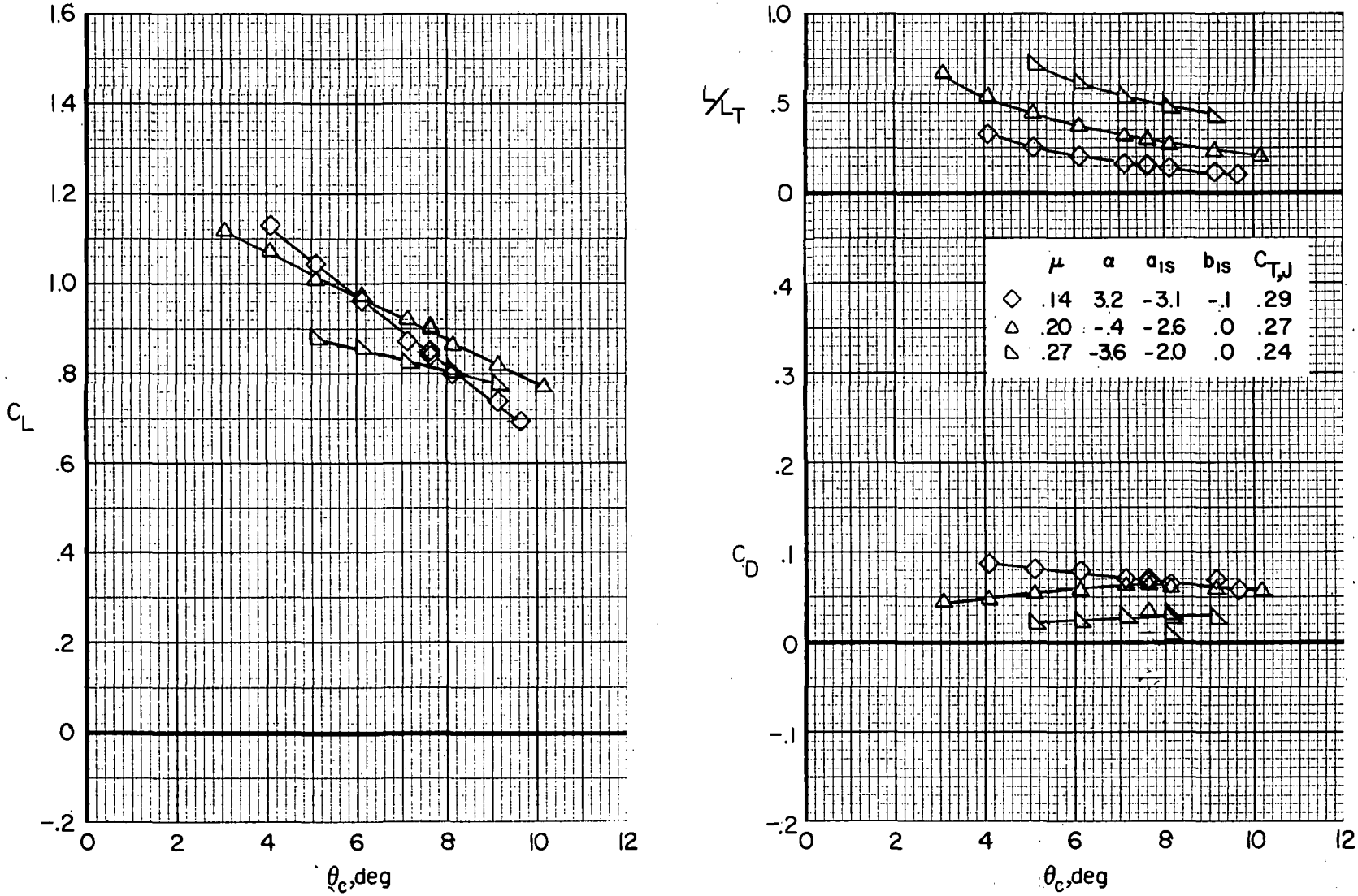

(b) Concluded.

Figure 6.- Concluded.

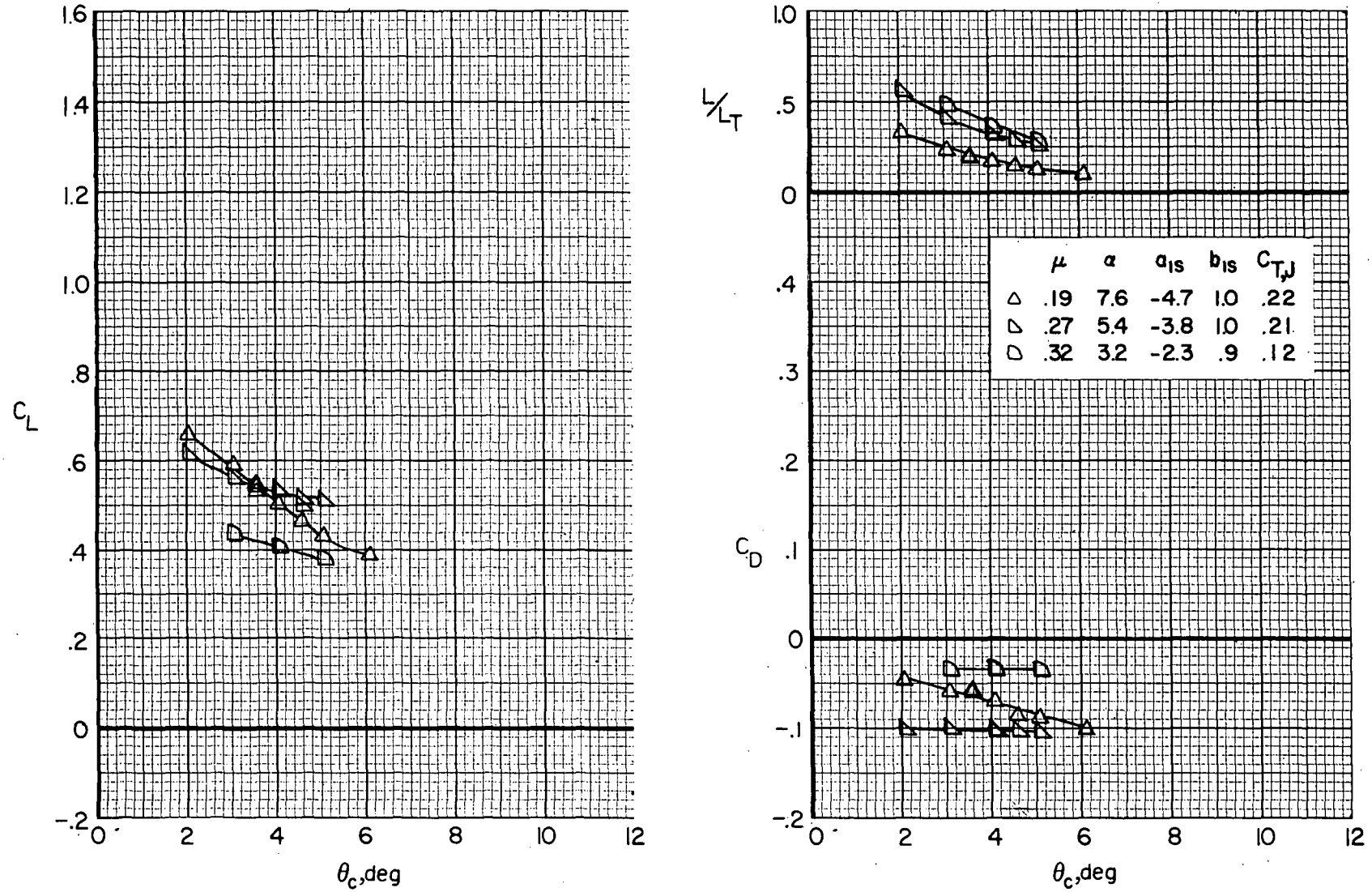

(a) $i_w = 0^\circ$; $\delta_f = 0^\circ$.

Figure 7.- Variation of airframe longitudinal aerodynamic characteristics for compound helicopter (rotor forces and moments removed) with collective pitch for several advance ratios. $\delta_3 = -2.0^\circ$; $i_t = 3^\circ$. (a_{1s} and b_{1s} are in degrees.)

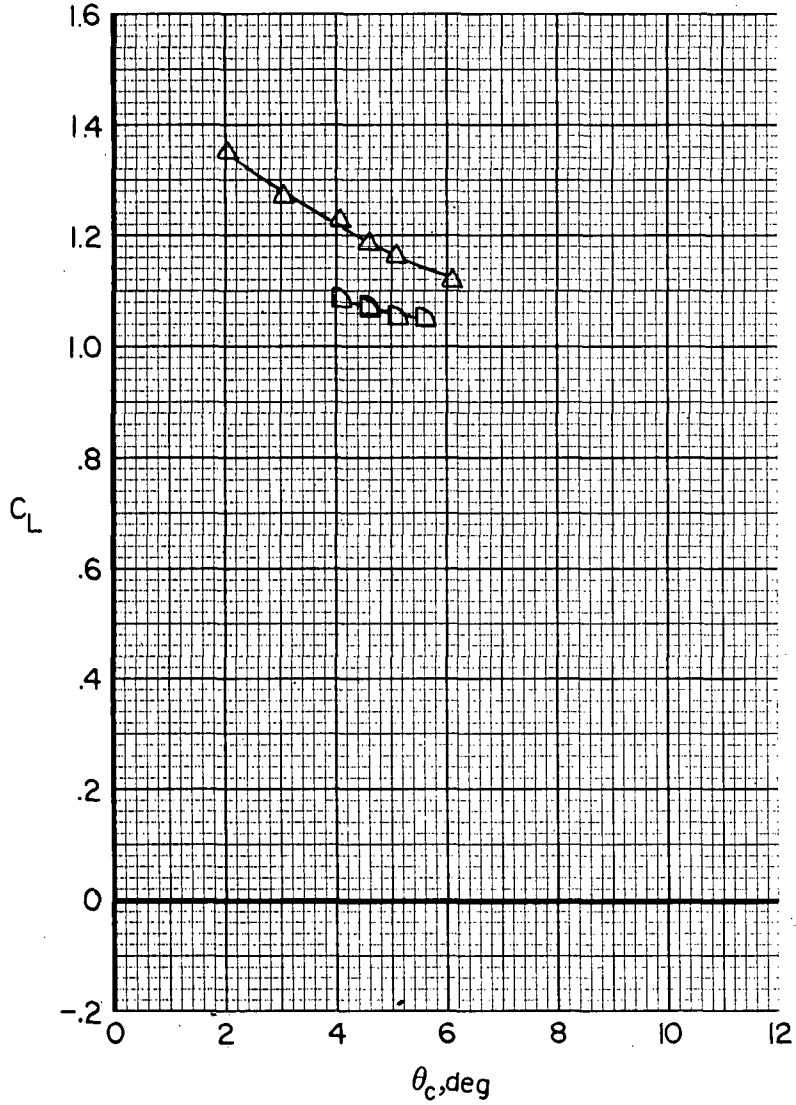

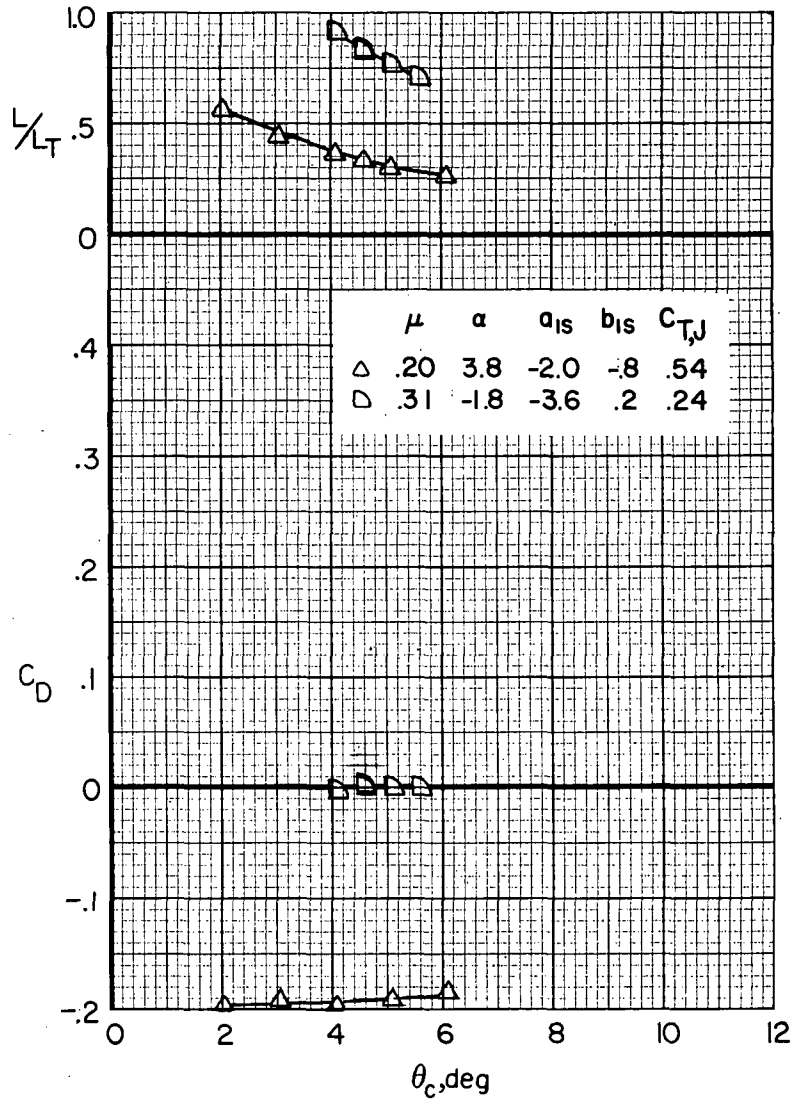

(b) $i_w = 7.5^\circ$; $\delta_f = 30^\circ$.

Figure 7.- Continued.

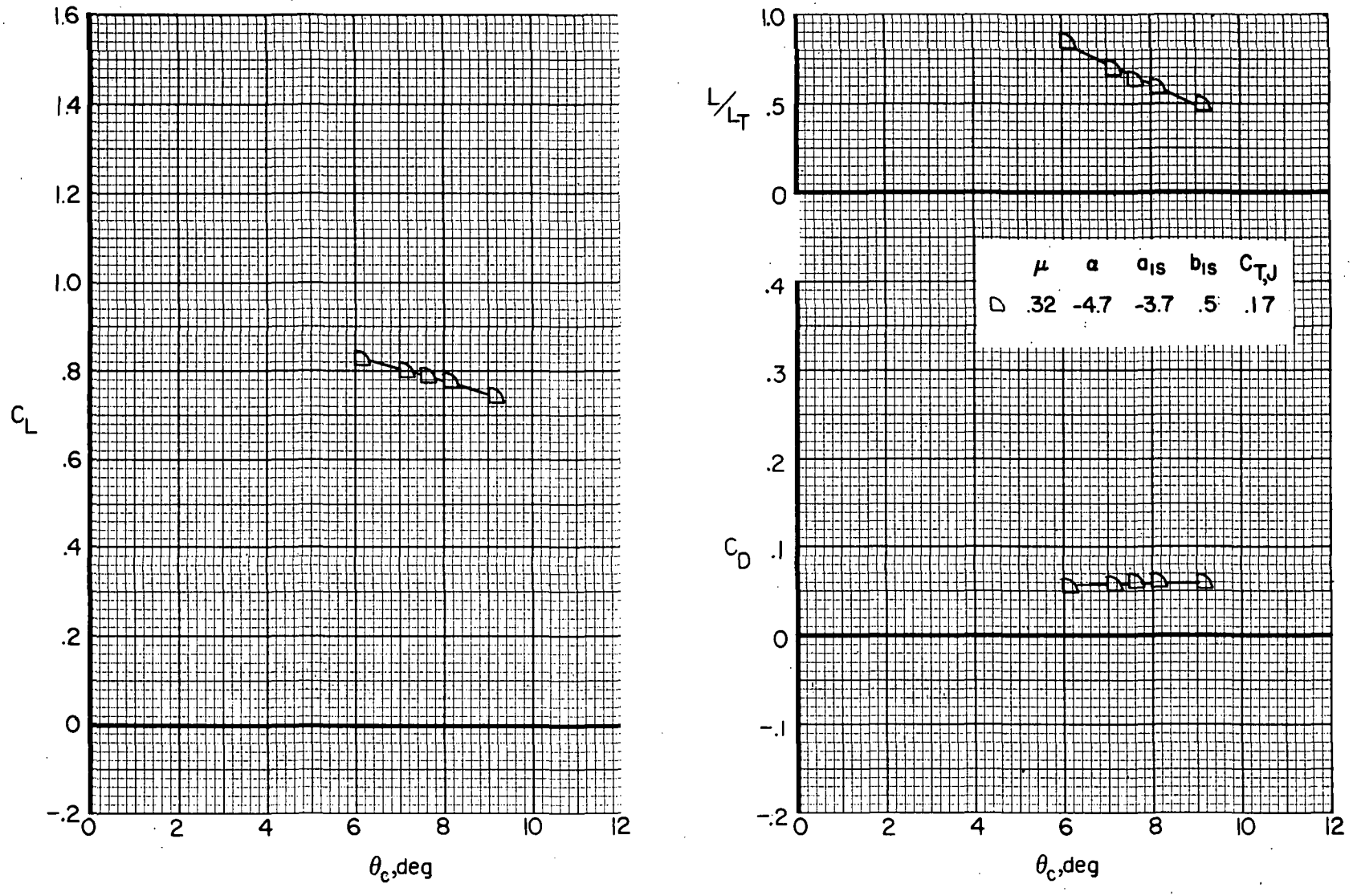

(b) Concluded.

Figure 7.- Concluded.

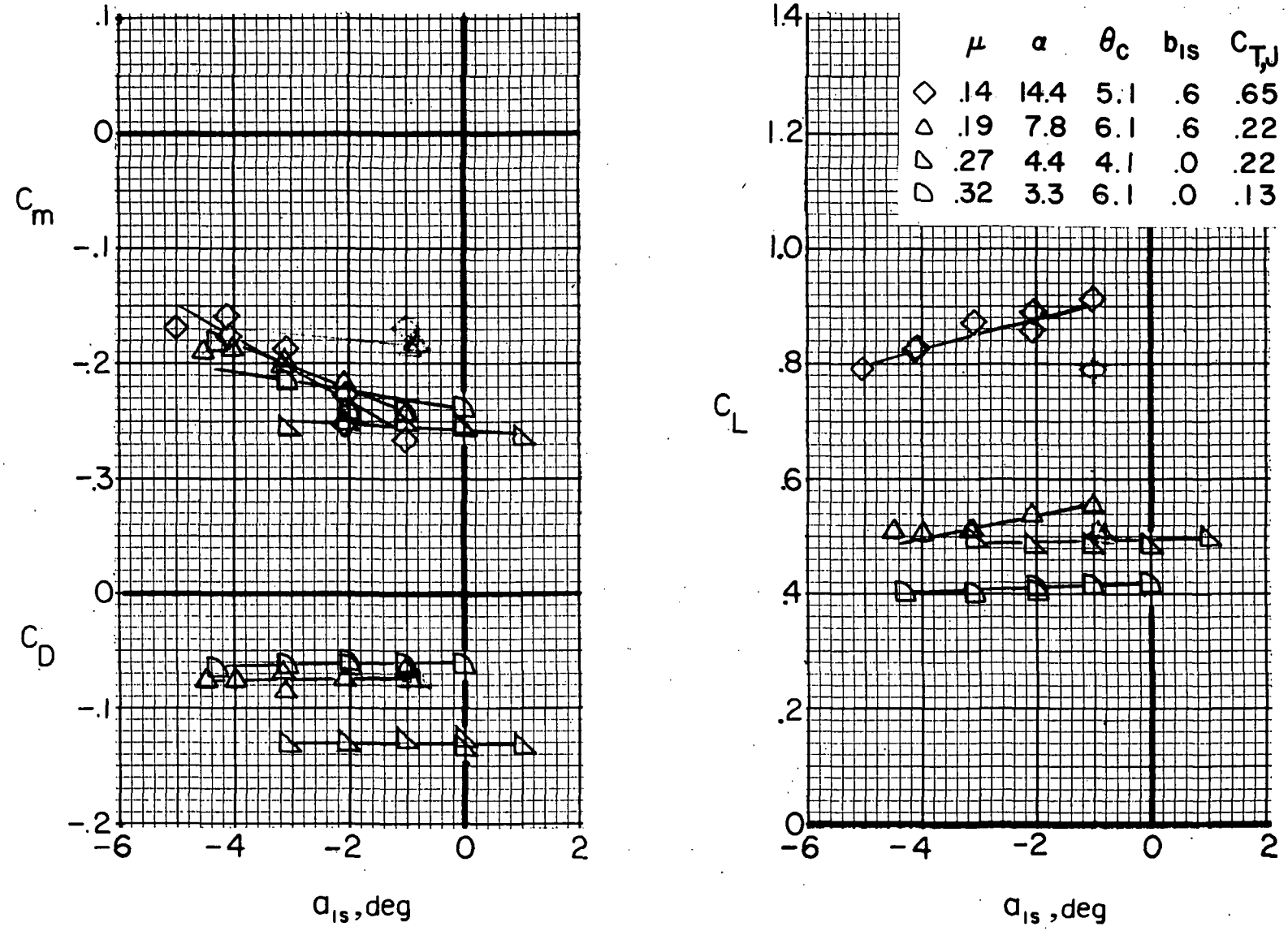

(a) $i_w = 0^o$; $\delta_f = 0^o$.

Figure 8.- Variation of airframe longitudinal aerodynamic characteristics for compound helicopter (rotor forces and moments removed) with longitudinal rotor flapping at several advance ratios. $\delta_3 = -27.6^o$; $i_t = 3^o$. (α, θ_c, and b_{ls} are in degrees.)

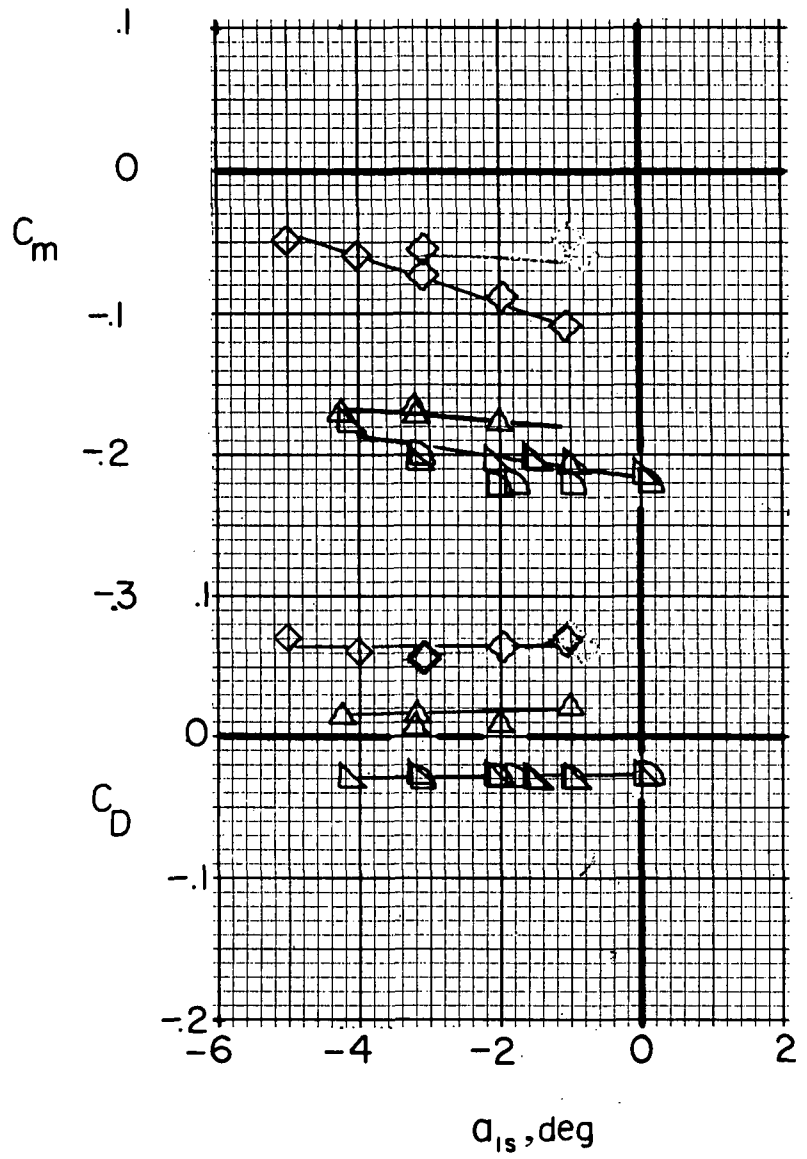

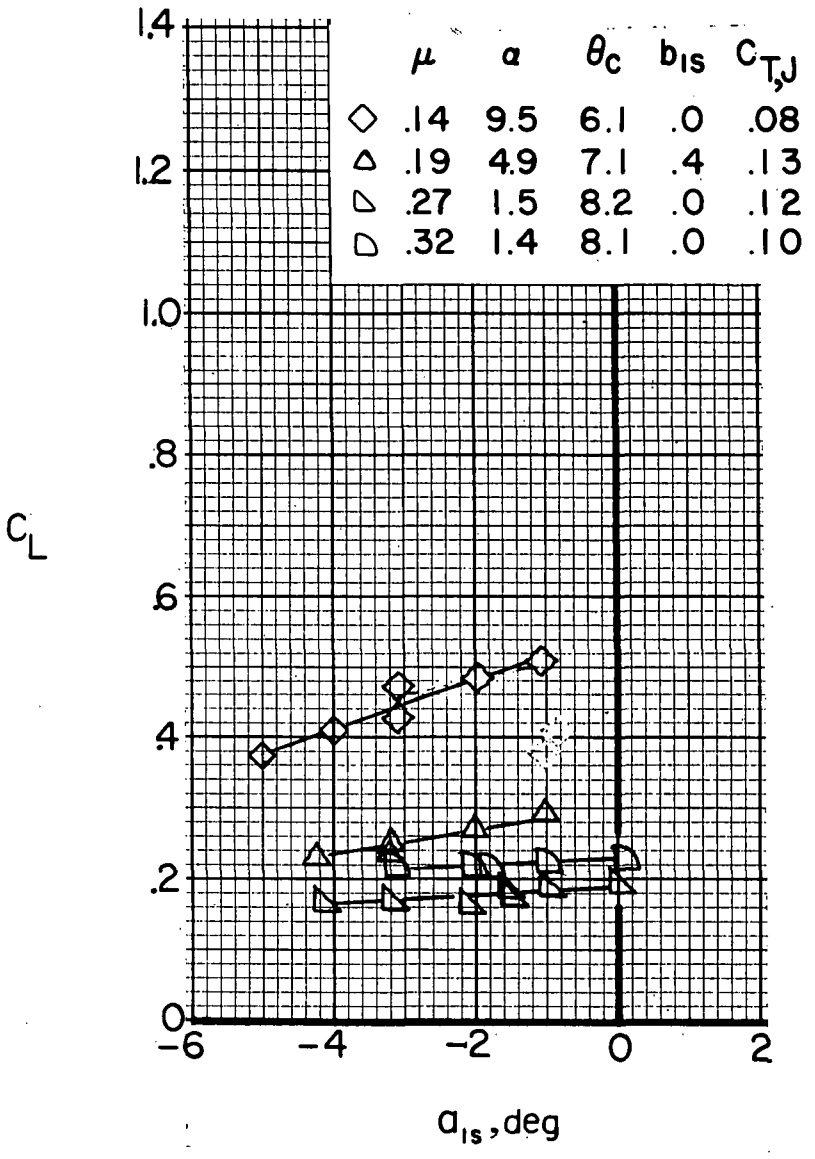

(a) Continued.

Figure 8.- Continued.

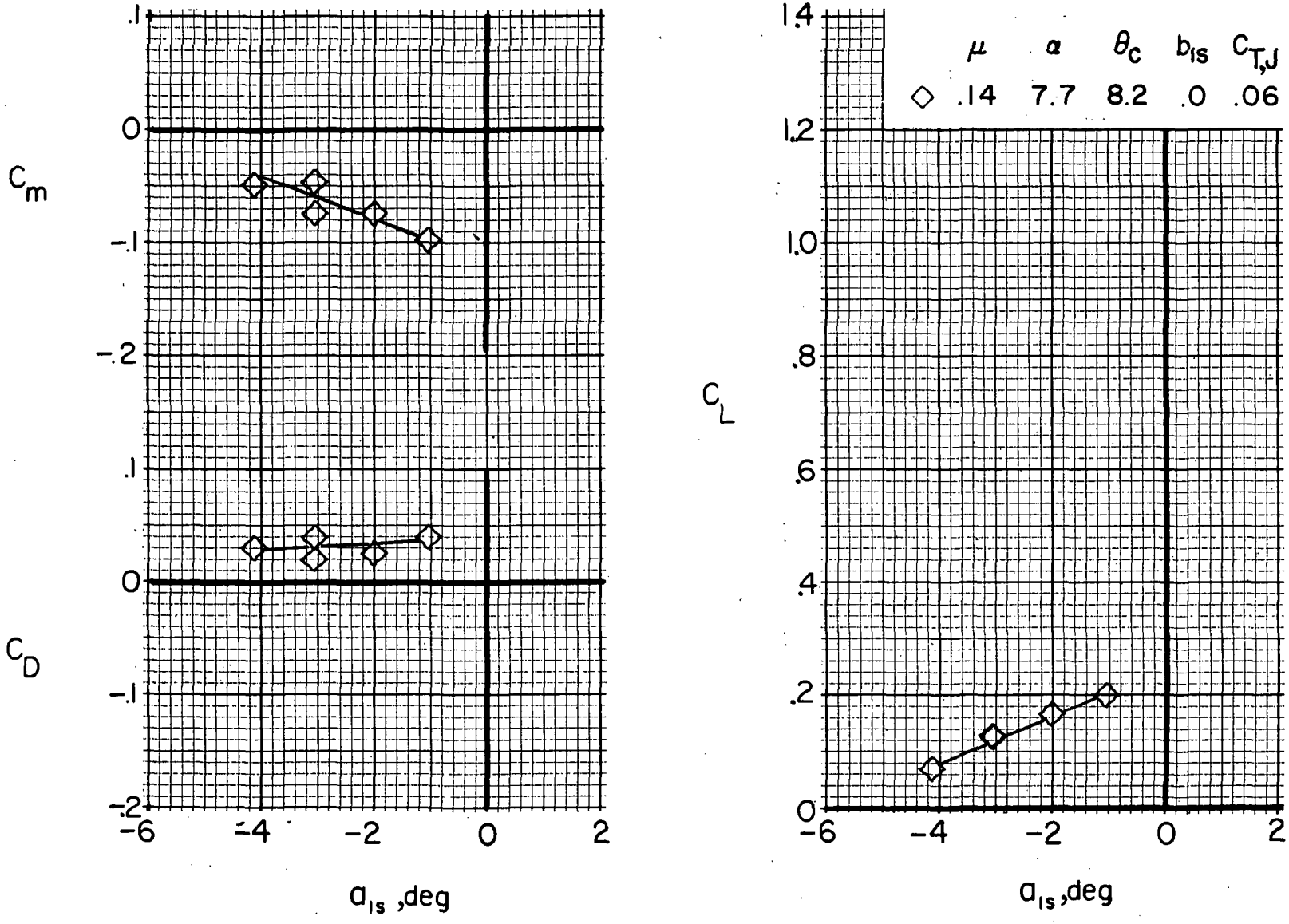

(a) Concluded.

Figure 8.- Continued.

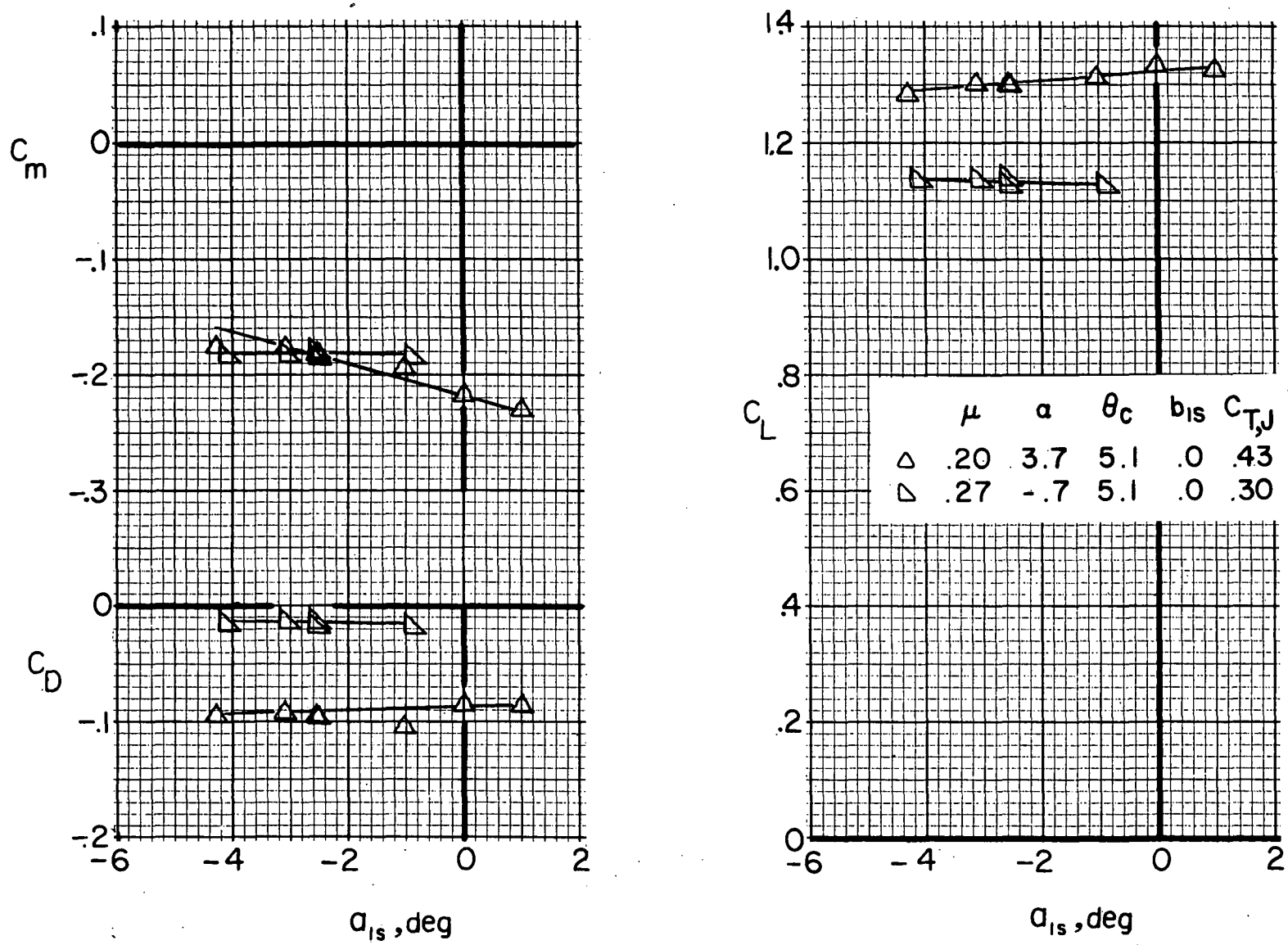

(b) $i_w = 7.5°$; $\delta_f = 30°$.

Figure 8.- Continued.

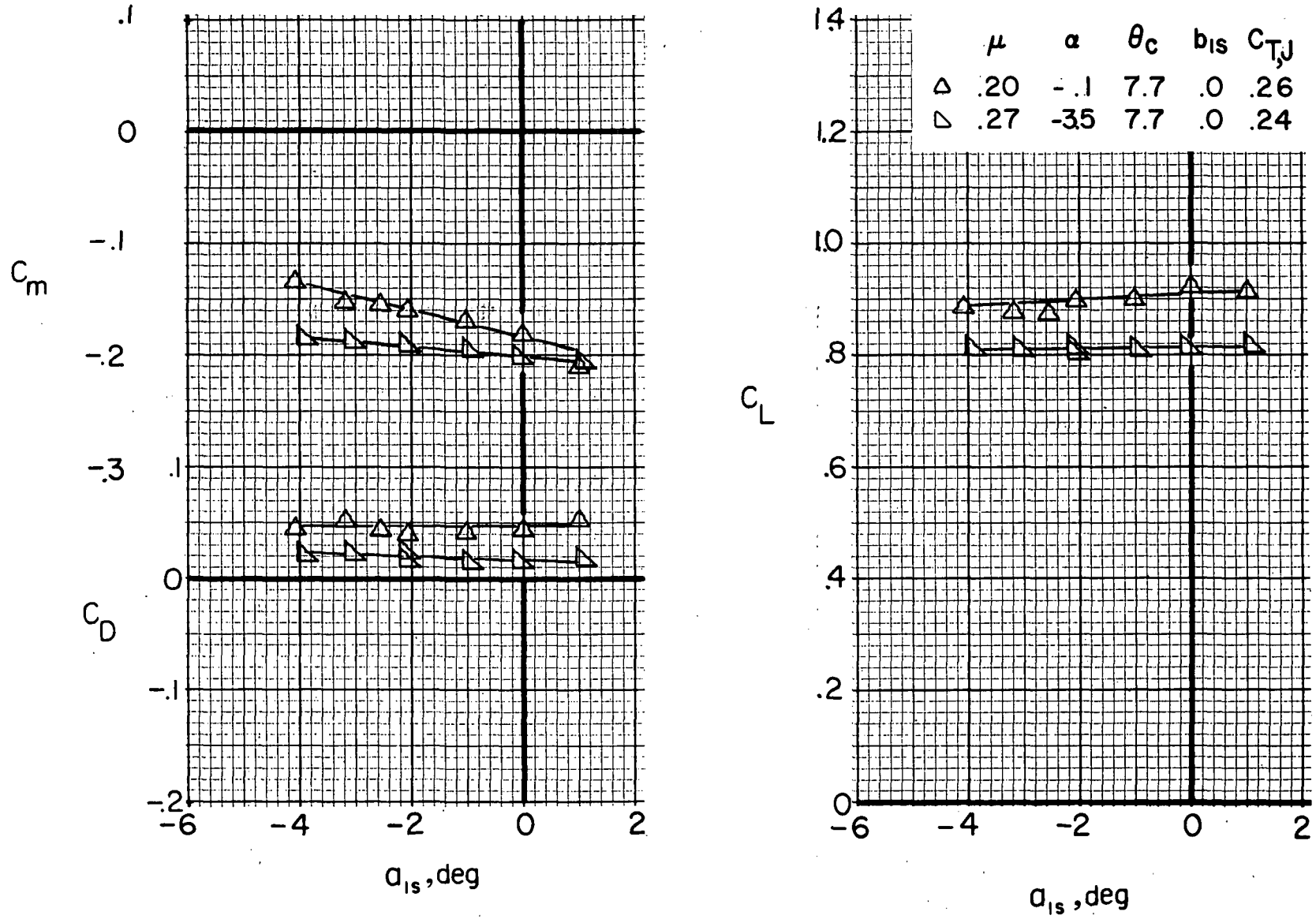

(b) Concluded.

Figure 8.- Concluded.

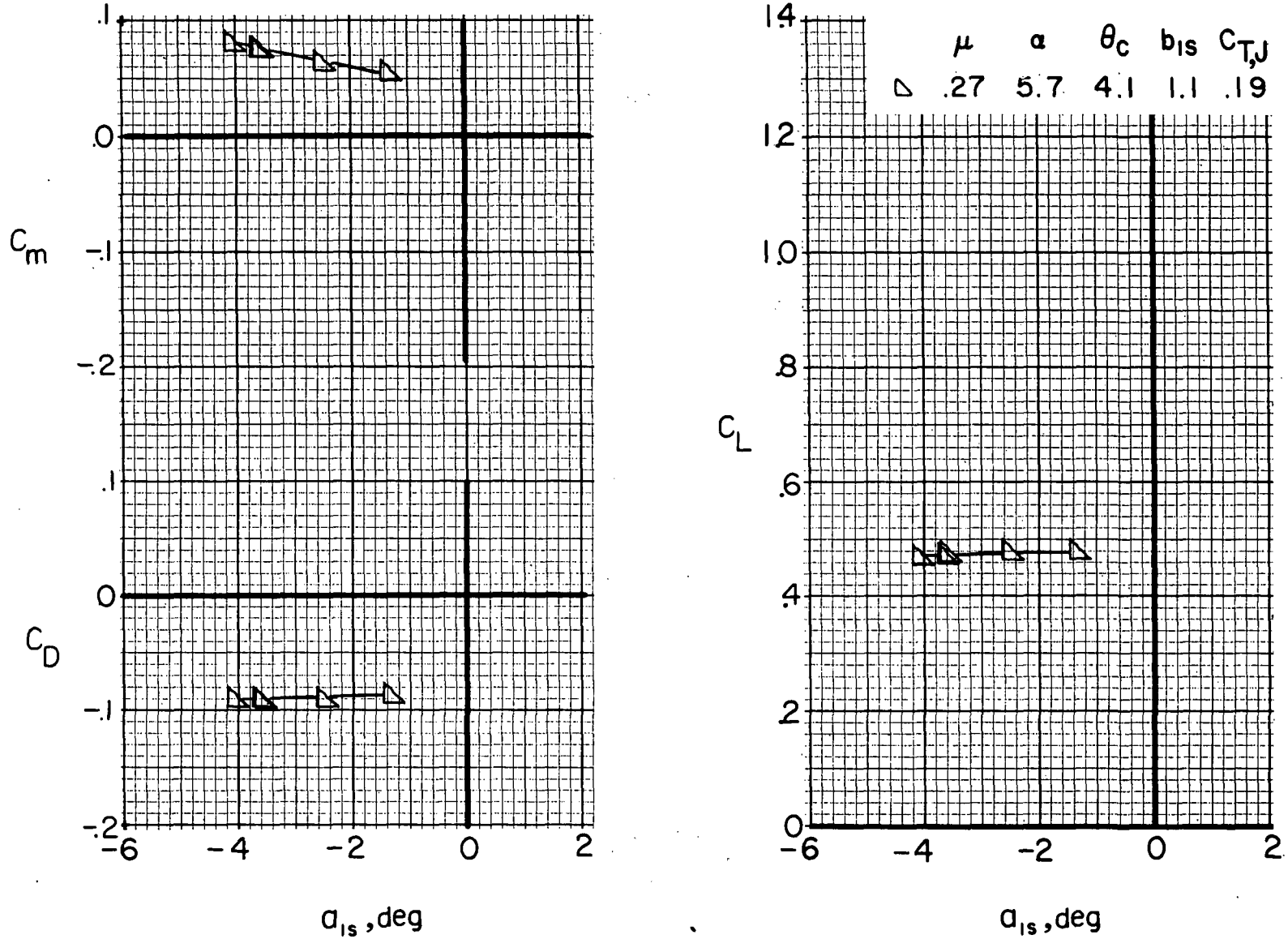

(a) $i_w = 0^\circ$; $\delta_f = 0^\circ$.

Figure 9.- Variation of airframe longitudinal aerodynamic characteristics for compound helicopter (rotor forces and moments removed) with longitudinal rotor flapping at several advance ratios. $\delta_3 = -2.0^\circ$; $i_t = 3^\circ$. (α, θ_c, and b_{ls} are in degrees.)

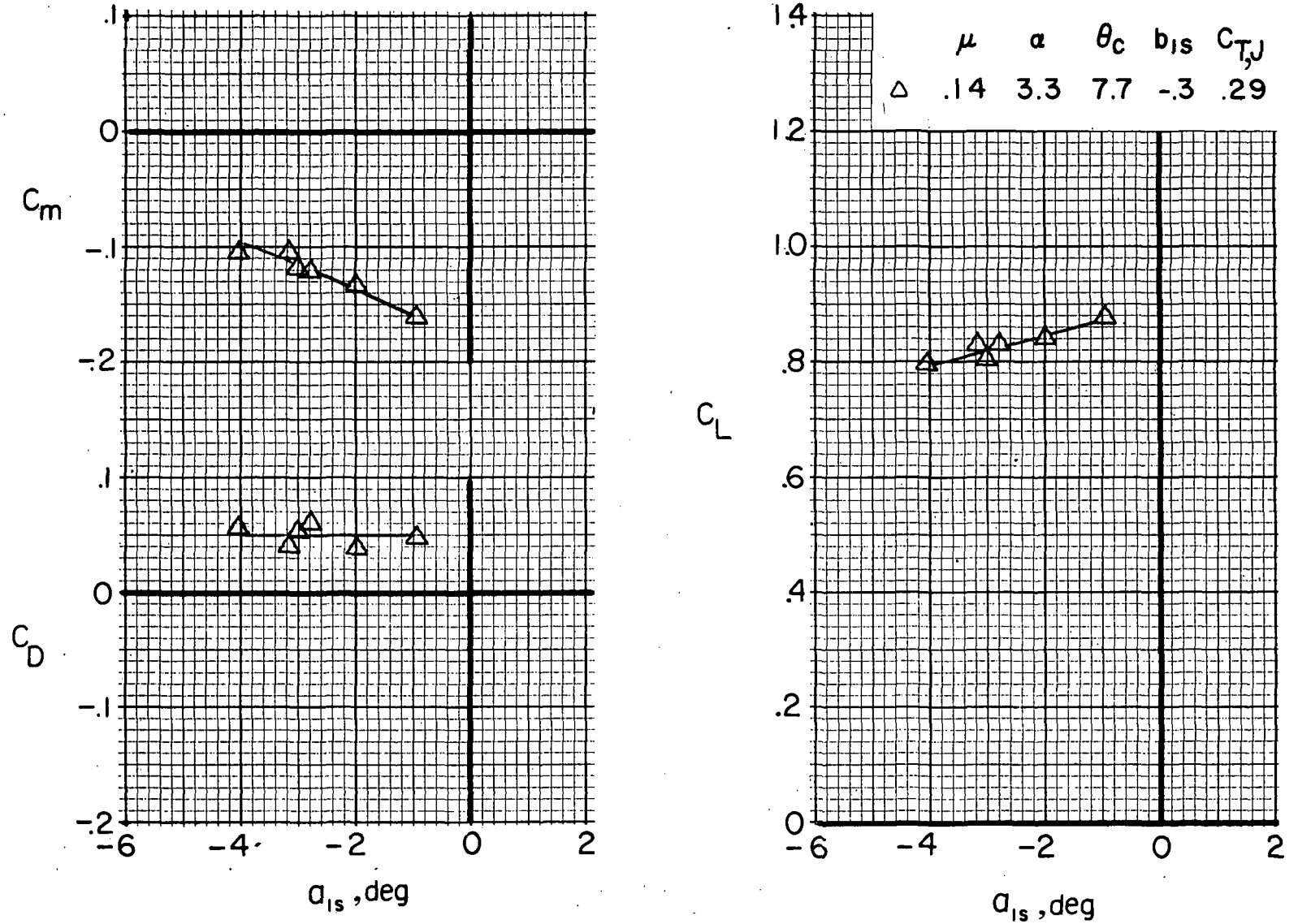

(b) $i_w = 7.5°$; $\delta_f = 30°$.

Figure 9.- Concluded.

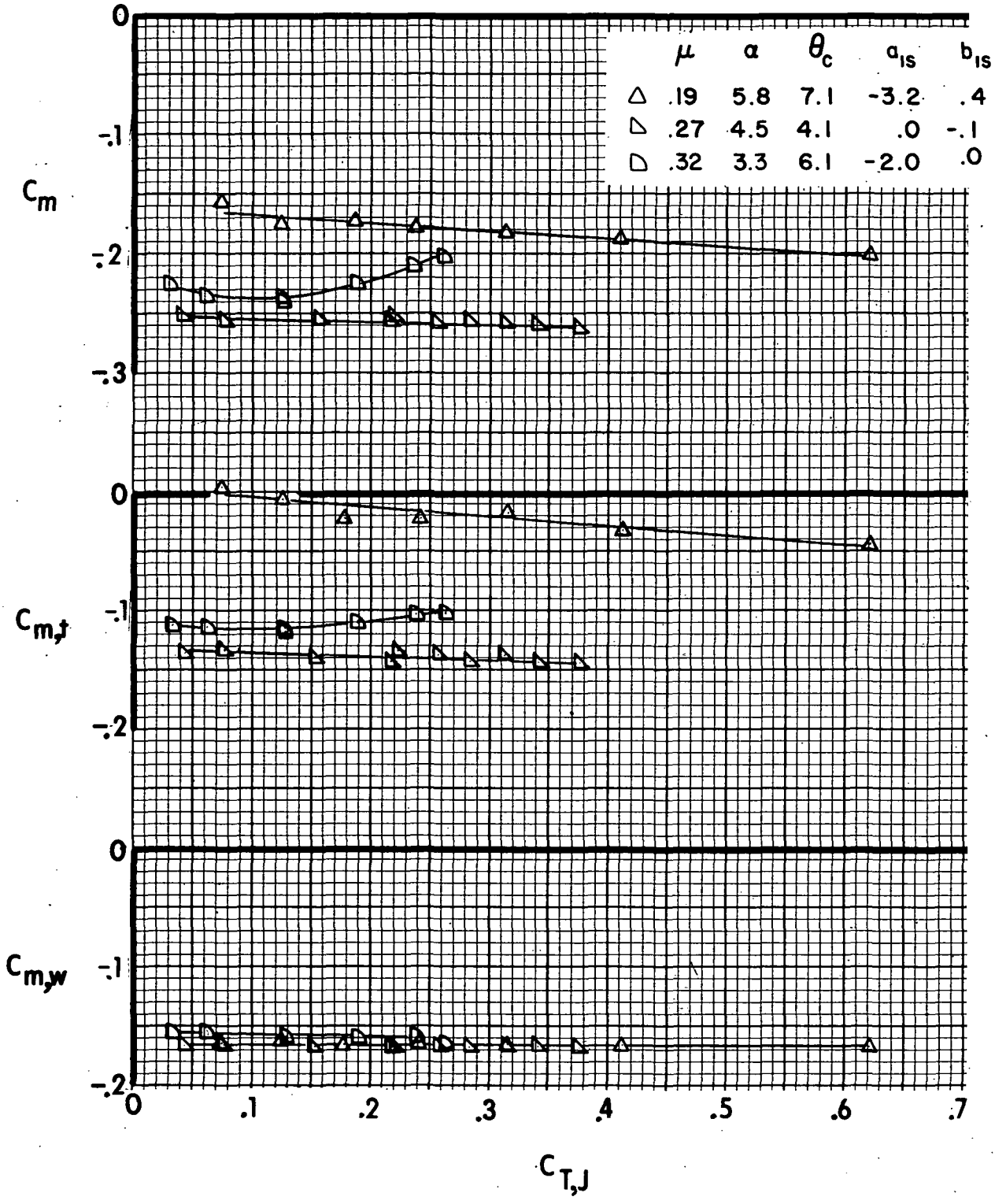

Figure 10.- Variation of pitching-moment coefficient with auxiliary engine thrust coefficient for several advance ratios. $i_w = 0^\circ$; $\delta_f = 0^\circ$; $\delta_3 = -27.6^\circ$; $i_t = 3^\circ$. (α, θ_c, a_{1s}, and b_{1s} are in degrees.)

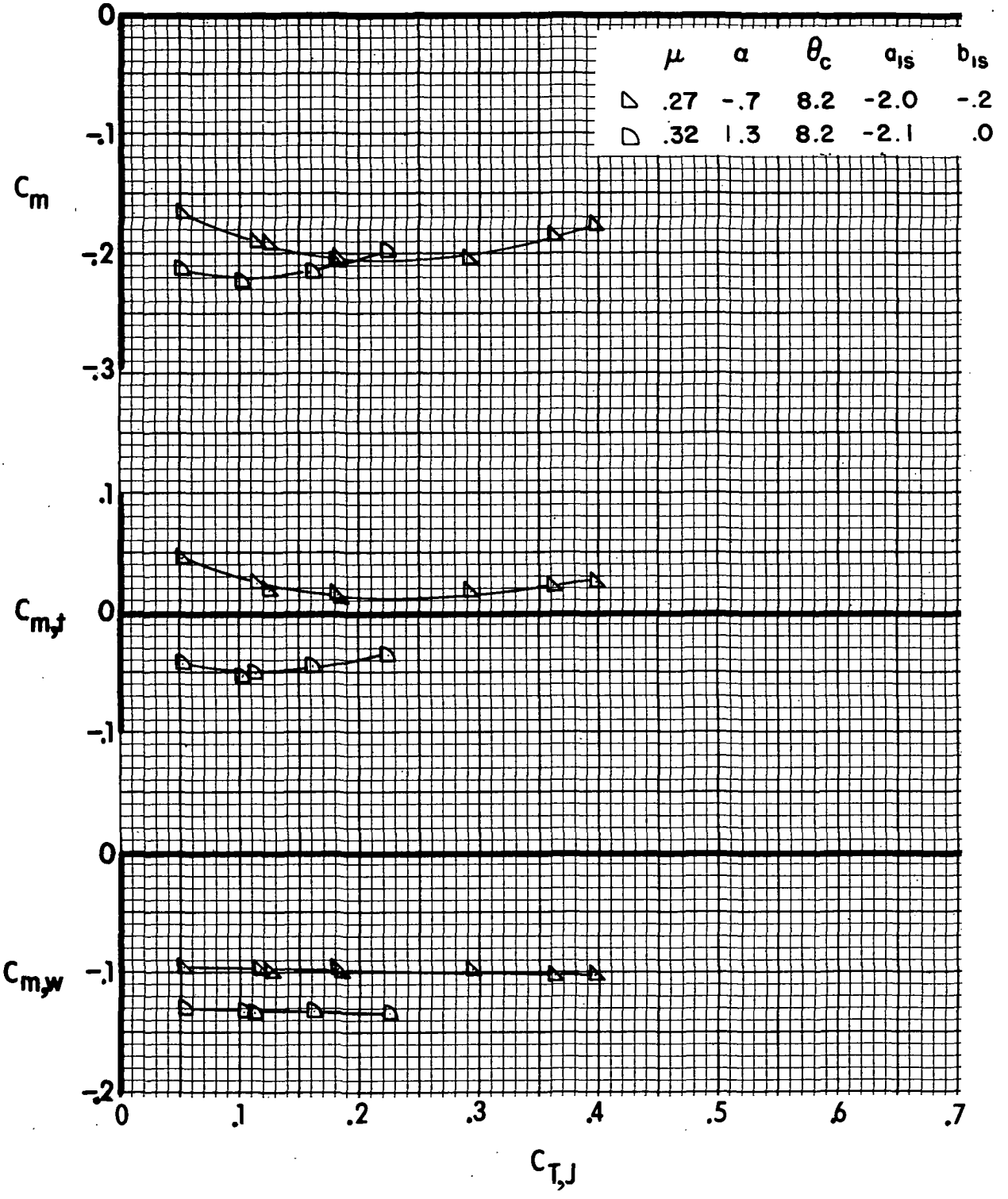

Figure 10.- Concluded.

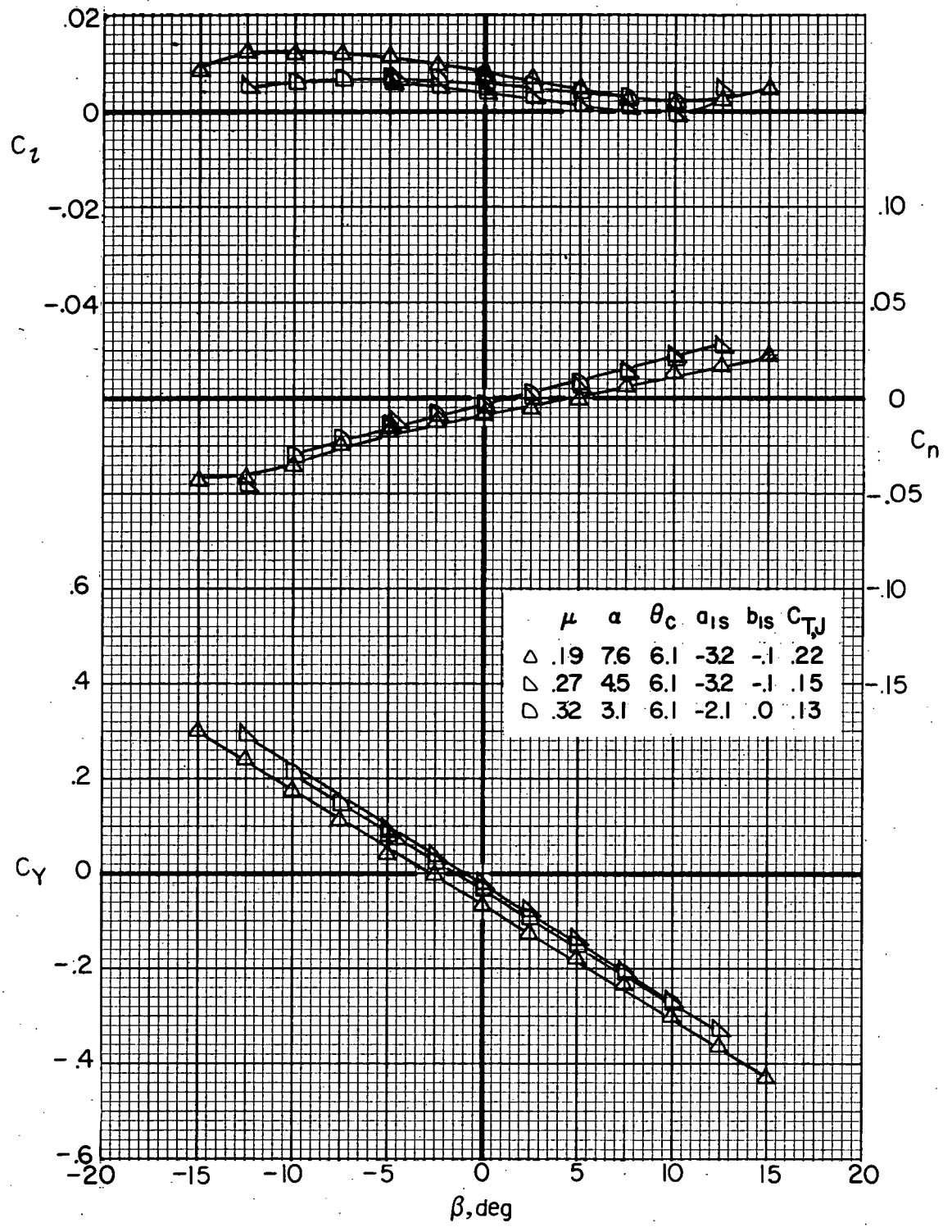

(a) $i_w = 0^\circ$; $\delta_f = 0^\circ$.

Figure 11.- Variation of airframe lateral aerodynamic characteristics for compound helicopter (rotor forces and moments removed) with angle of sideslip for several advance ratios. $\delta_3 = -27.6^\circ$; $i_t = 3^\circ$. (α, θ_c, a_{1s}, and b_{1s} are in degrees.)

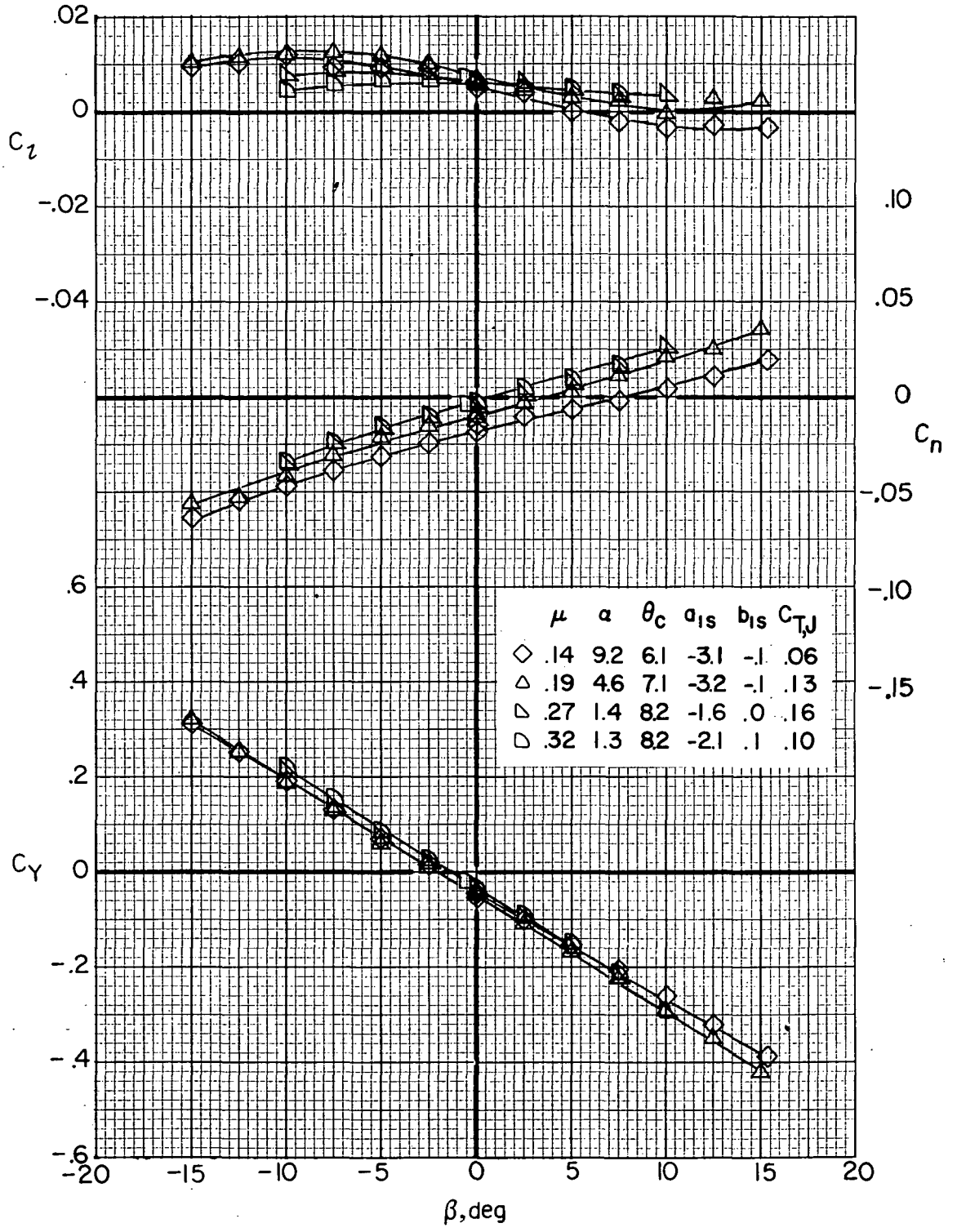

(a) Concluded.

Figure 11.- Continued.

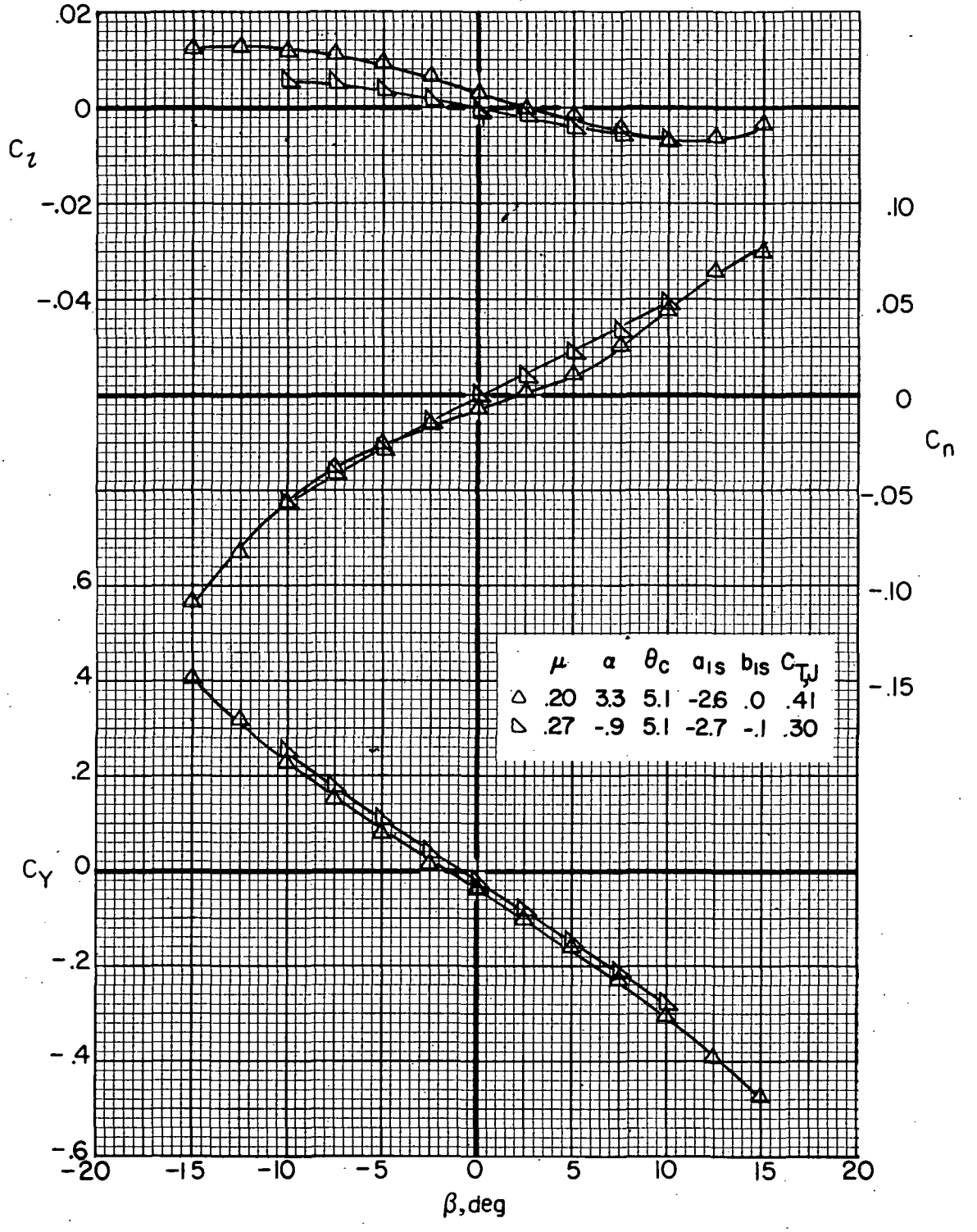

(b) $i_w = 7.5^\circ$; $\delta_f = 30^\circ$.

Figure 11.- Continued.

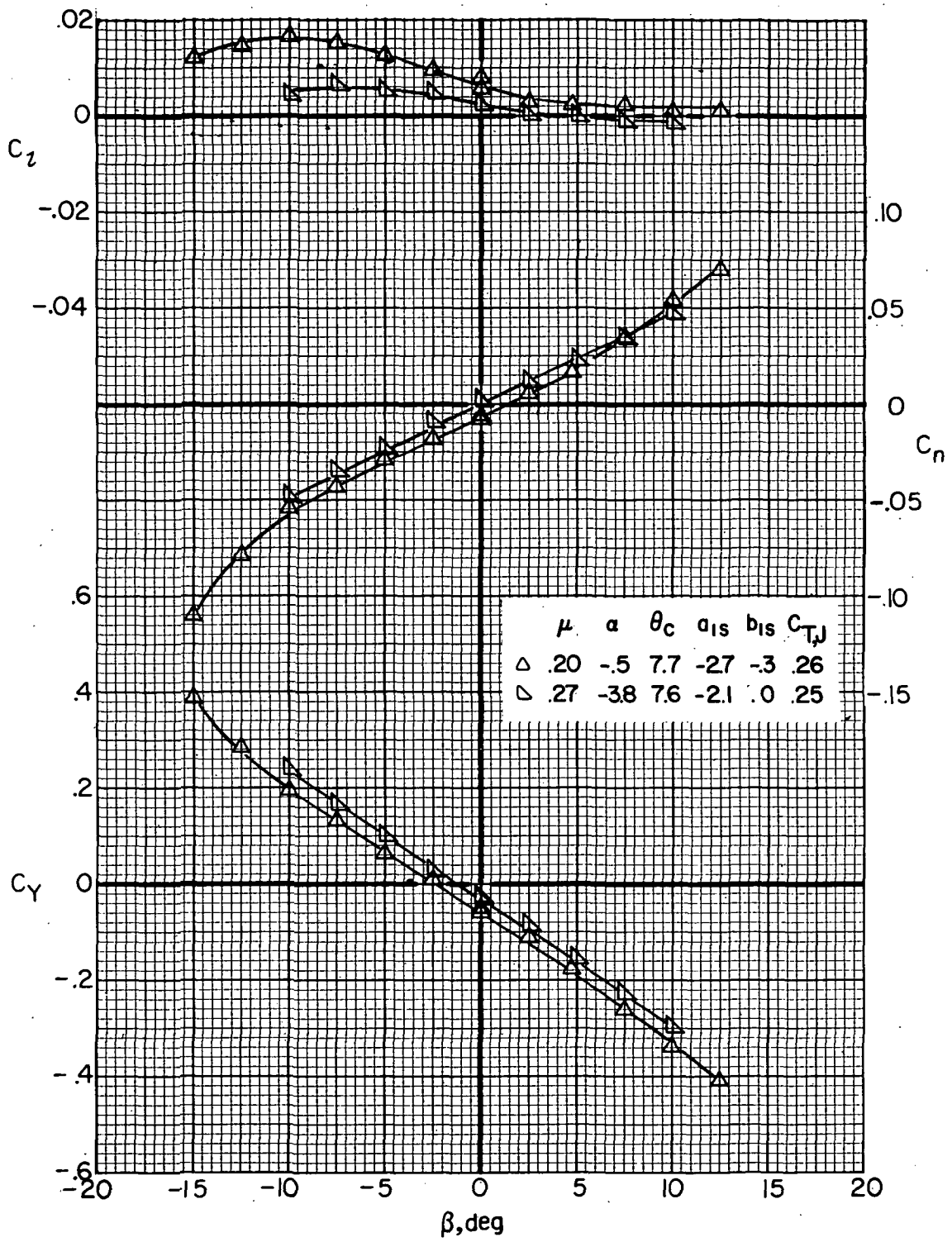

(b) Concluded.

Figure 11.- Concluded.

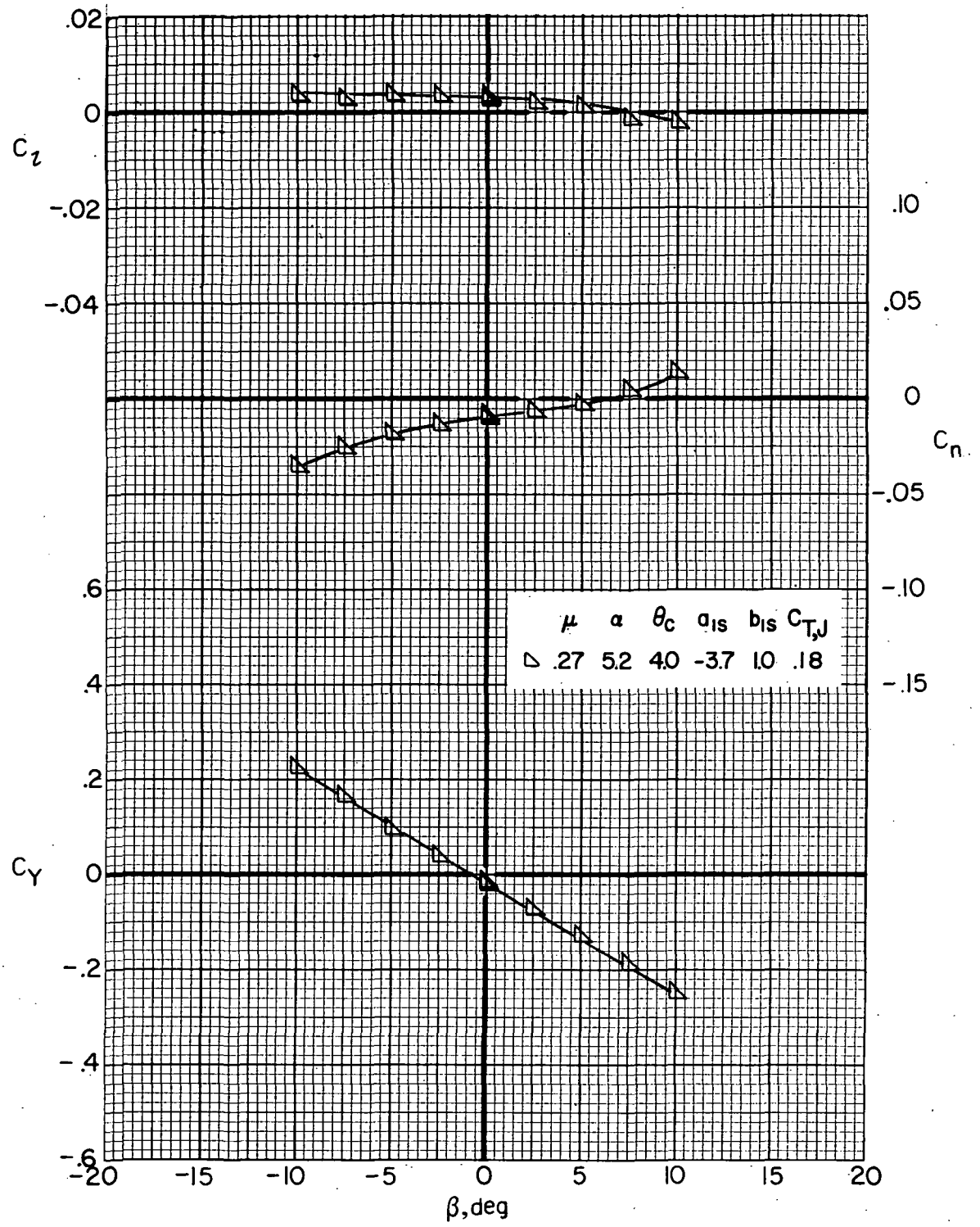

(a) $i_w = 0^\circ$; $\delta_f = 0^\circ$.

Figure 12.- Variation of airframe lateral aerodynamic characteristics for compound helicopter (rotor forces and moments removed) with angle of sideslip for several advance ratios. $\delta_3 = -2.0^\circ$; $i_t = 3^\circ$. (α, θ_c, a_{1s}, and b_{1s} are in degrees.)

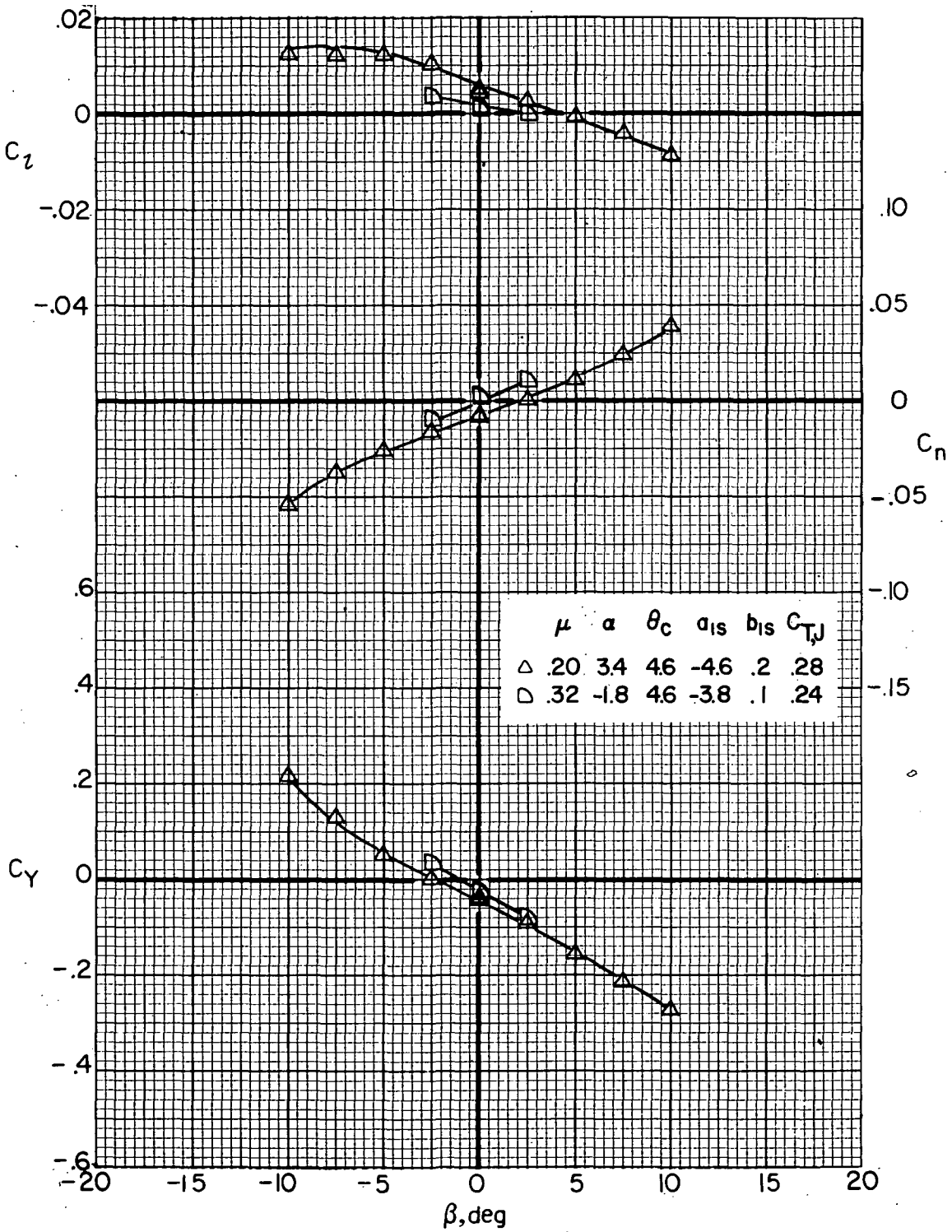

(b) $i_w = 7.5^\circ$; $\delta_f = 30^\circ$.

Figure 12.- Continued.

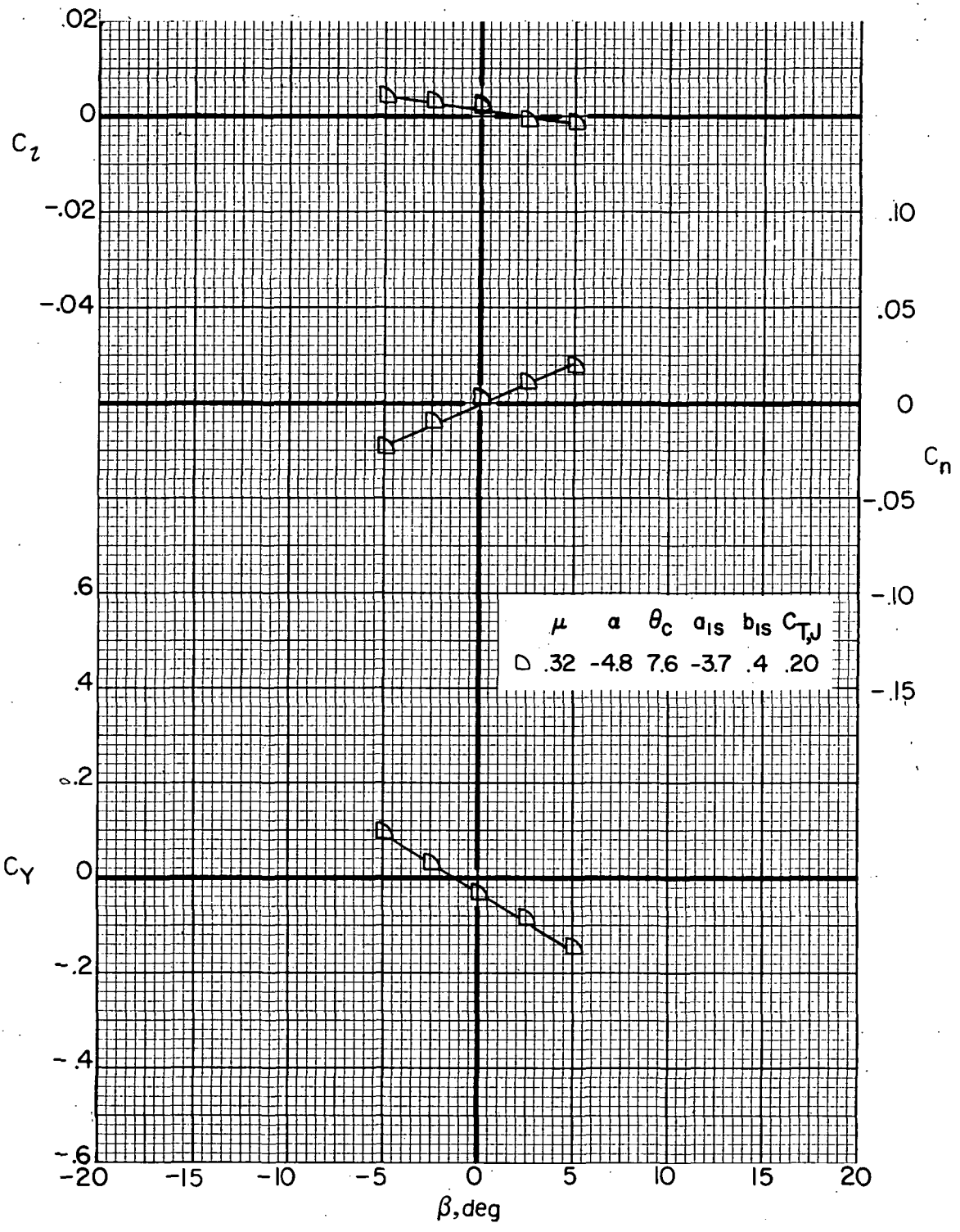

(b) Concluded.

Figure 12.- Concluded.

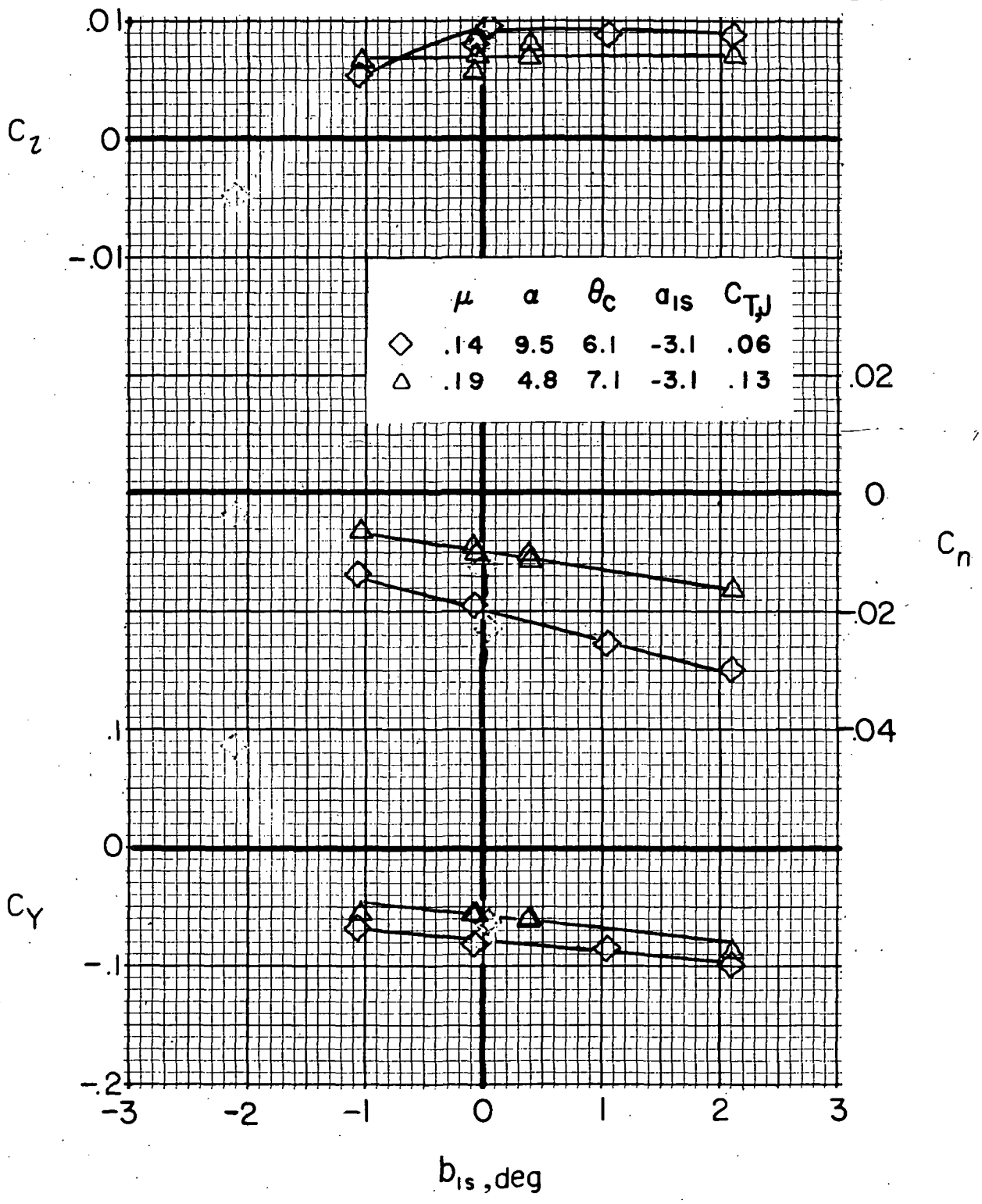

Figure 13.- Variation of airframe lateral aerodynamic characteristics for compound helicopter (rotor forces and moments removed) with rotor lateral flapping at several advance ratios. $\delta_3 = -27.6^\circ$; $i_t = 3^\circ$; $i_w = 0^\circ$; $\delta_f = 0^\circ$. (α, θ_c, and a_{1s} are in degrees.)

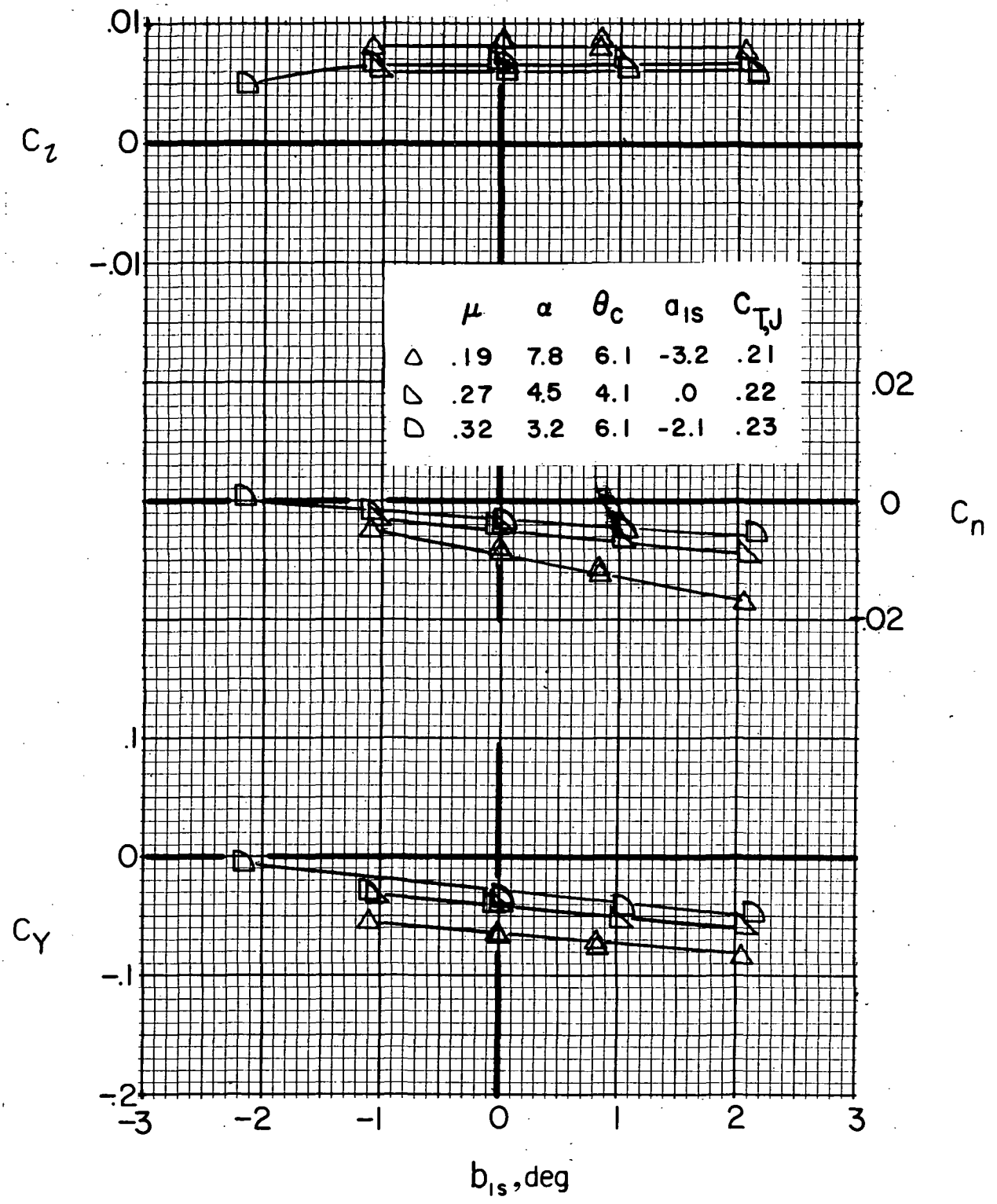

Figure 13.- Concluded.

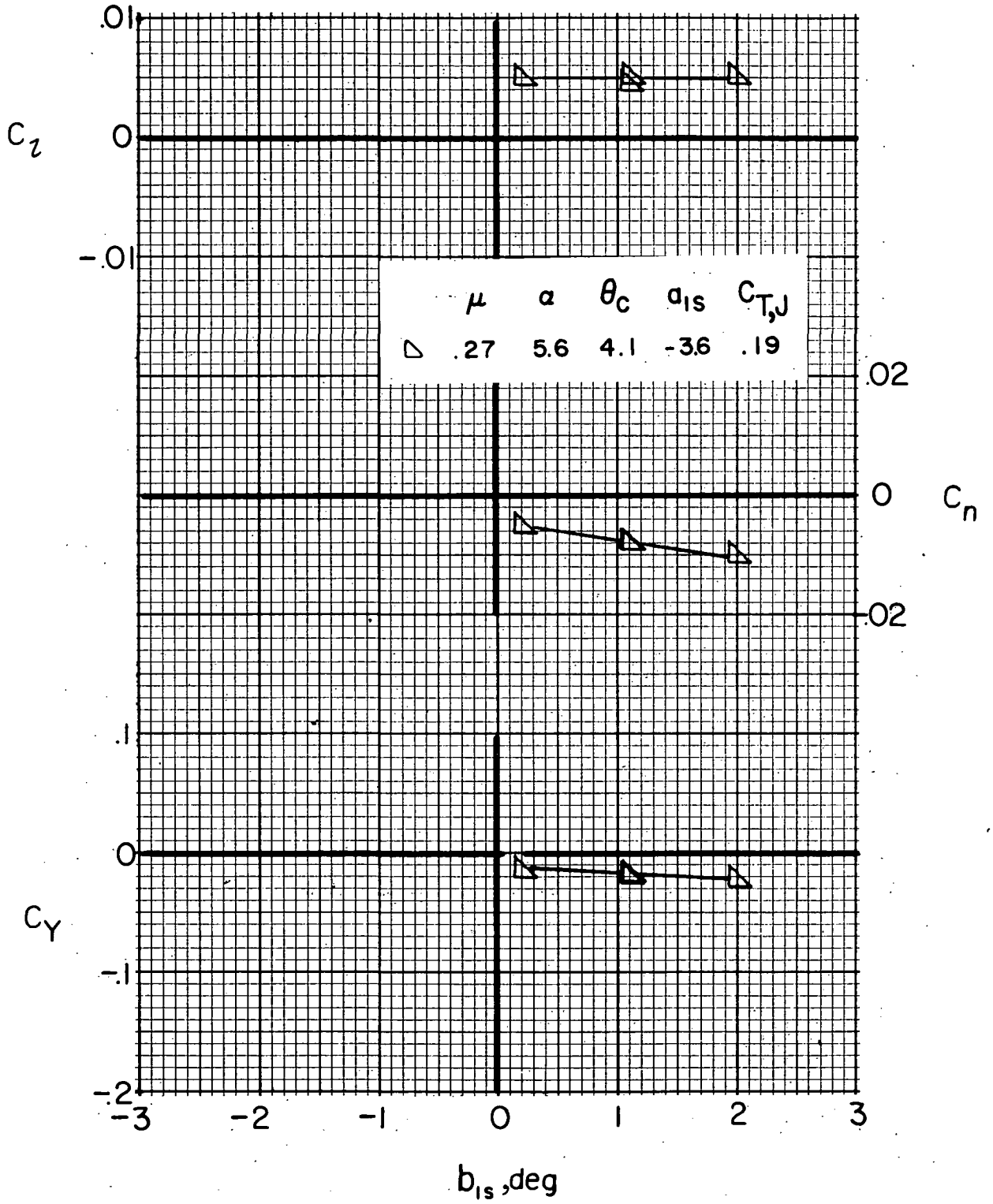

(a) $i_w = 0^\circ$; $\delta_f = 0^\circ$.

Figure 14.- Variation of airframe lateral aerodynamic characteristics for compound helicopter (rotor forces and moments removed) with lateral rotor flapping at several advance ratios. $\delta_3 = -2.0^\circ$; $i_t = 3^\circ$. (α, θ_c, and a_{ls} are in degrees.)

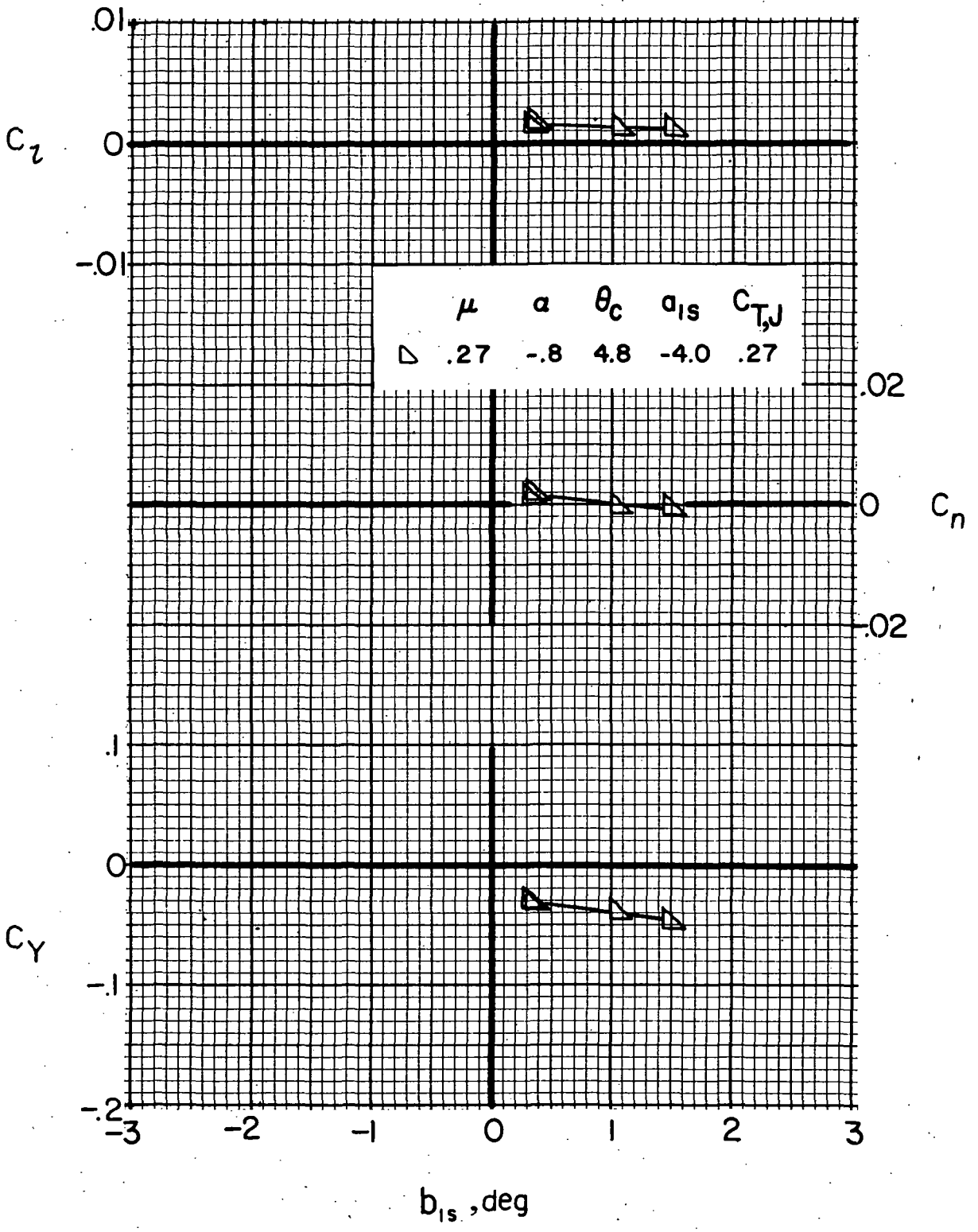

(b) $i_w = 7.5°$; $\delta_f = 30°$.

Figure 14.- Concluded.

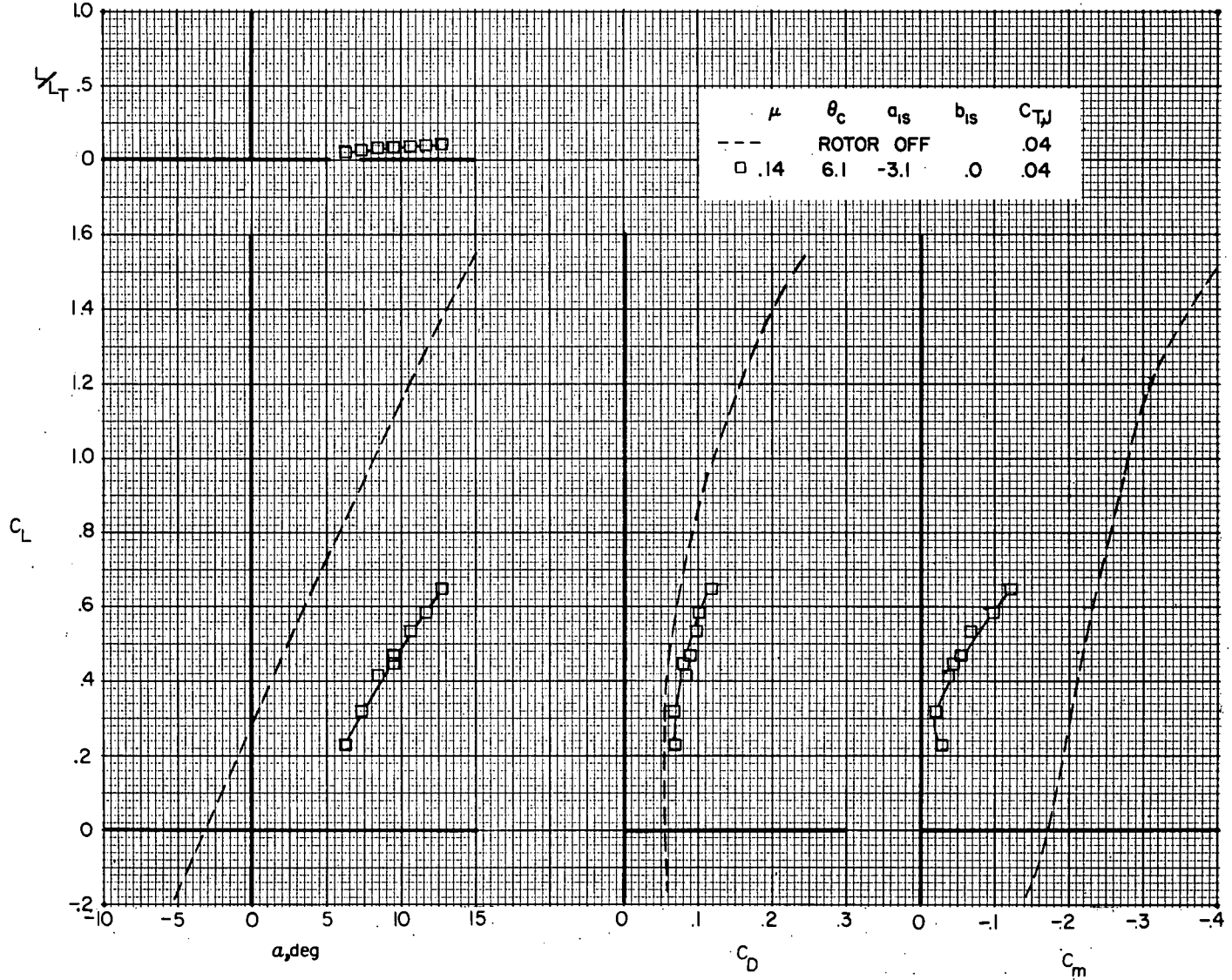

(a) $\mu = 0.14$.

Figure 15.- Comparison of airframe longitudinal aerodynamic characteristics for compound helicopter (rotor forces and moments removed) for rotor on and rotor off. $i_w = 0^\circ$; $\delta_f = 0^\circ$; $i_t = 3^\circ$. (θ_c, a_{ls}, and b_{ls} are in degrees.)

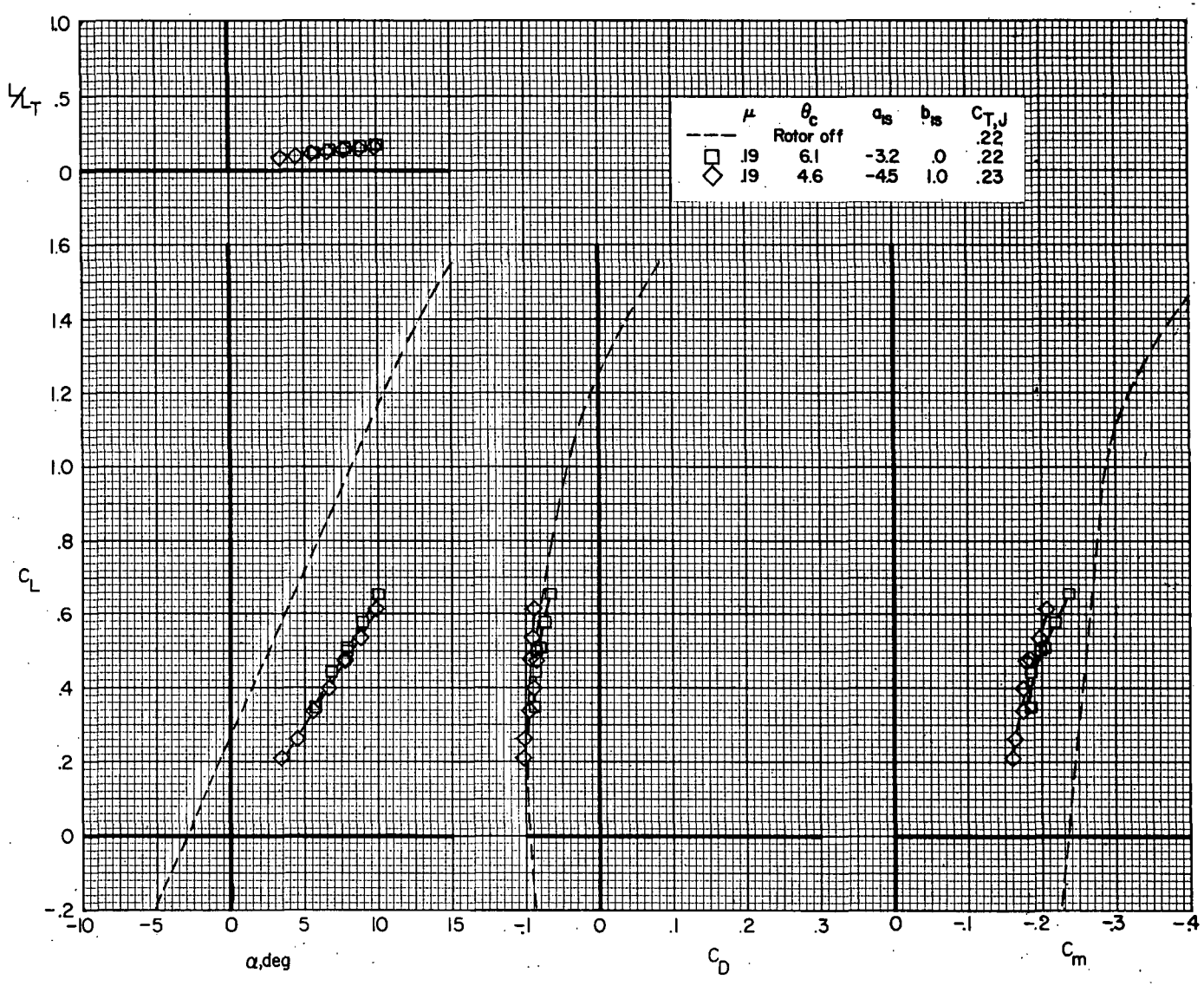

(b) $\mu = 0.19$.

Figure 15.- Continued.

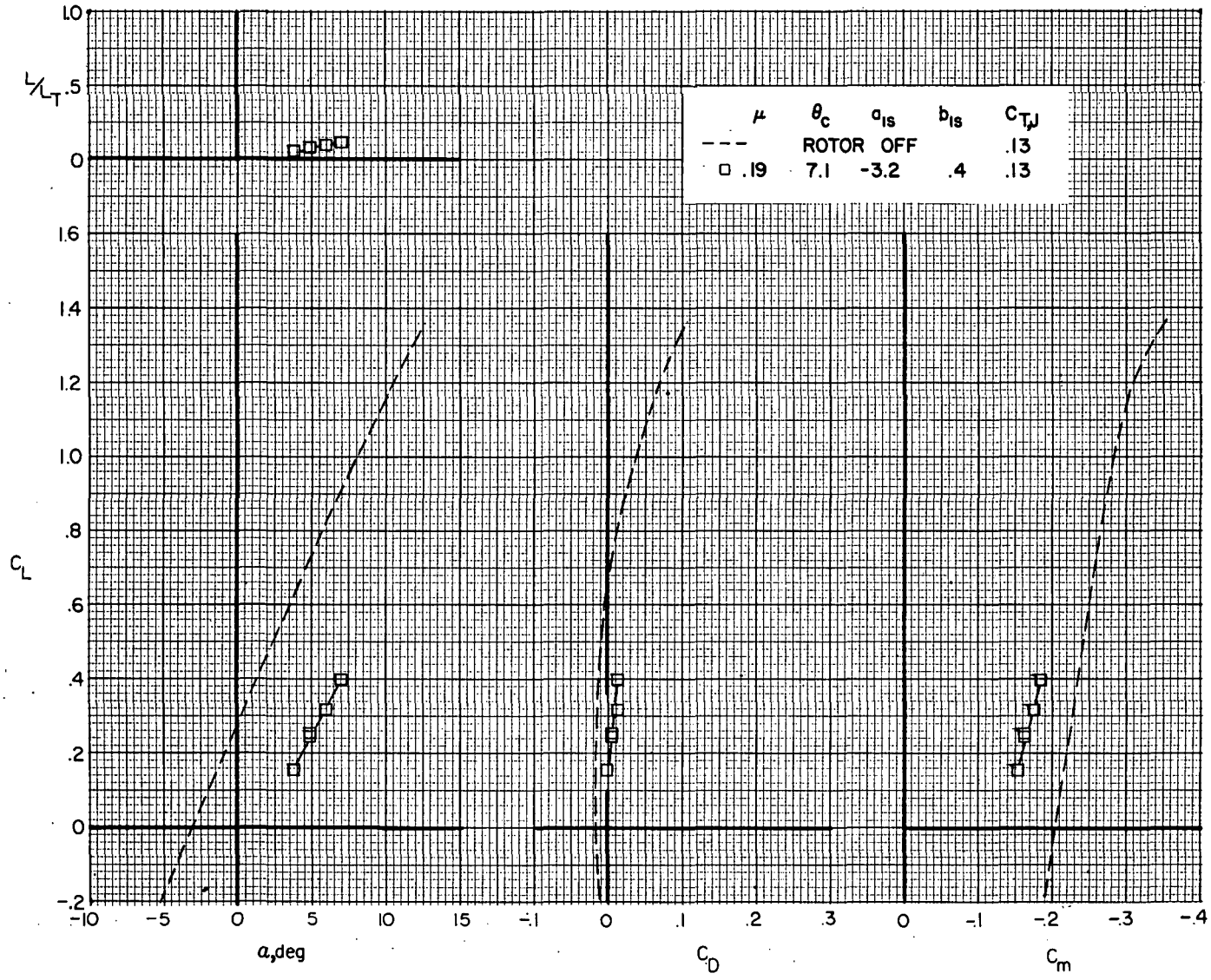

(b) Concluded.

Figure 15.- Continued.

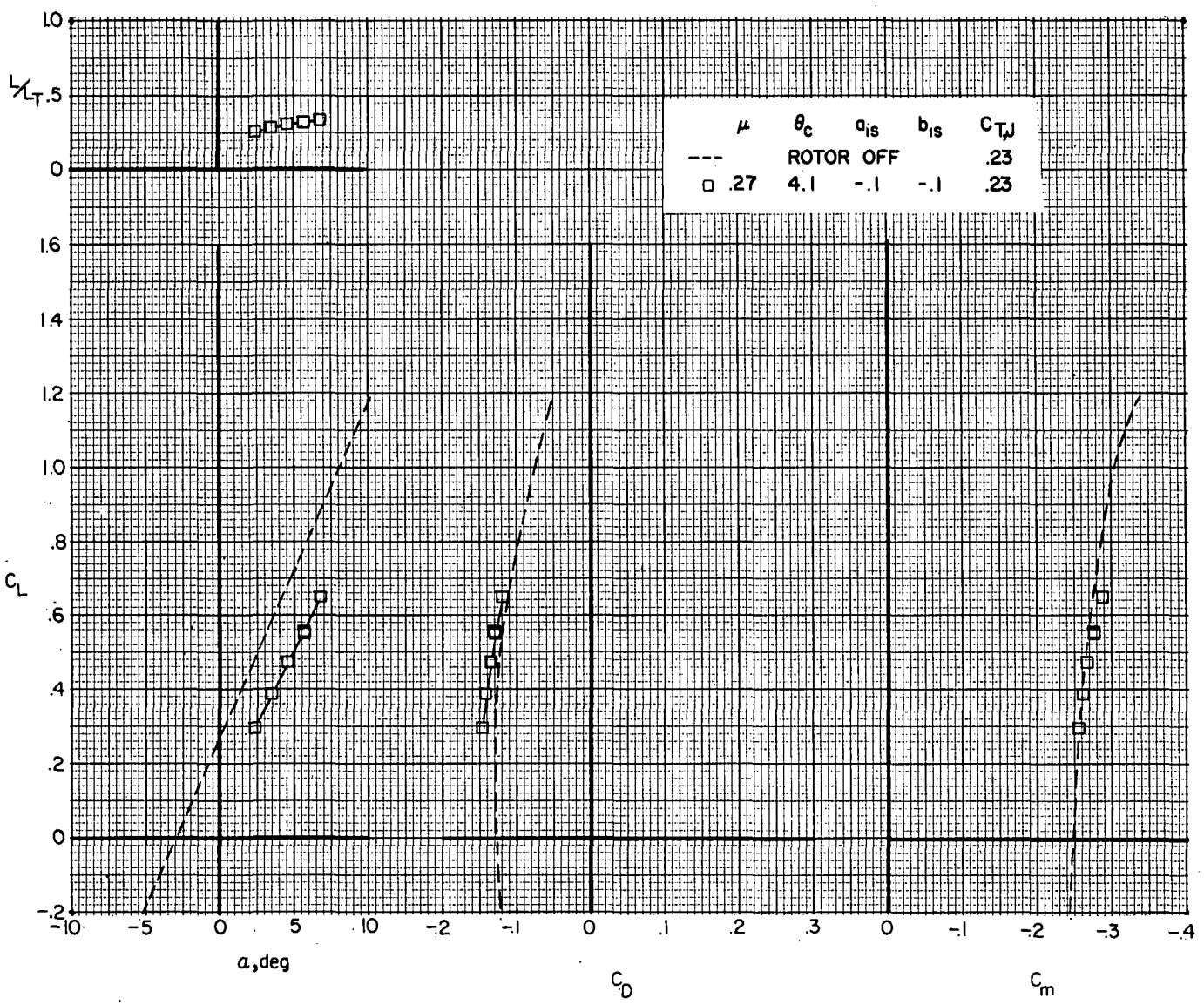

(c) μ = 0.27.

Figure 15.- Continued.

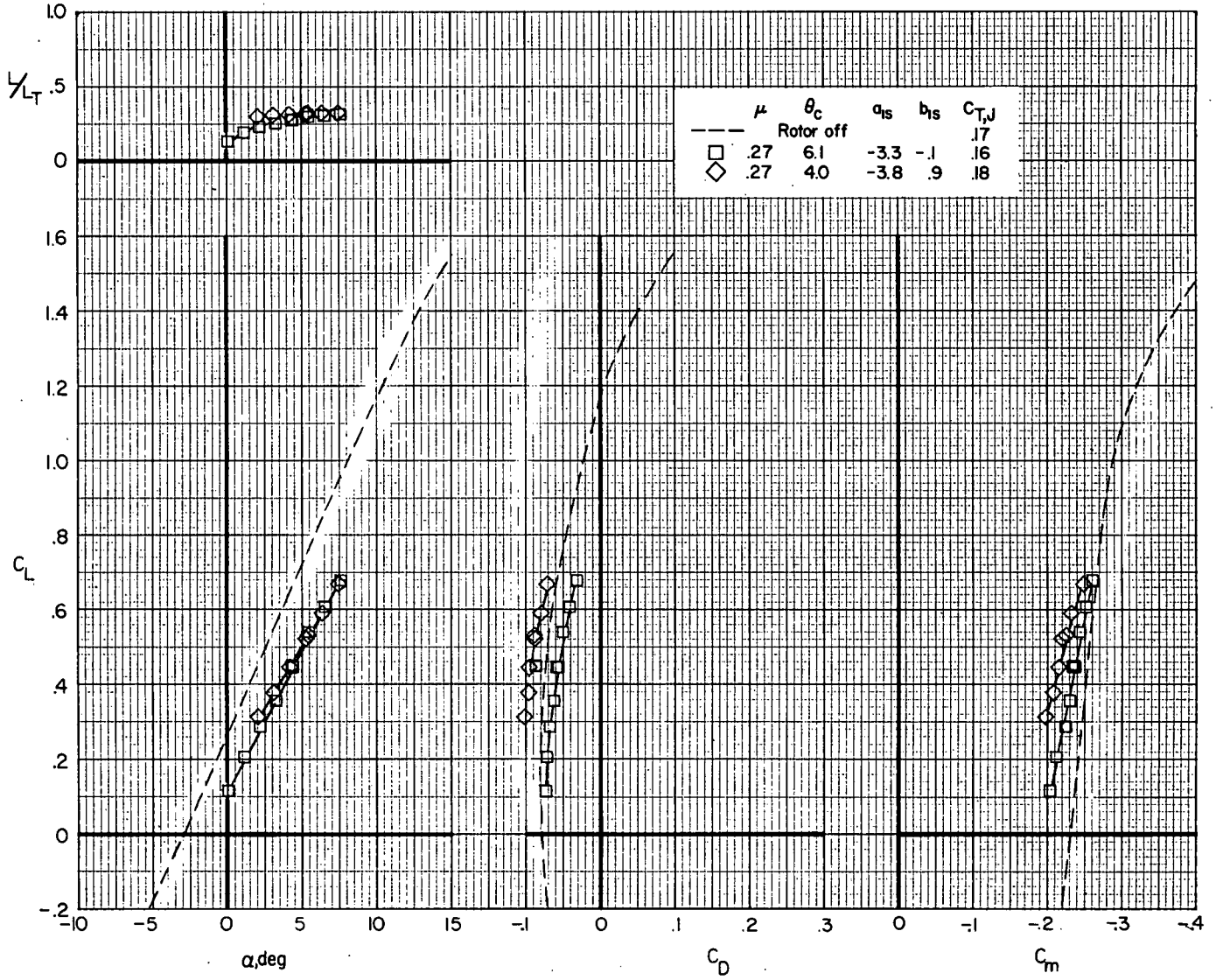

(c) Continued.

Figure 15.- Continued.

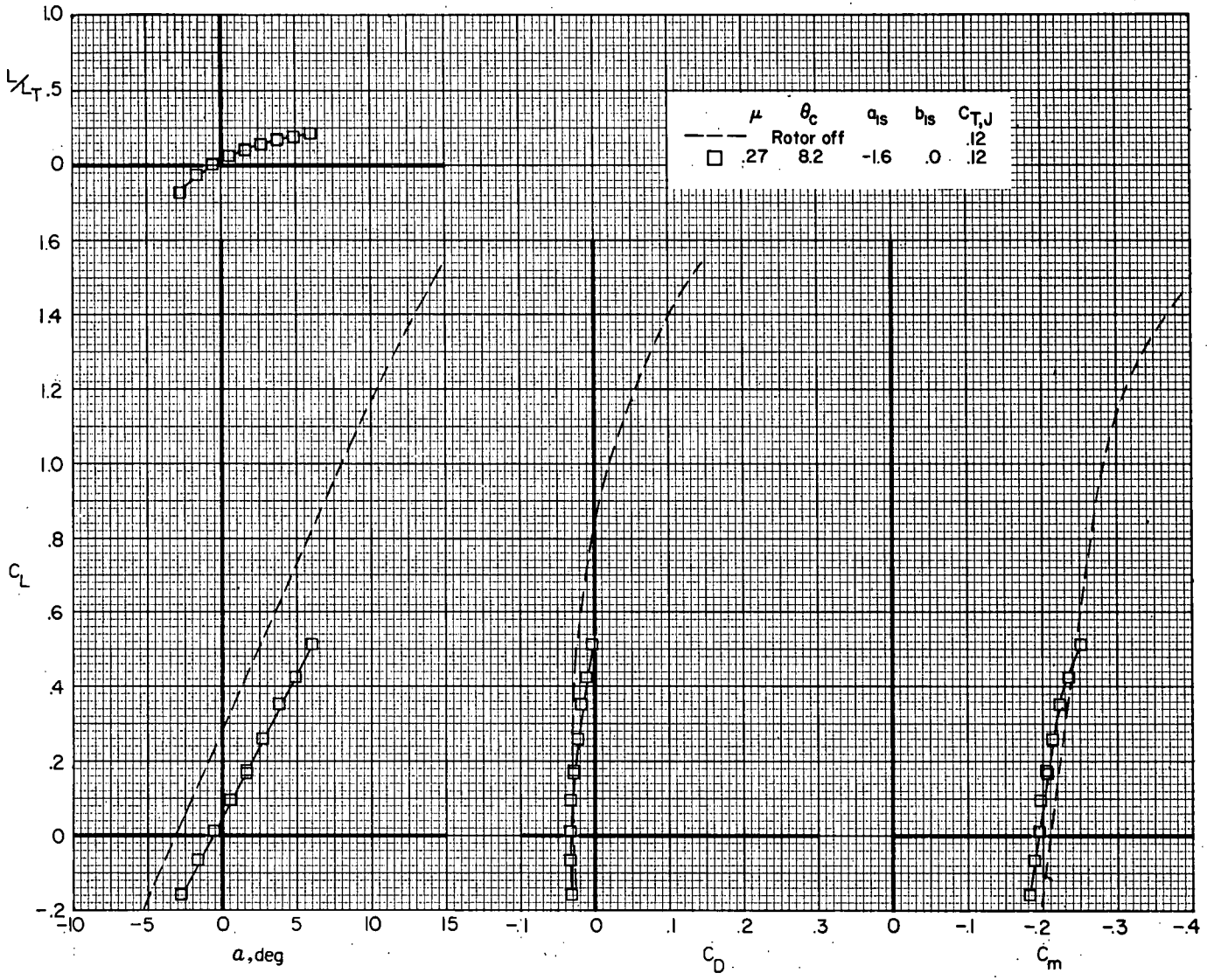

(c) Concluded.

Figure 15.- Continued.

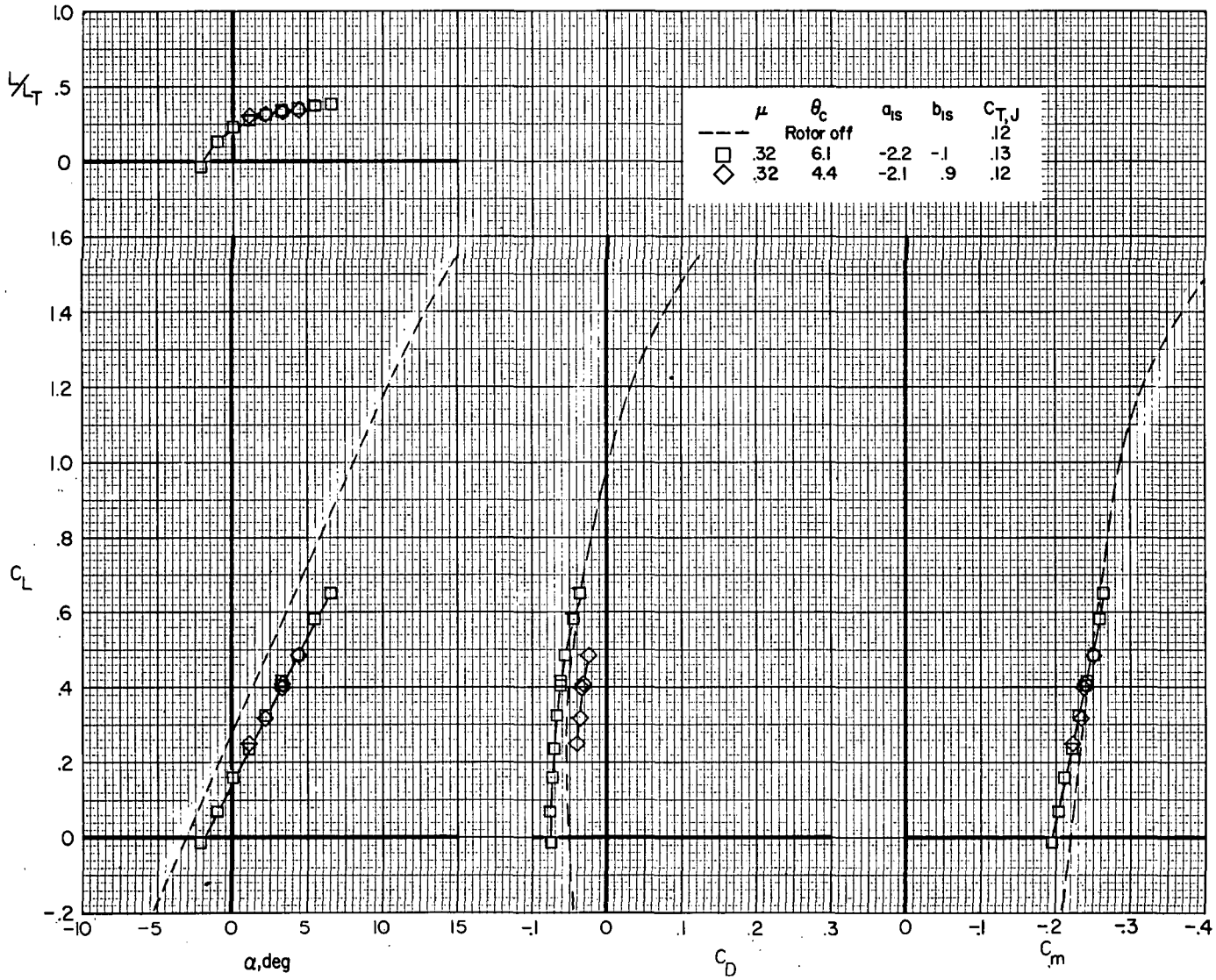

(d) $\mu = 0.32$.

Figure 15.- Continued.

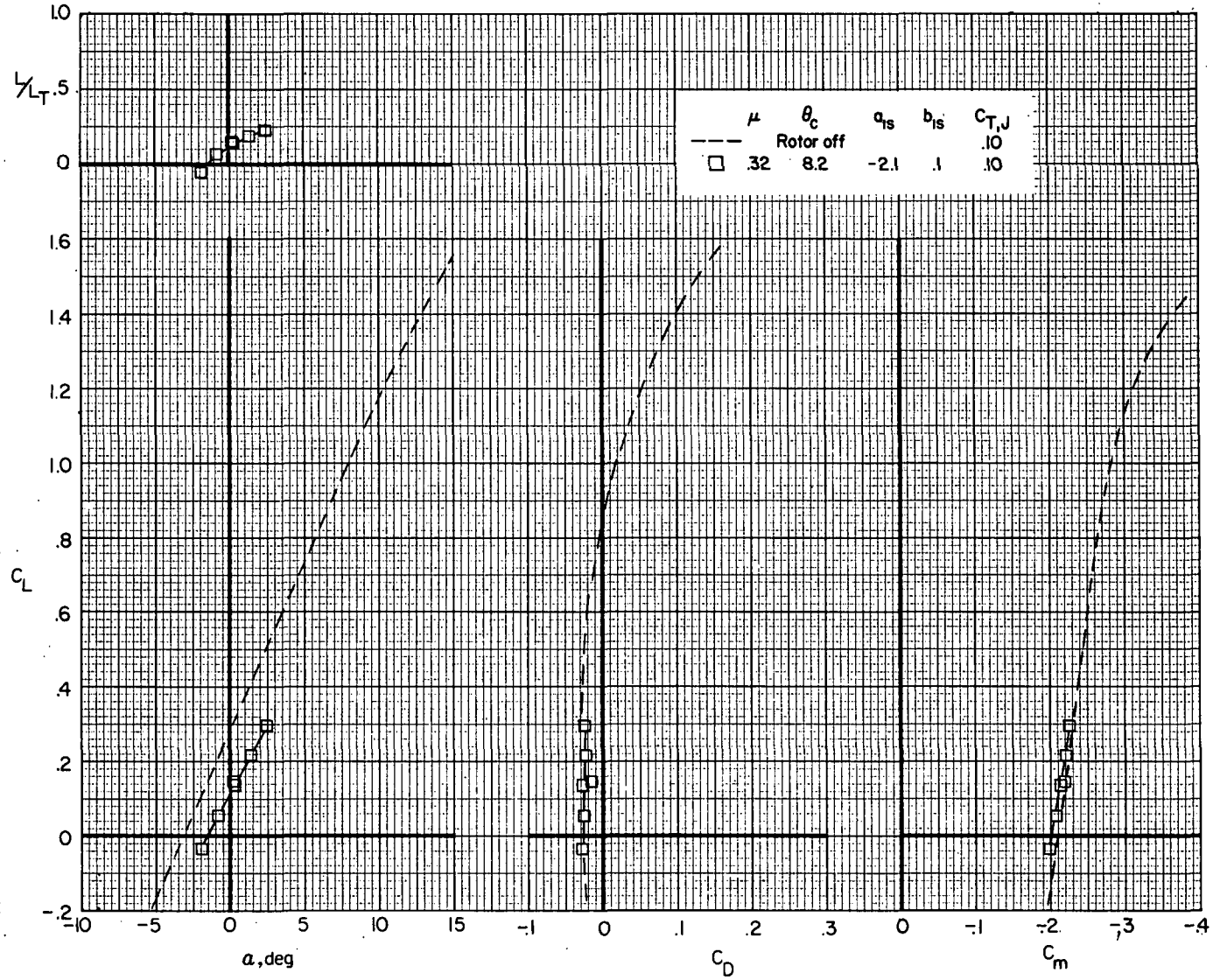

(d) Concluded.

Figure 15.- Concluded.

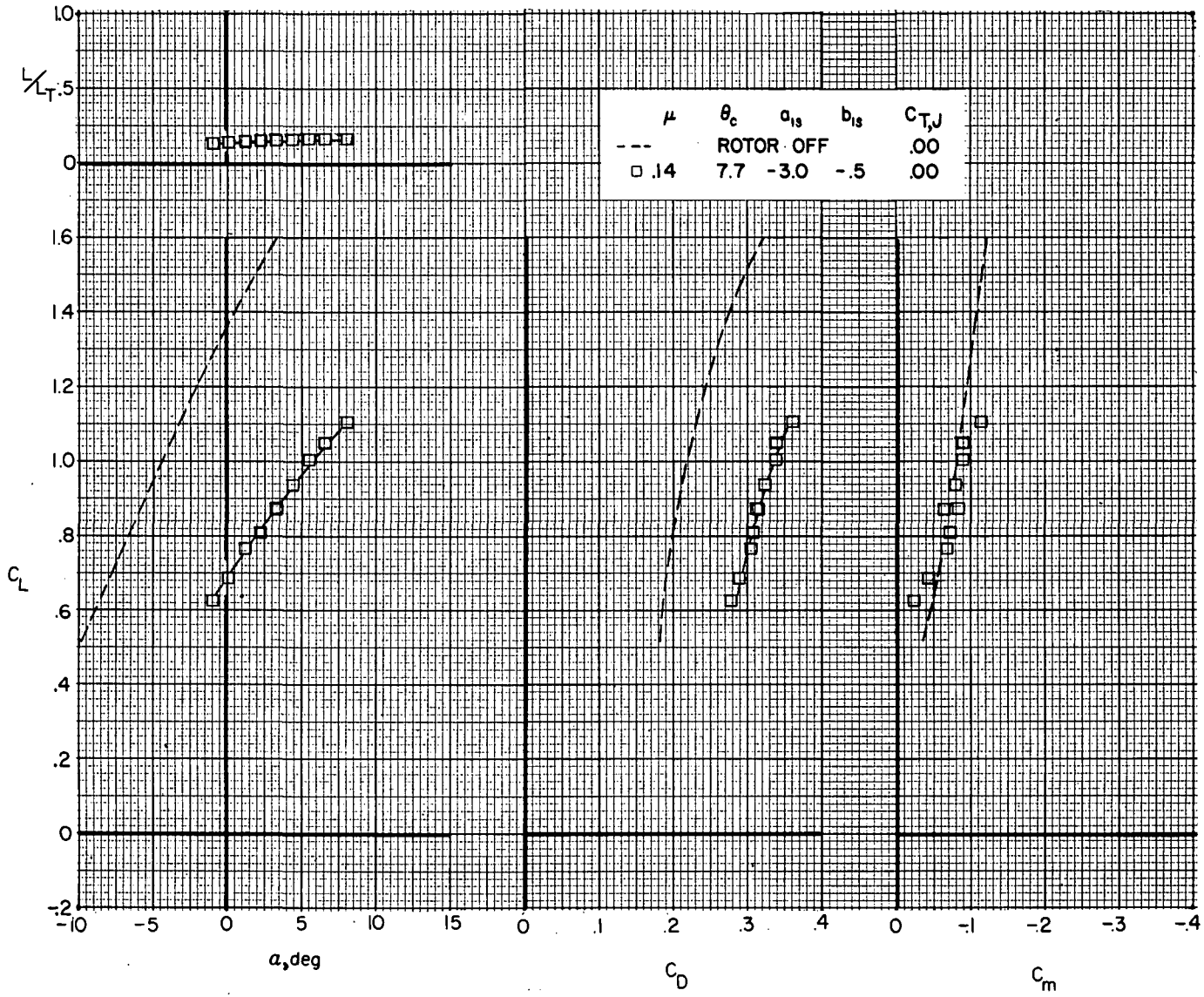

(a) $\mu = 0.14$.

Figure 16.- Comparison of airframe longitudinal aerodynamic characteristics for compound helicopter (rotor forces and moments removed) for rotor on and rotor off. $i_w = 7.5^\circ$; $\delta_f = 30^\circ$; $i_t = 3^\circ$. (θ_c, a_{ls}, and b_{ls} are in degrees.)

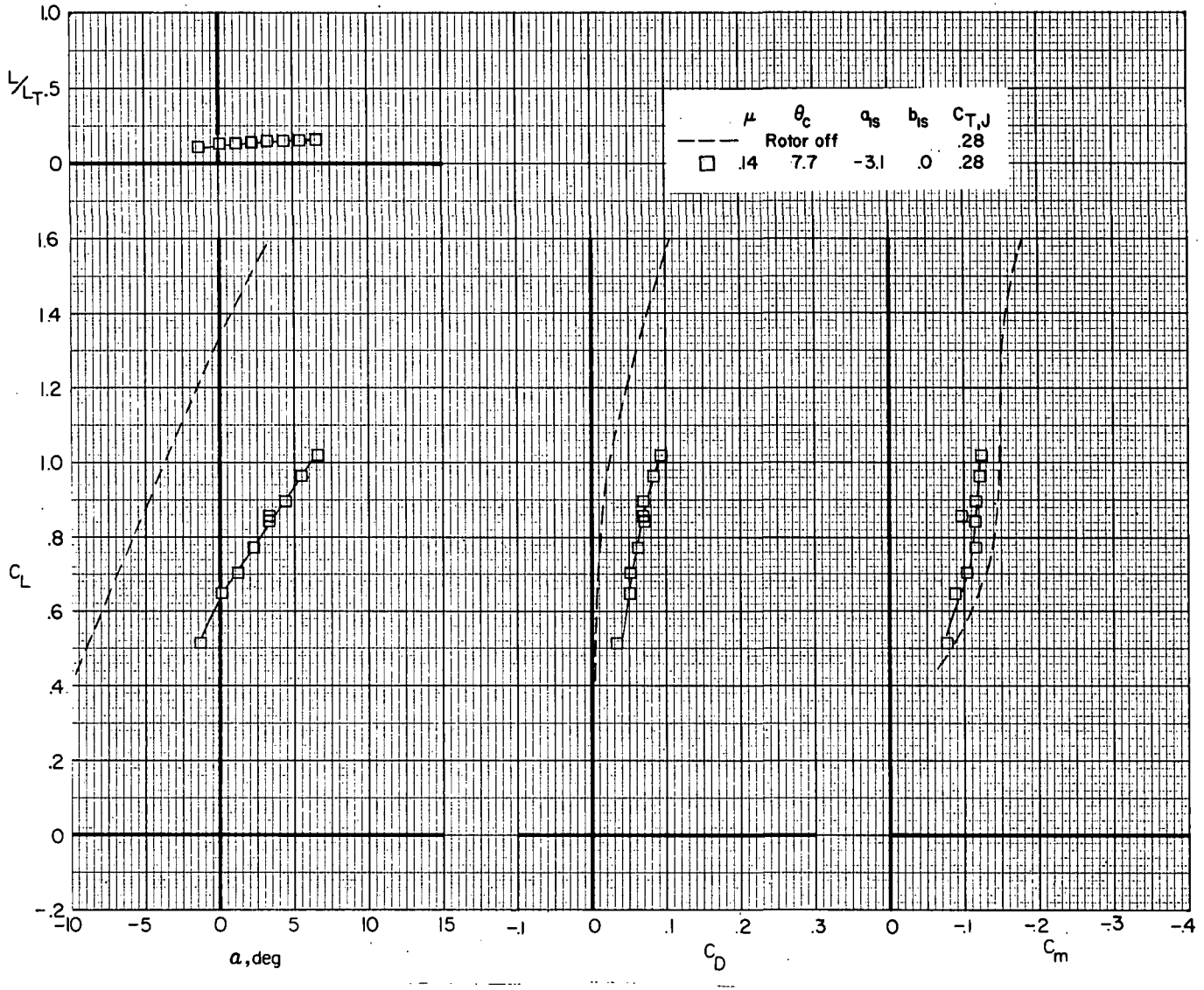

(a) Concluded.

Figure 16.- Continued.

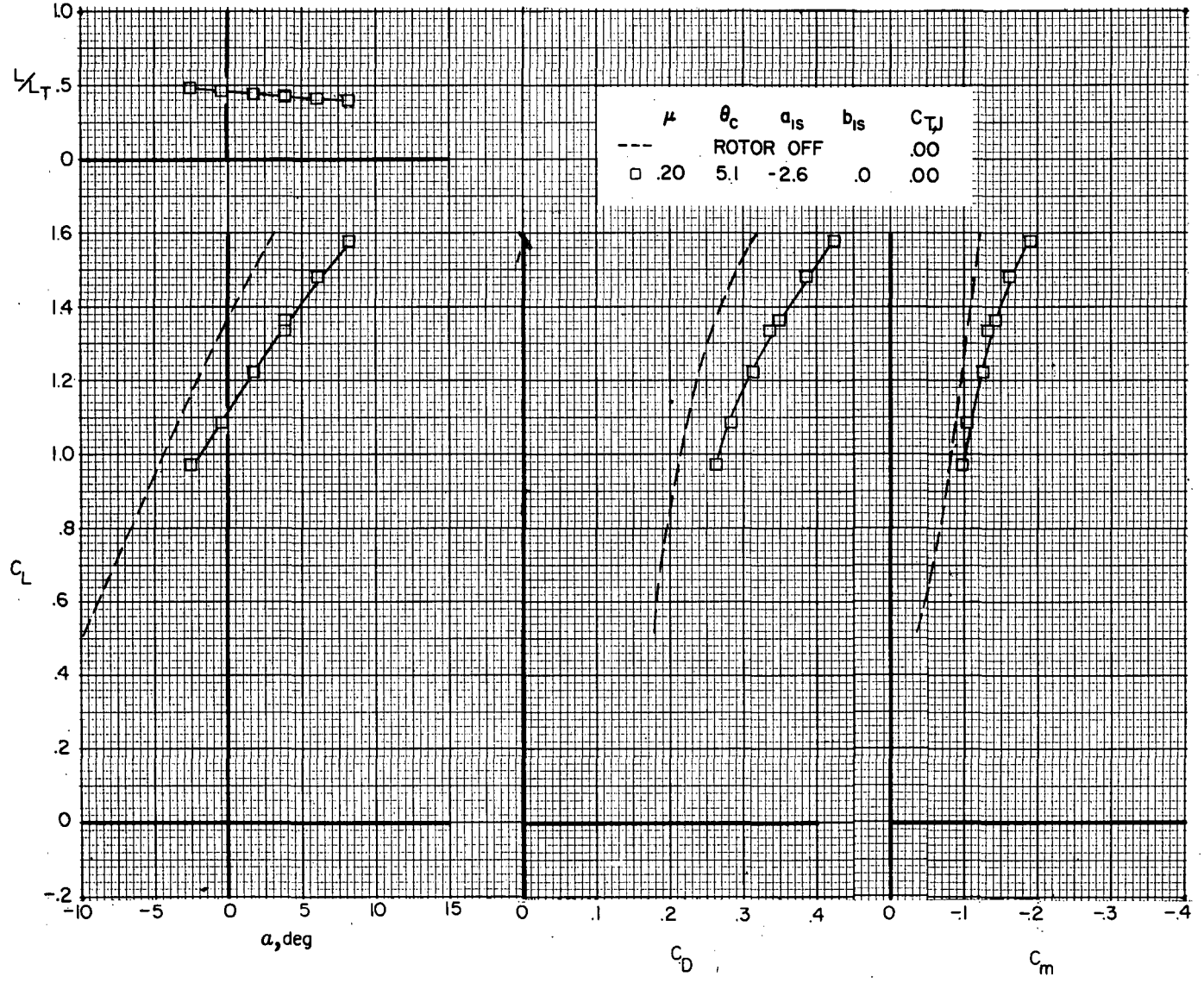

(b) μ = 0.20.

Figure 16.- Continued.

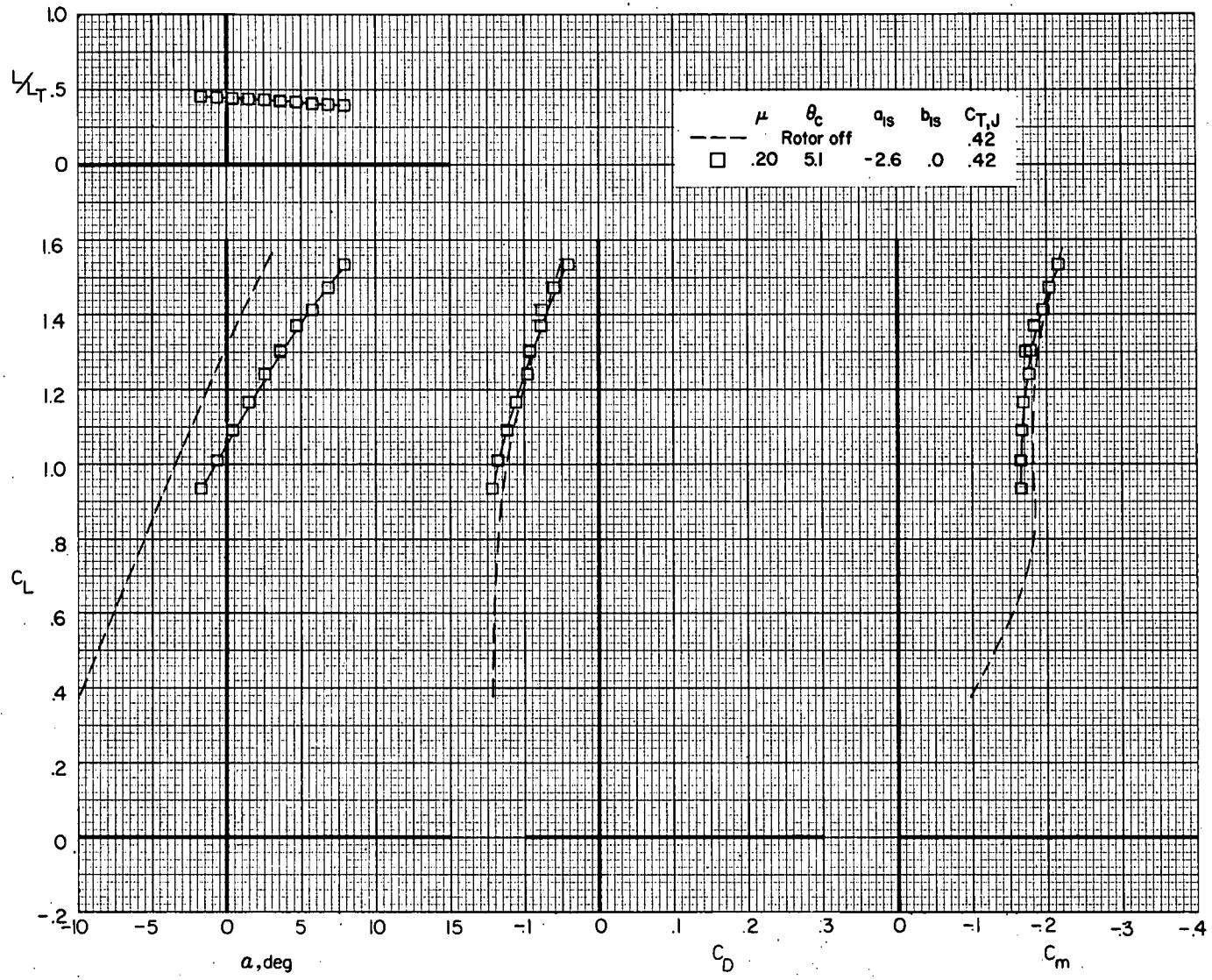

(b) Continued.

Figure 16.- Continued.

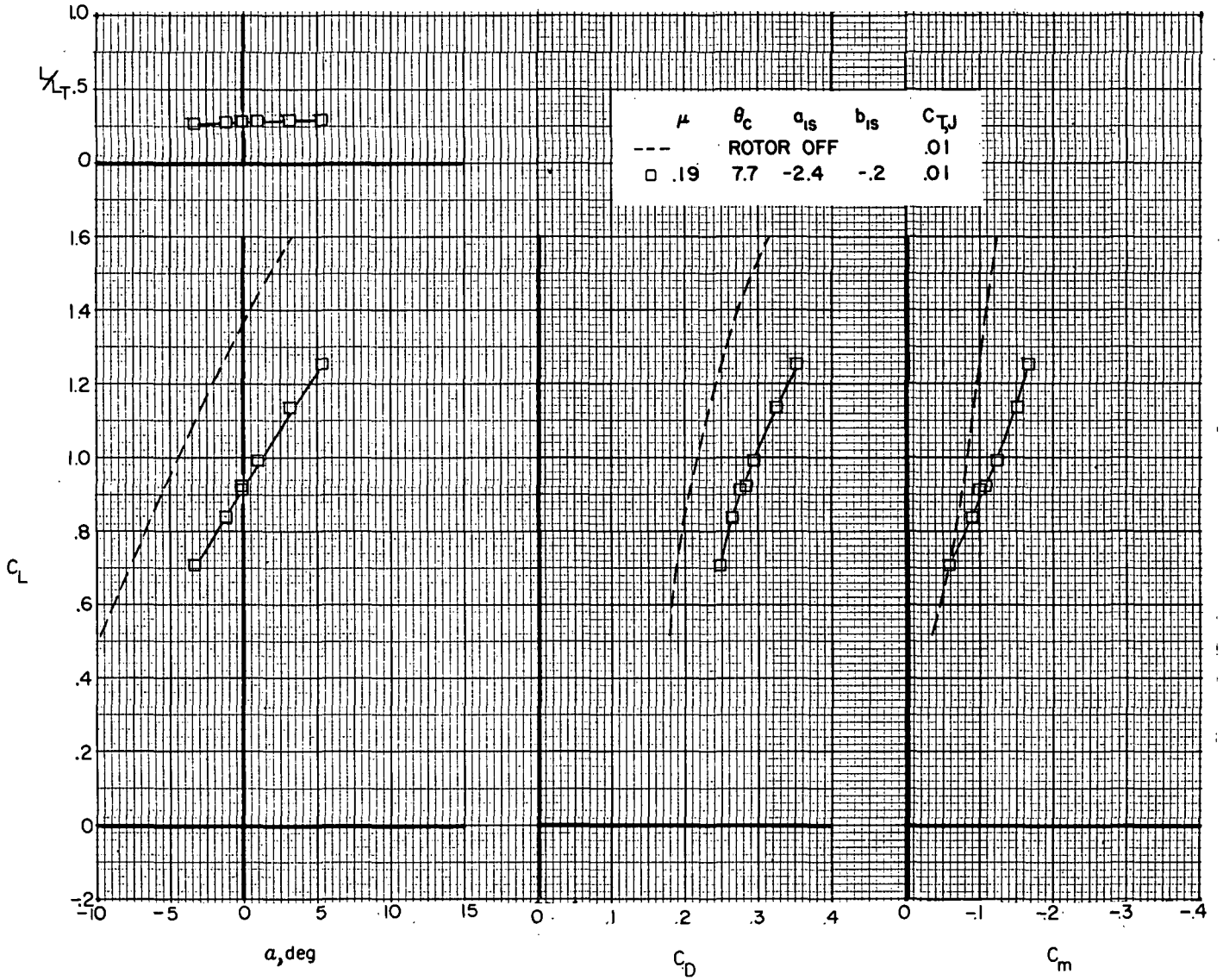

(b) Continued.

Figure 16.- Continued.

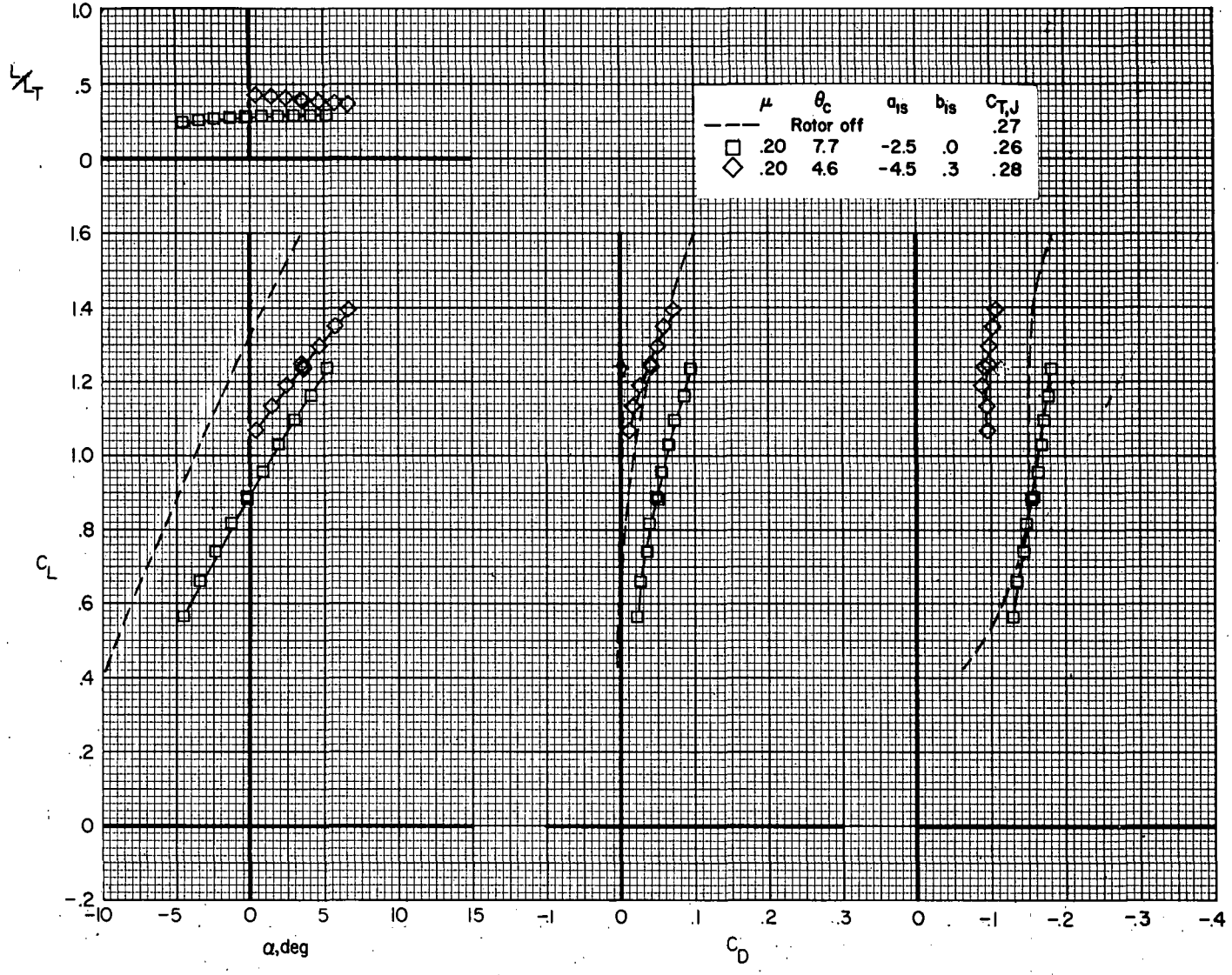

(b) Concluded.

Figure 16.- Continued.

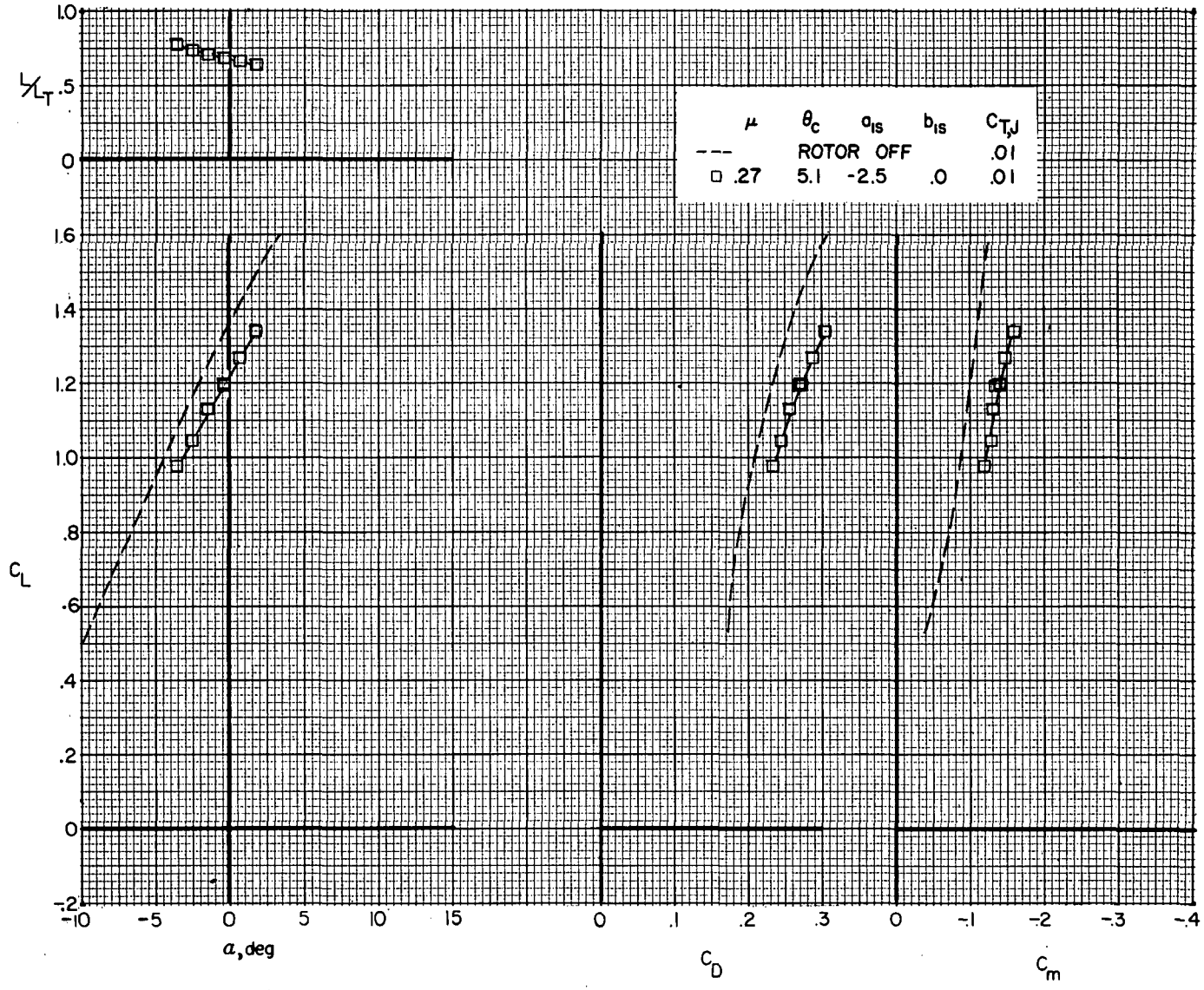

(c) μ = 0.27.

Figure 16.- Continued.

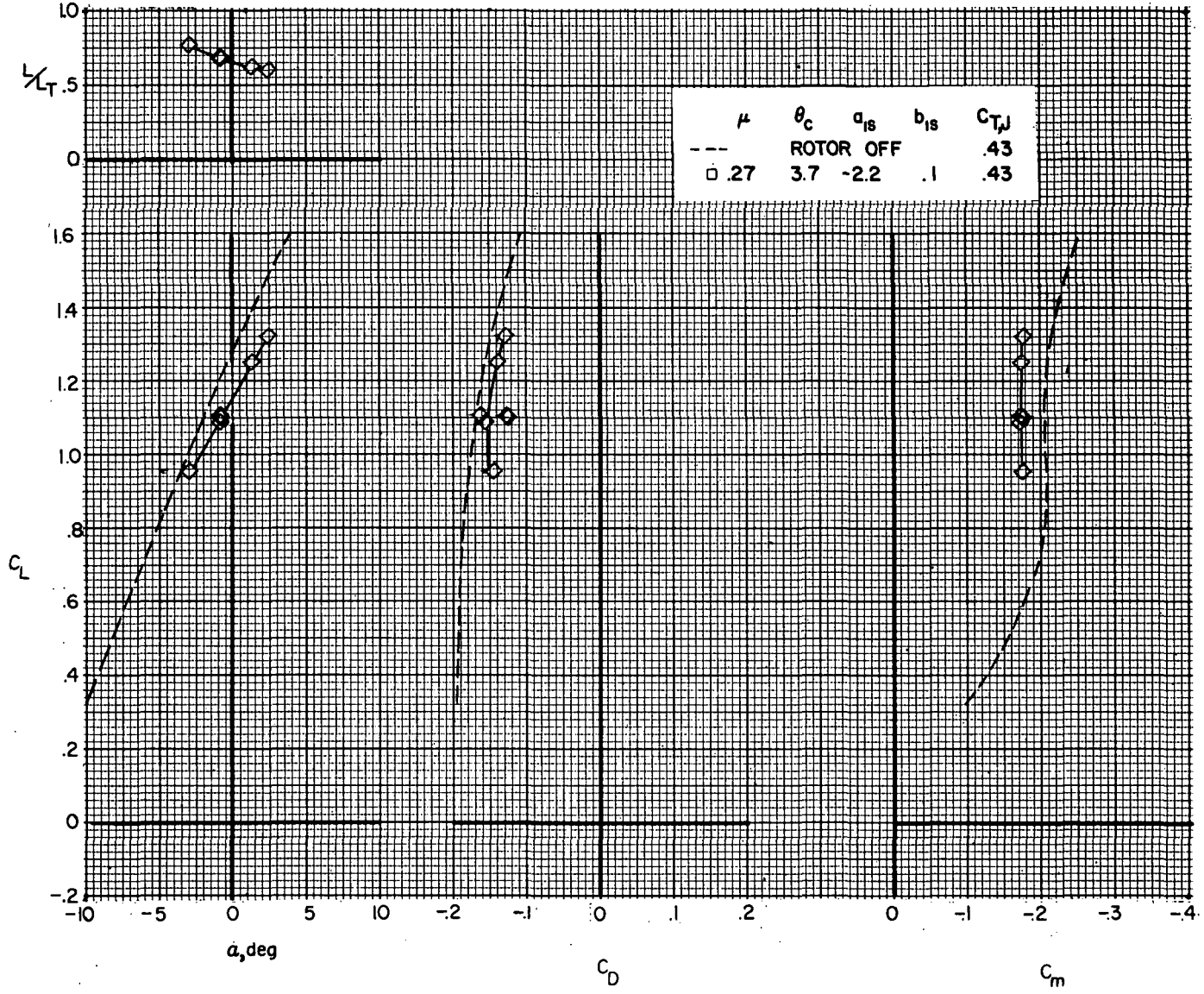

(c) Continued.

Figure 16.- Continued.

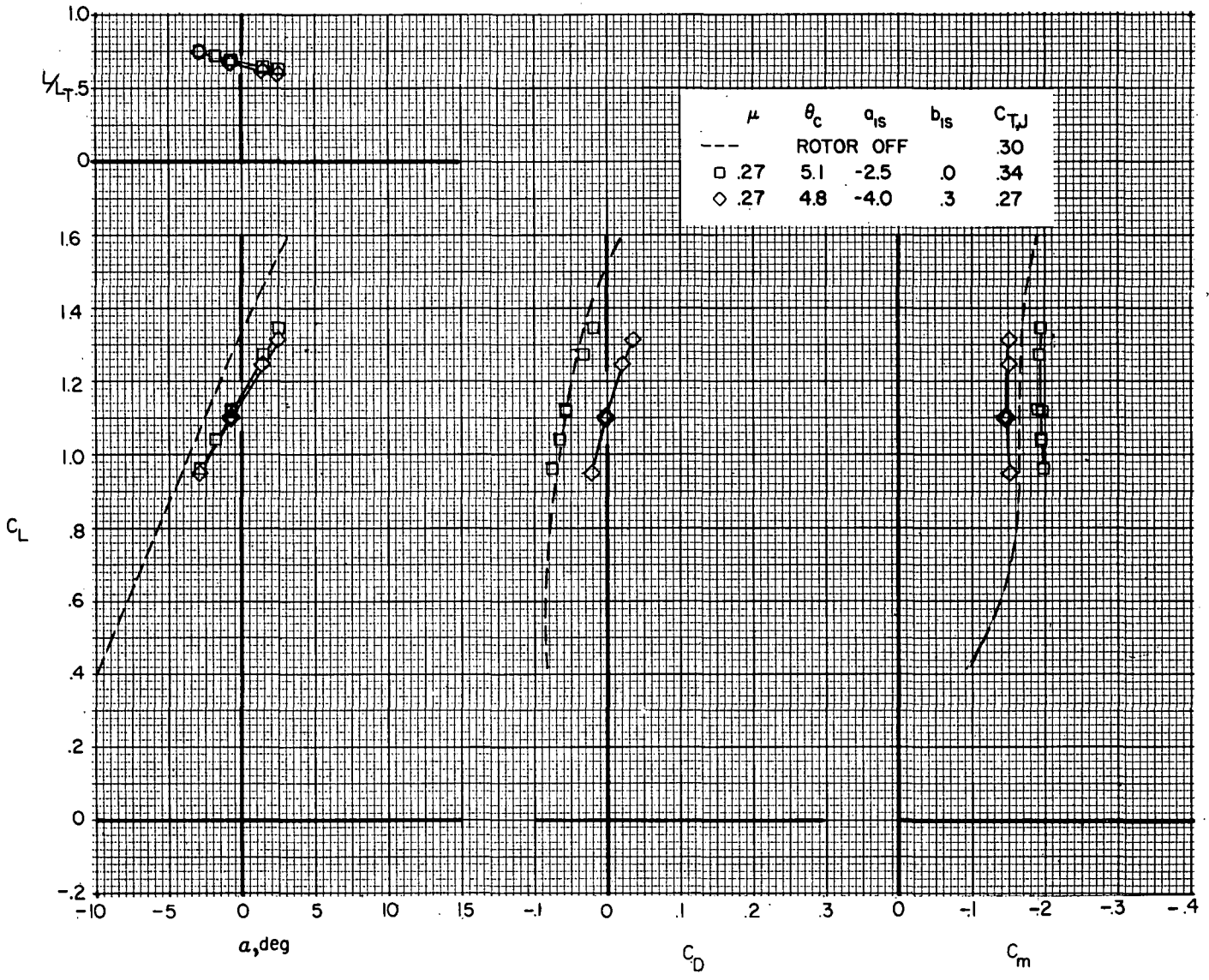

(c) Continued.

Figure 16.- Continued.

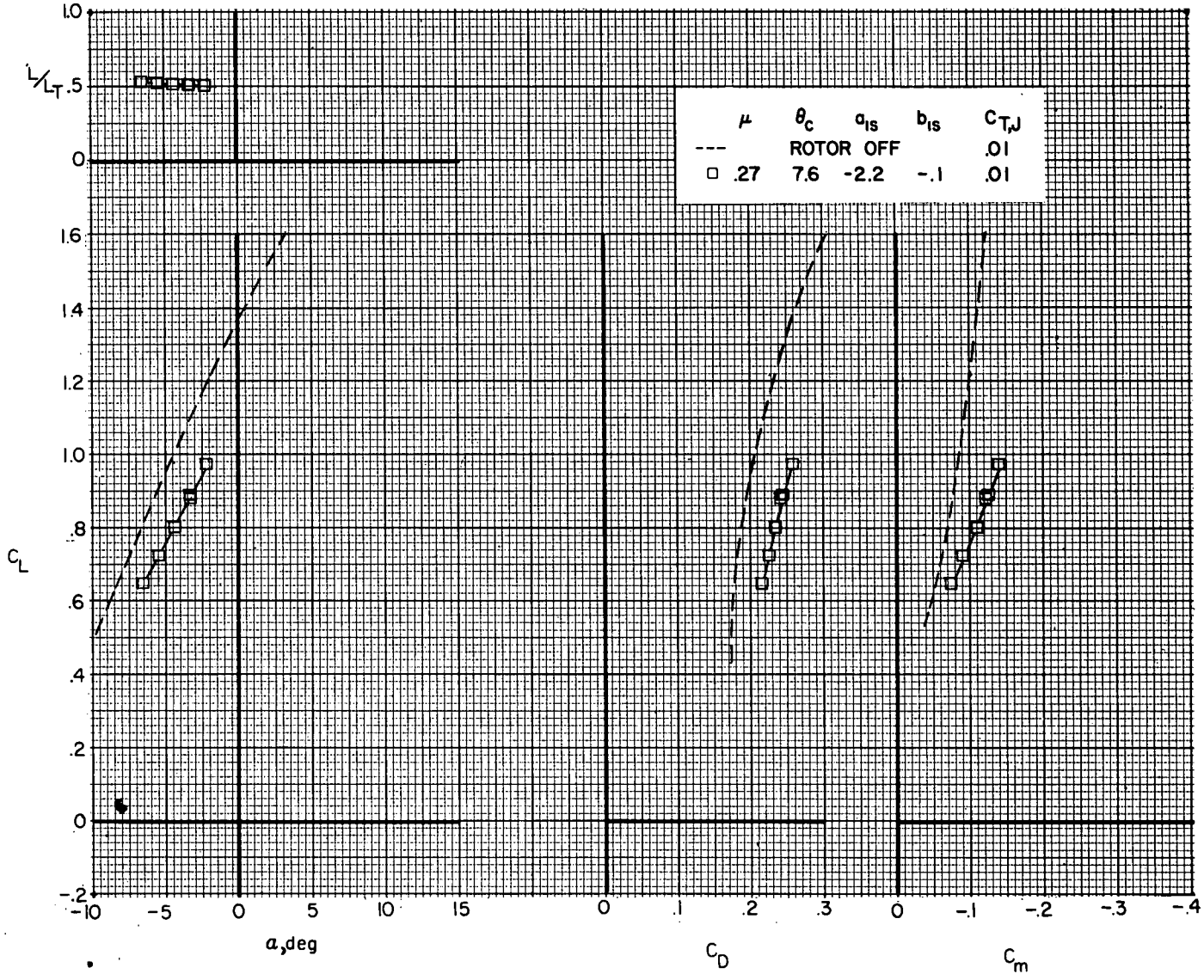

(c) Continued.

Figure 16.- Continued.

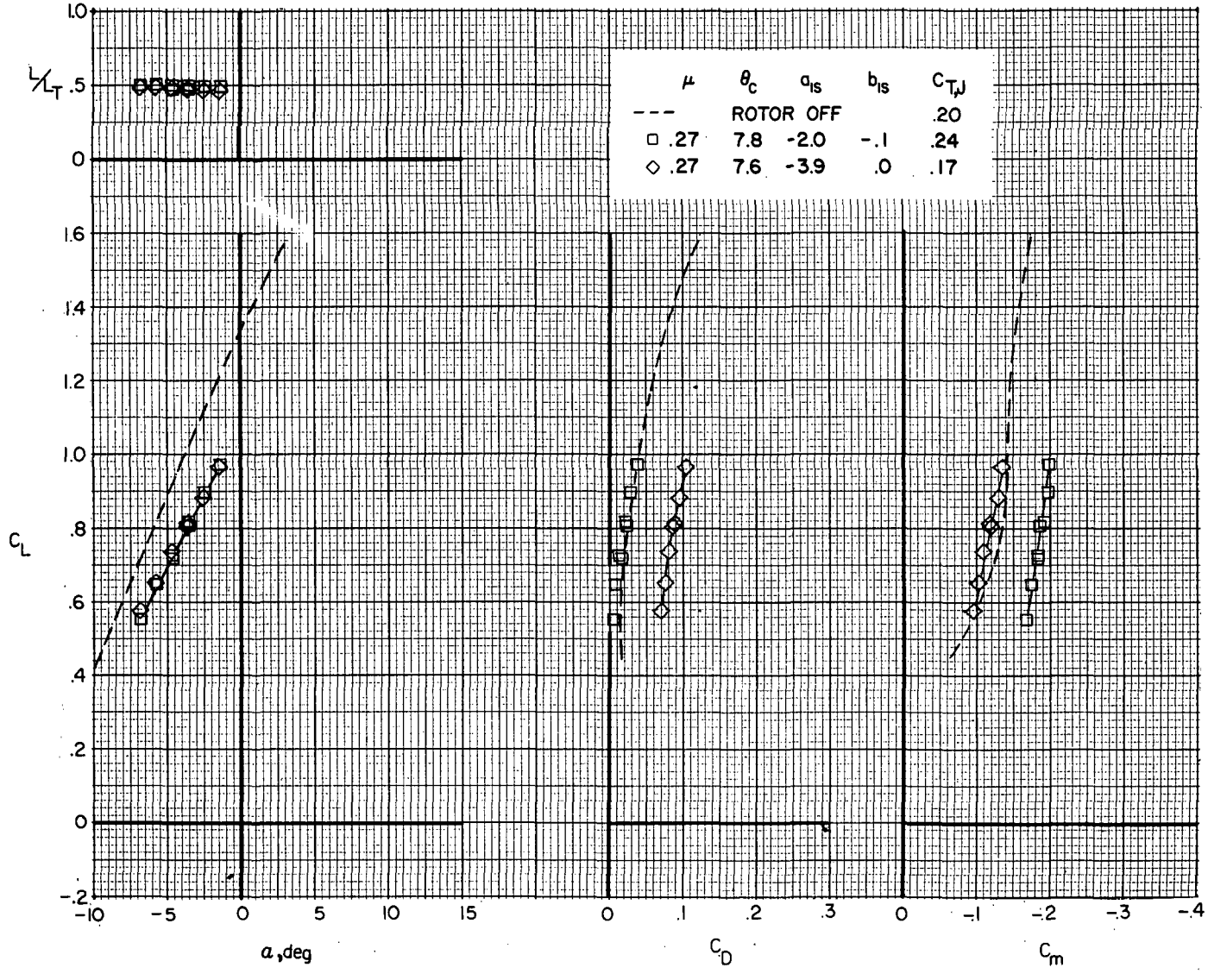

(c) Concluded.

Figure 16.- Continued.

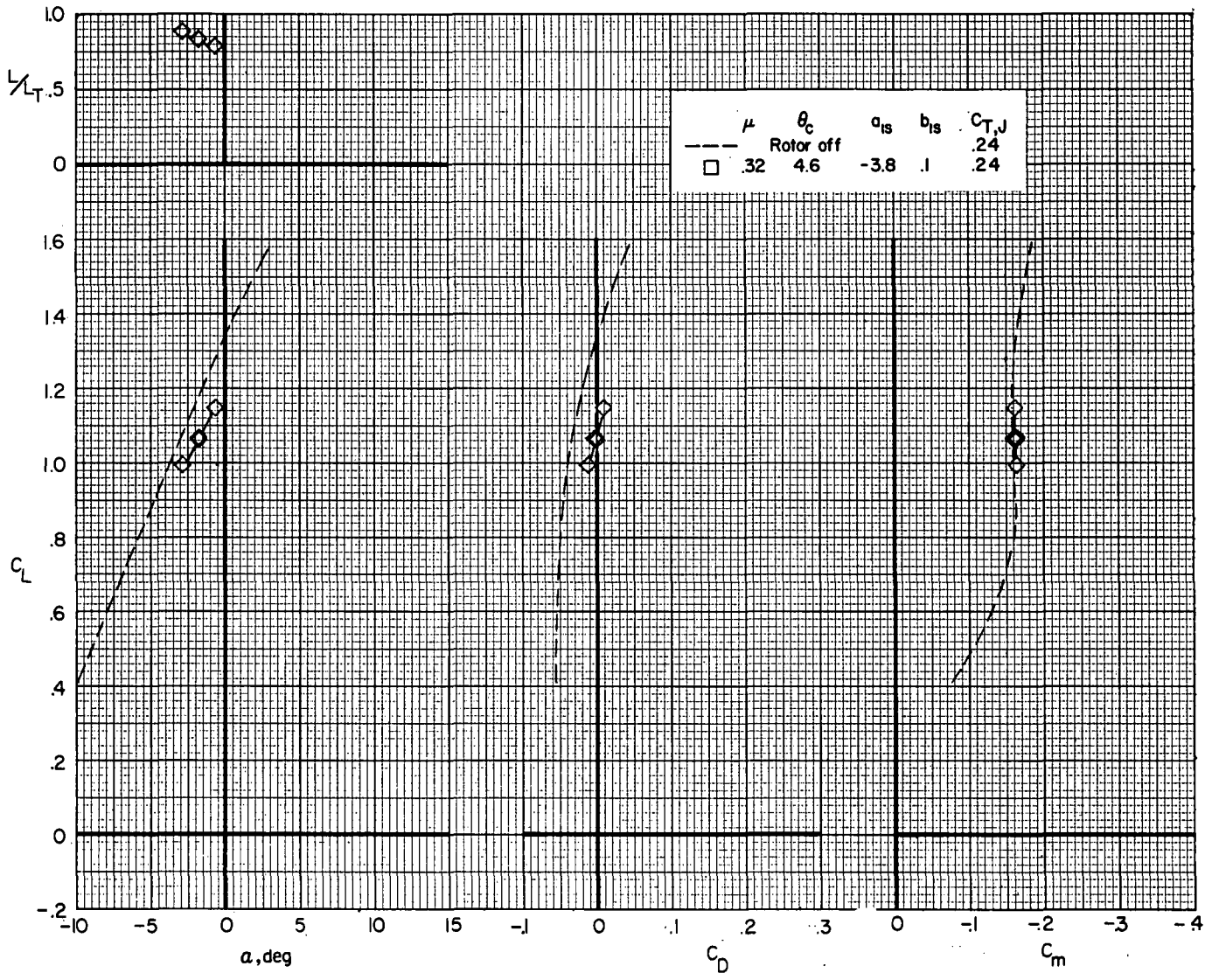

(d) μ = 0.32.

Figure 16.- Continued.

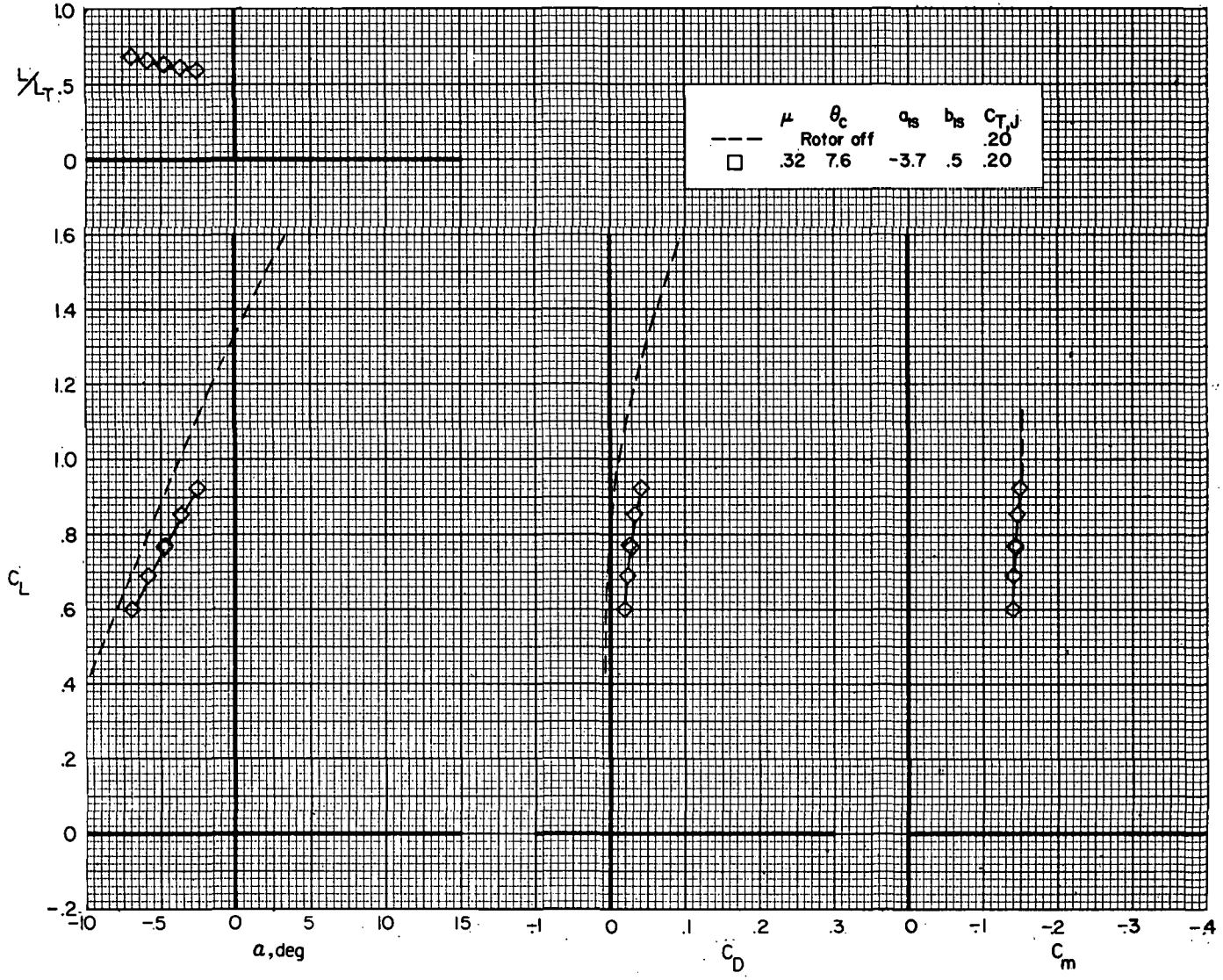

(d) Concluded.

Figure 16.- Concluded.

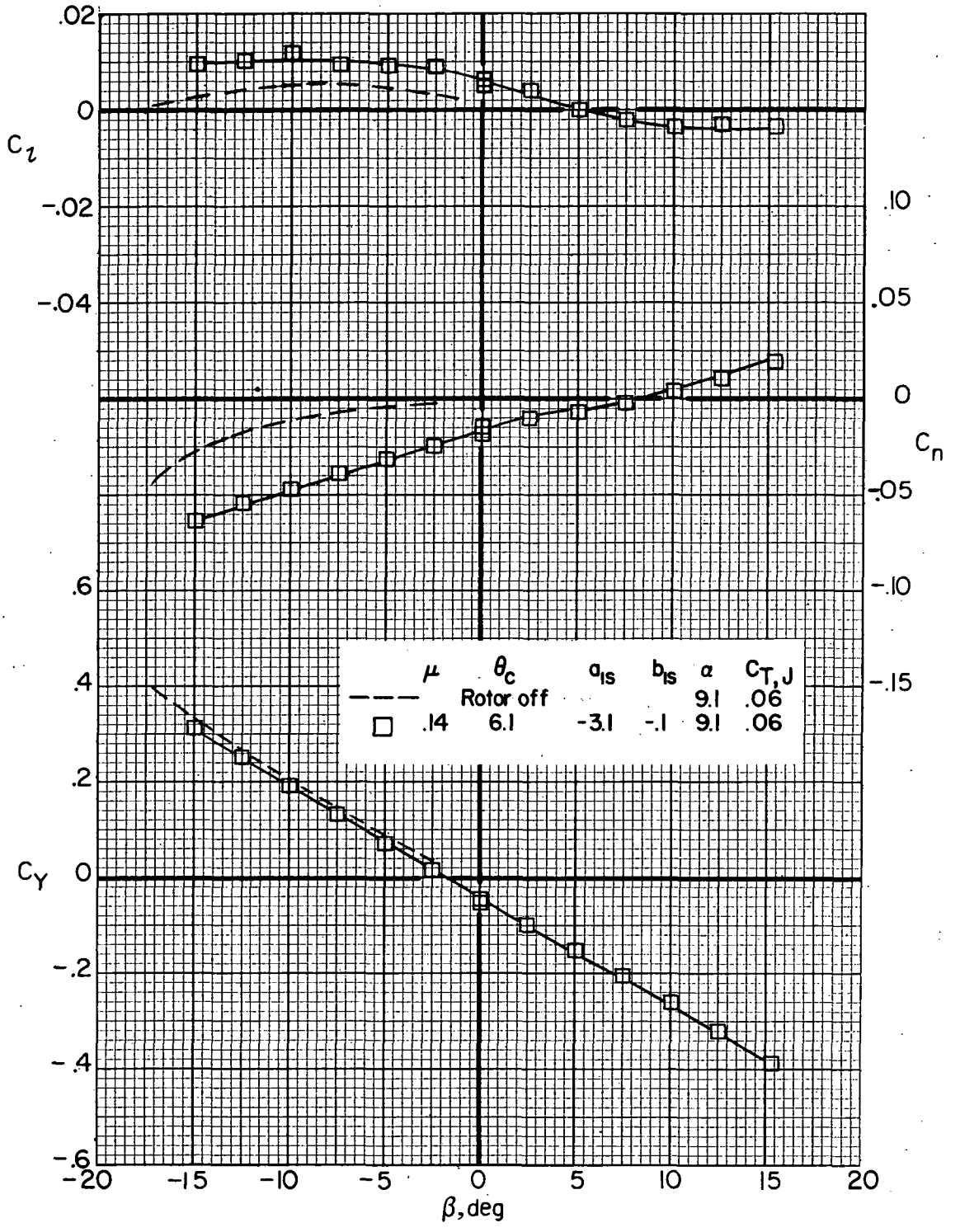

(a) $\mu = 0.14$.

Figure 17.- Comparison of airframe lateral aerodynamic characteristics for compound helicopter (rotor forces and moments removed) for rotor on and rotor off. $i_w = 0^o$; $\delta_f = 0^o$; $i_t = 3^o$. (θ_c, a_{ls}, b_{ls}, and α are in degrees.)

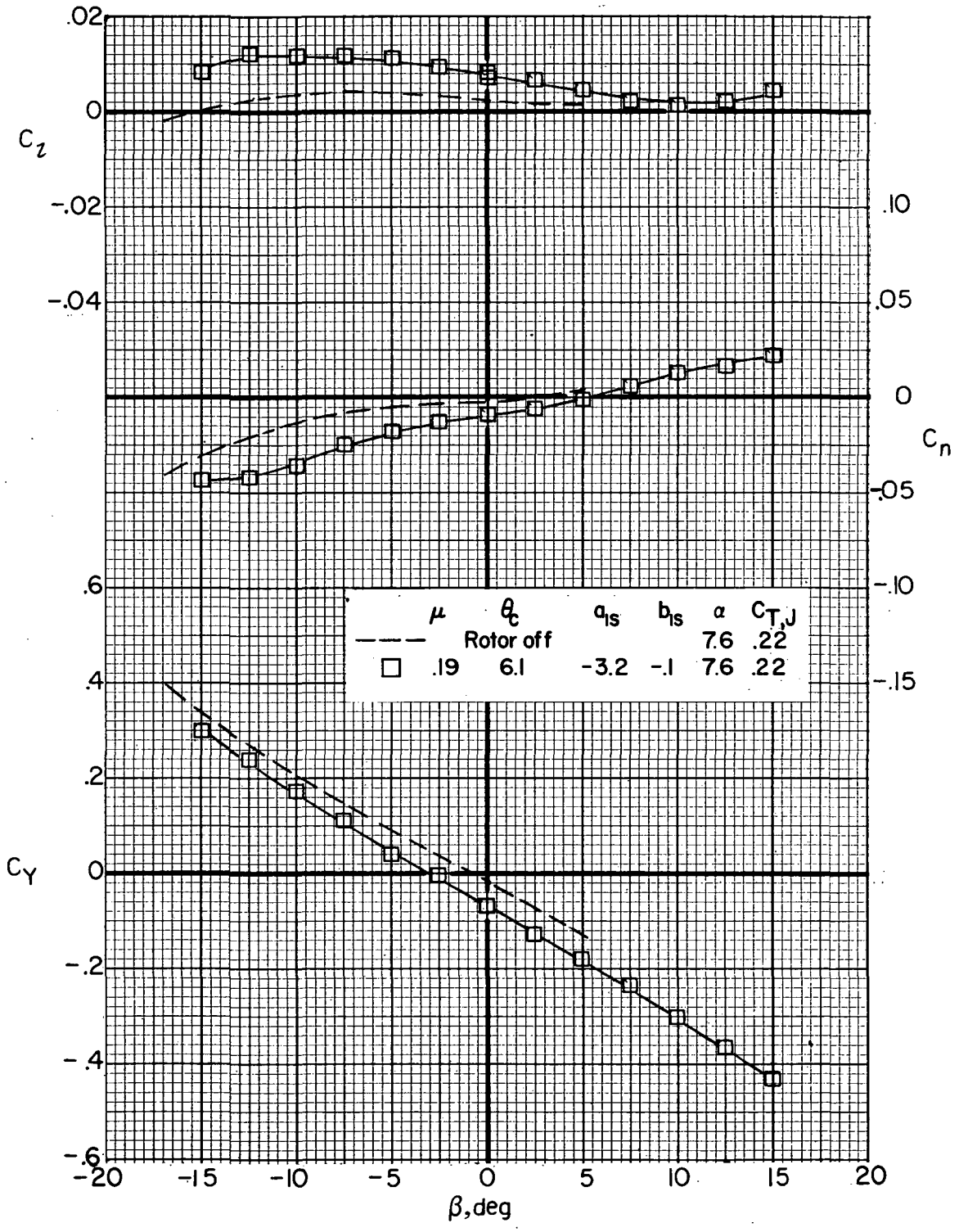

(b) μ = 0.19.

Figure 17.- Continued.

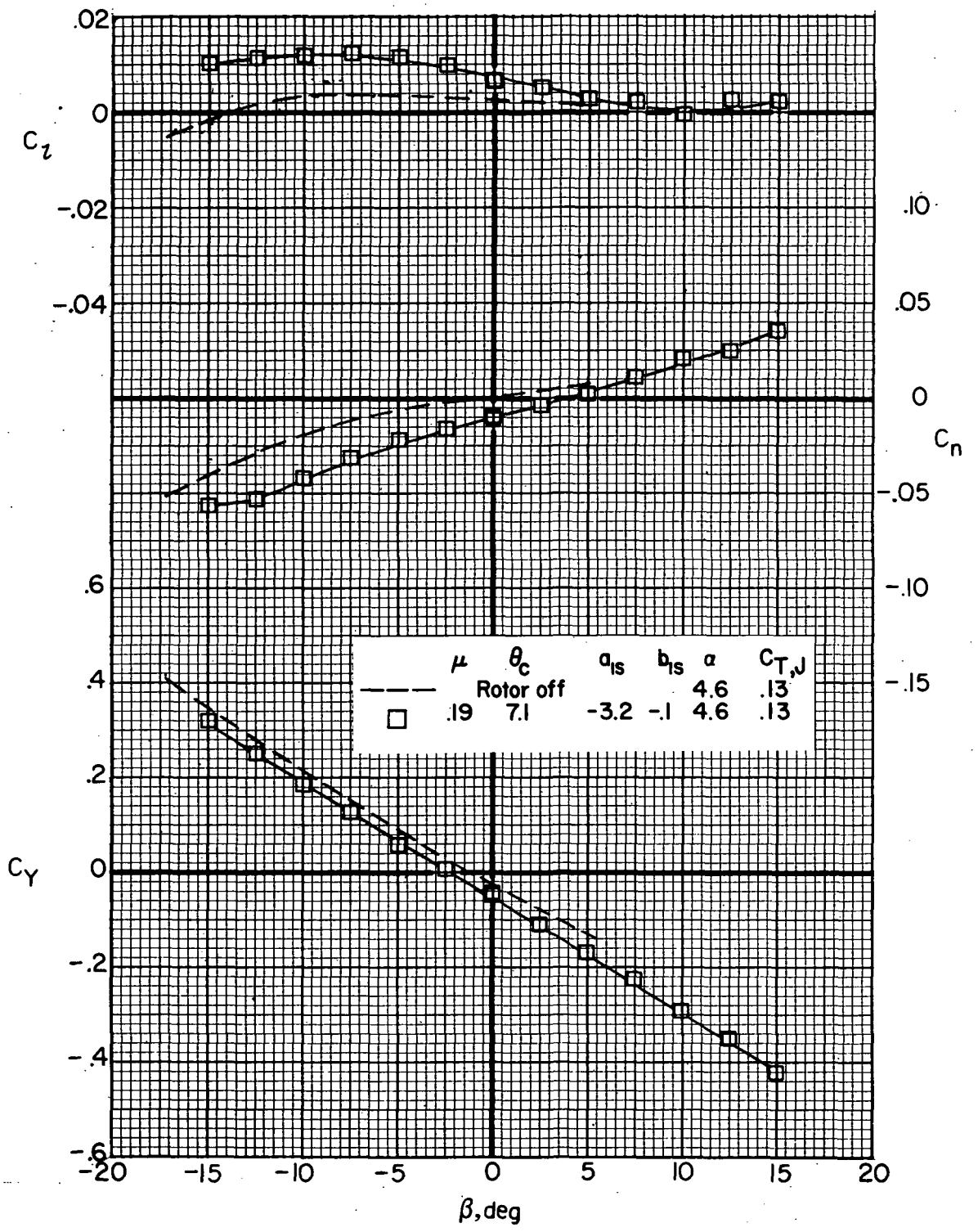

(b) Concluded.

Figure 17.- Continued.

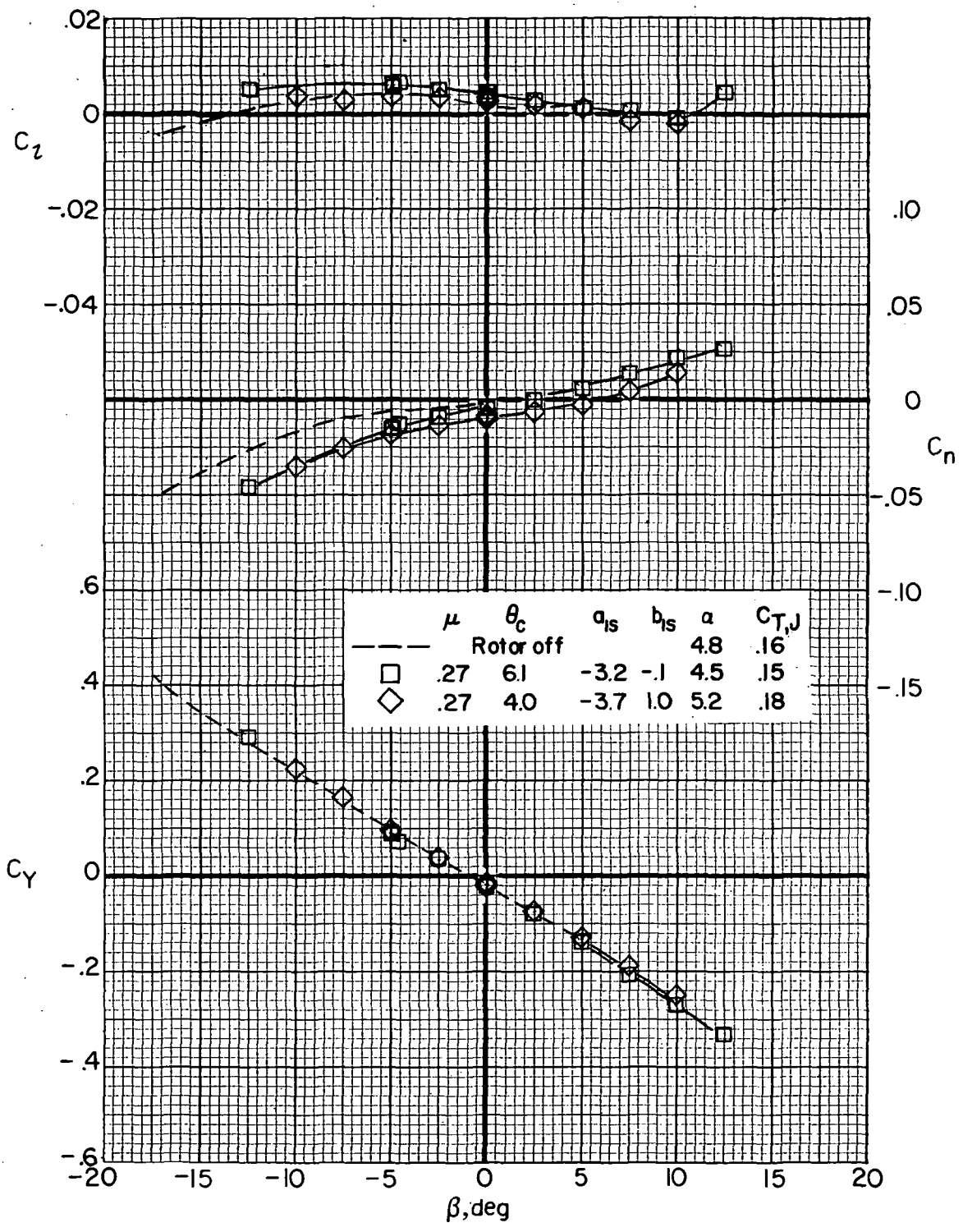

(c) μ = 0.27.

Figure 17.- Continued.

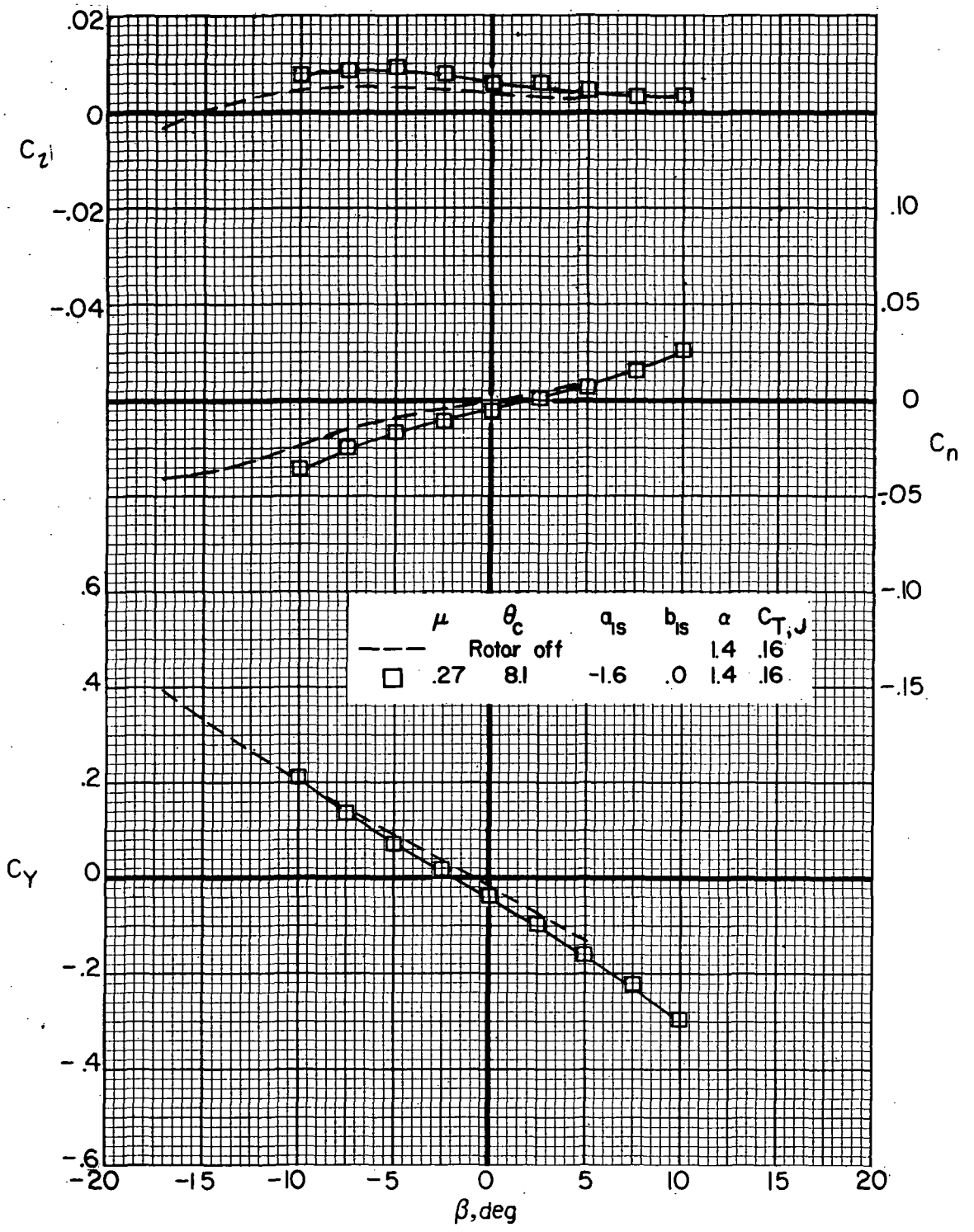

(c) Concluded.

Figure 17.- Continued.

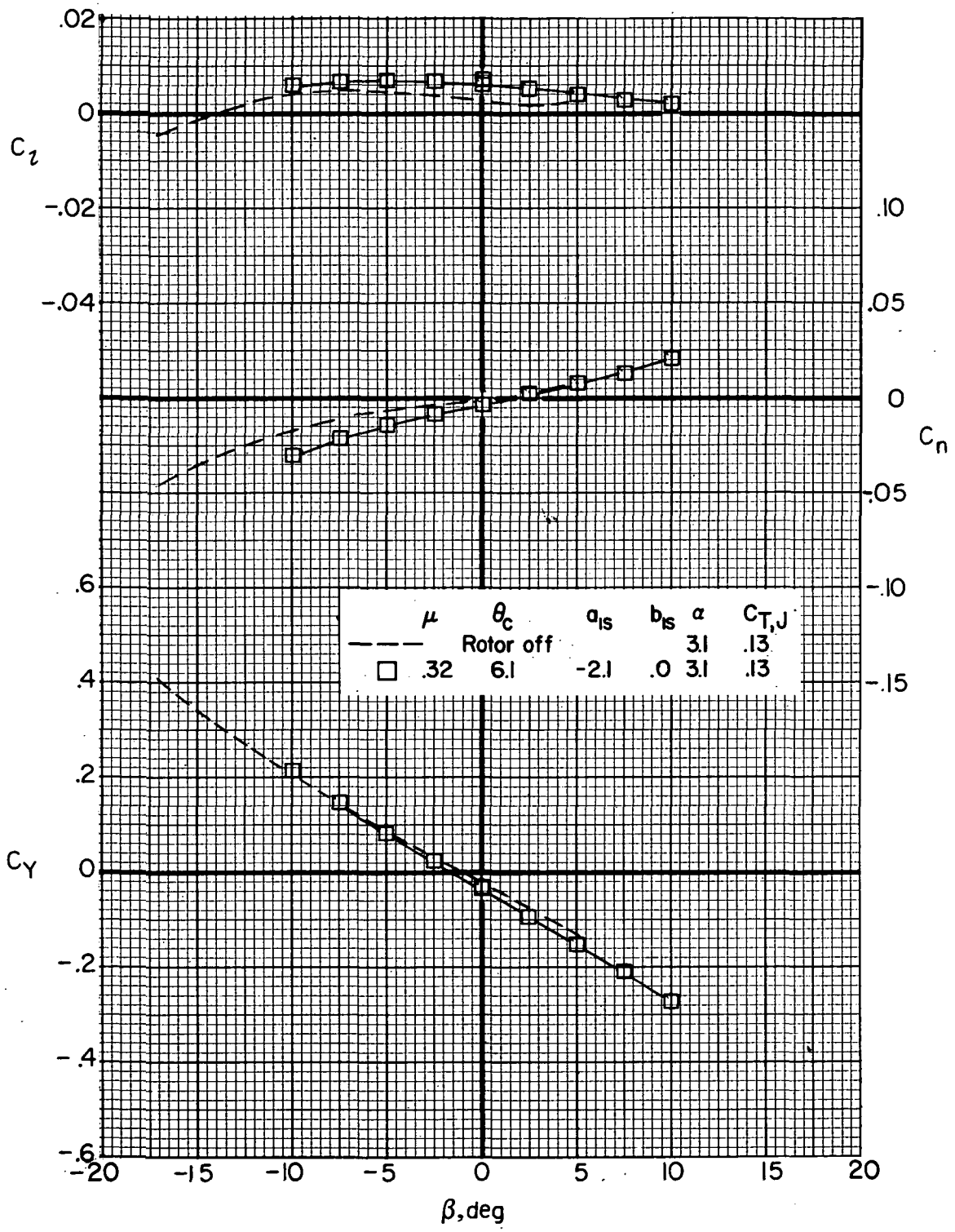

(d) $\mu = 0.32$.

Figure 17.- Continued.

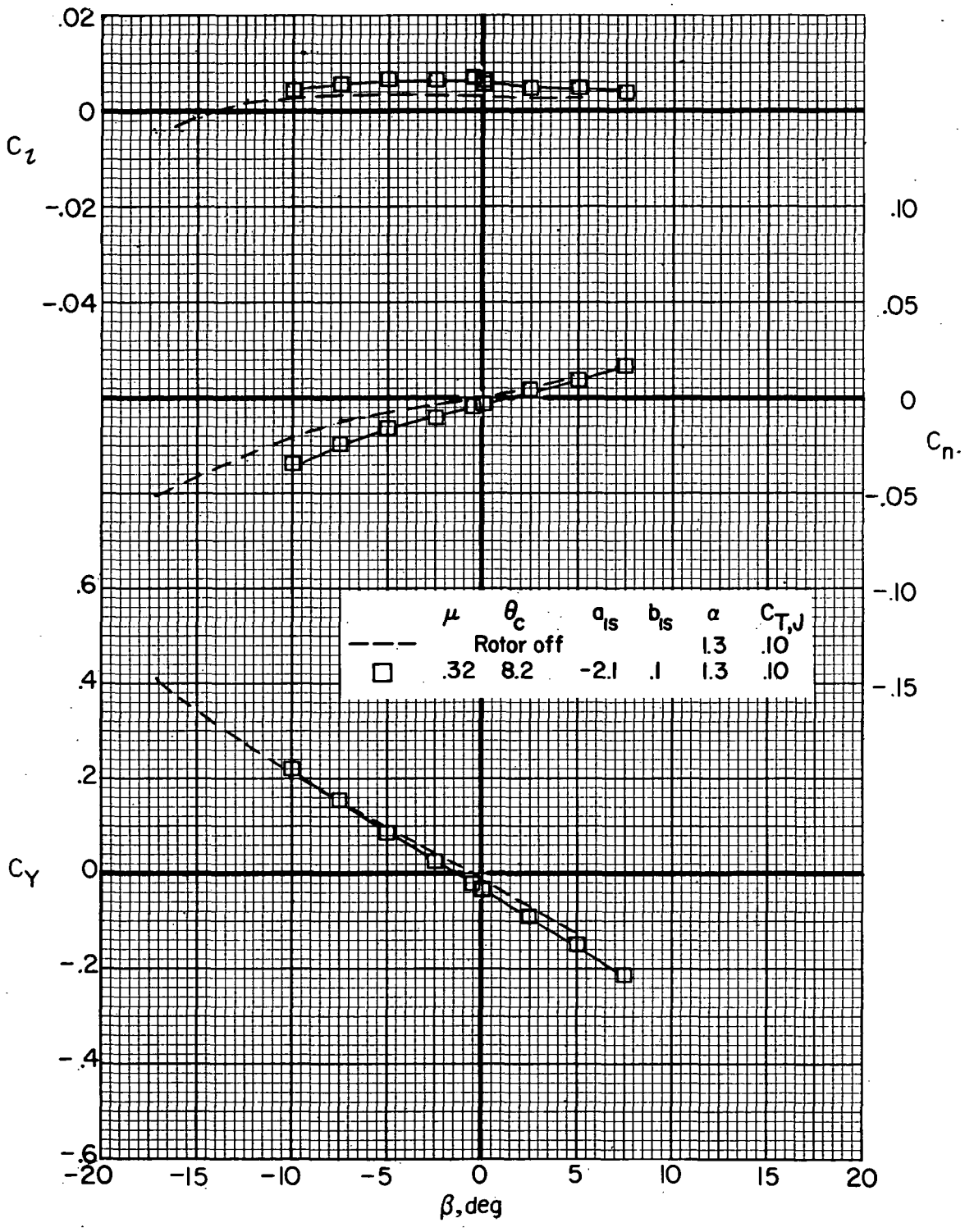

(d) Concluded.

Figure 17.- Concluded.

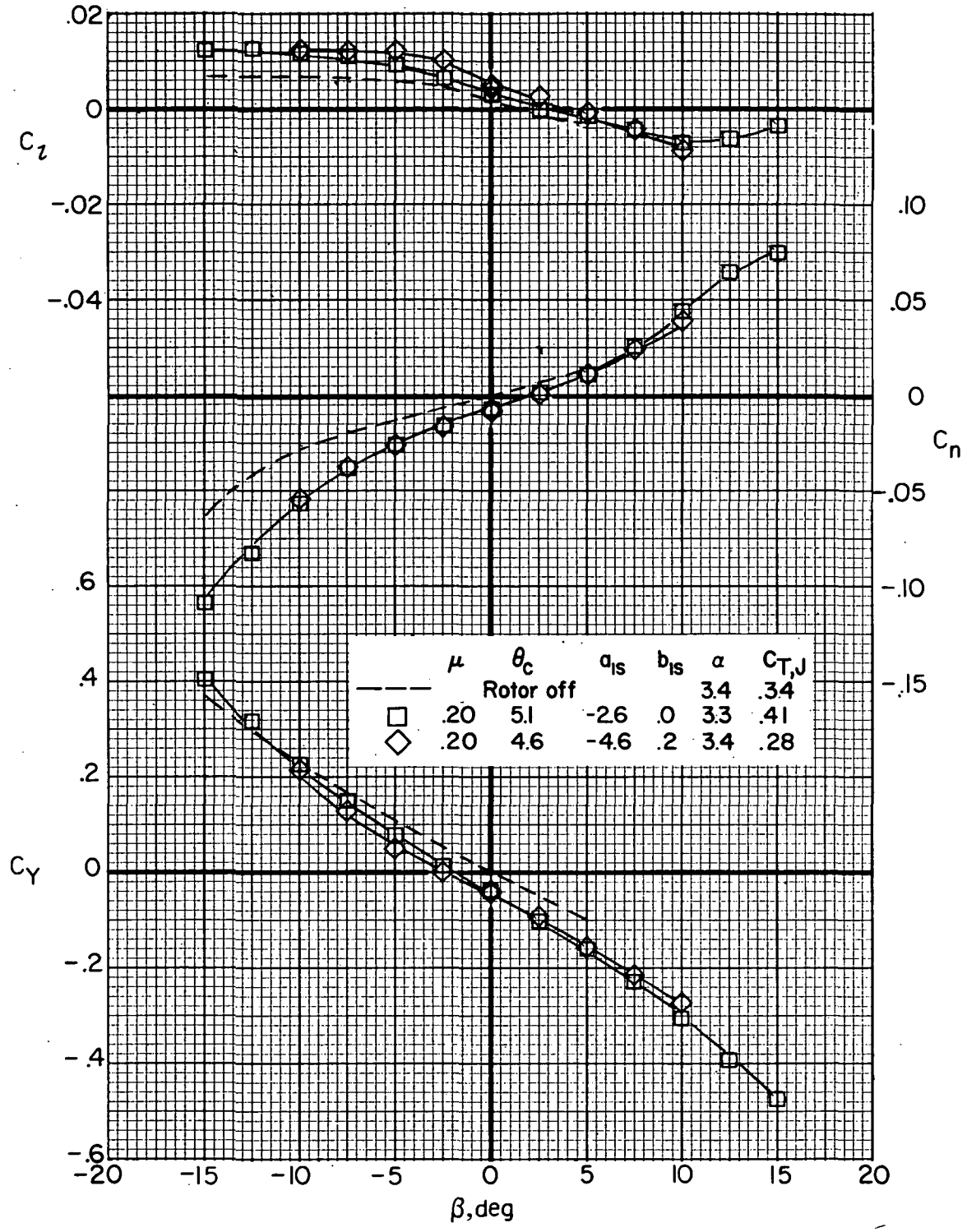

(a) $\mu = 0.20$.

Figure 18.- Comparison of airframe lateral aerodynamic characteristics for compound helicopter (rotor forces and moments removed) for rotor on and rotor off. $i_w = 7.5^\circ$; $\delta_f = 30^\circ$; $i_t = 3^\circ$. (θ_c, a_{ls}, b_{ls}, and α are in degrees.)

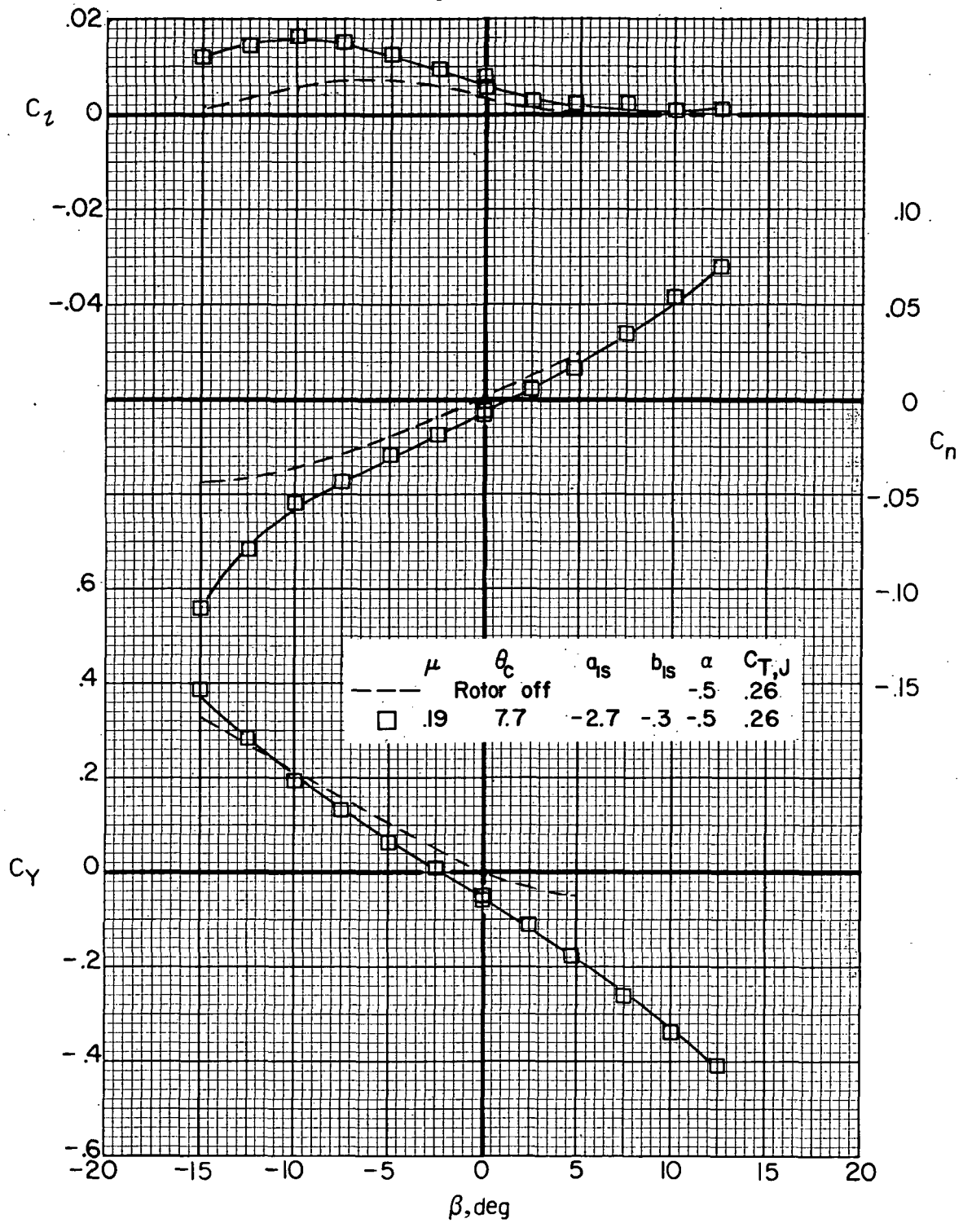

(a) Concluded.

Figure 18.- Continued.

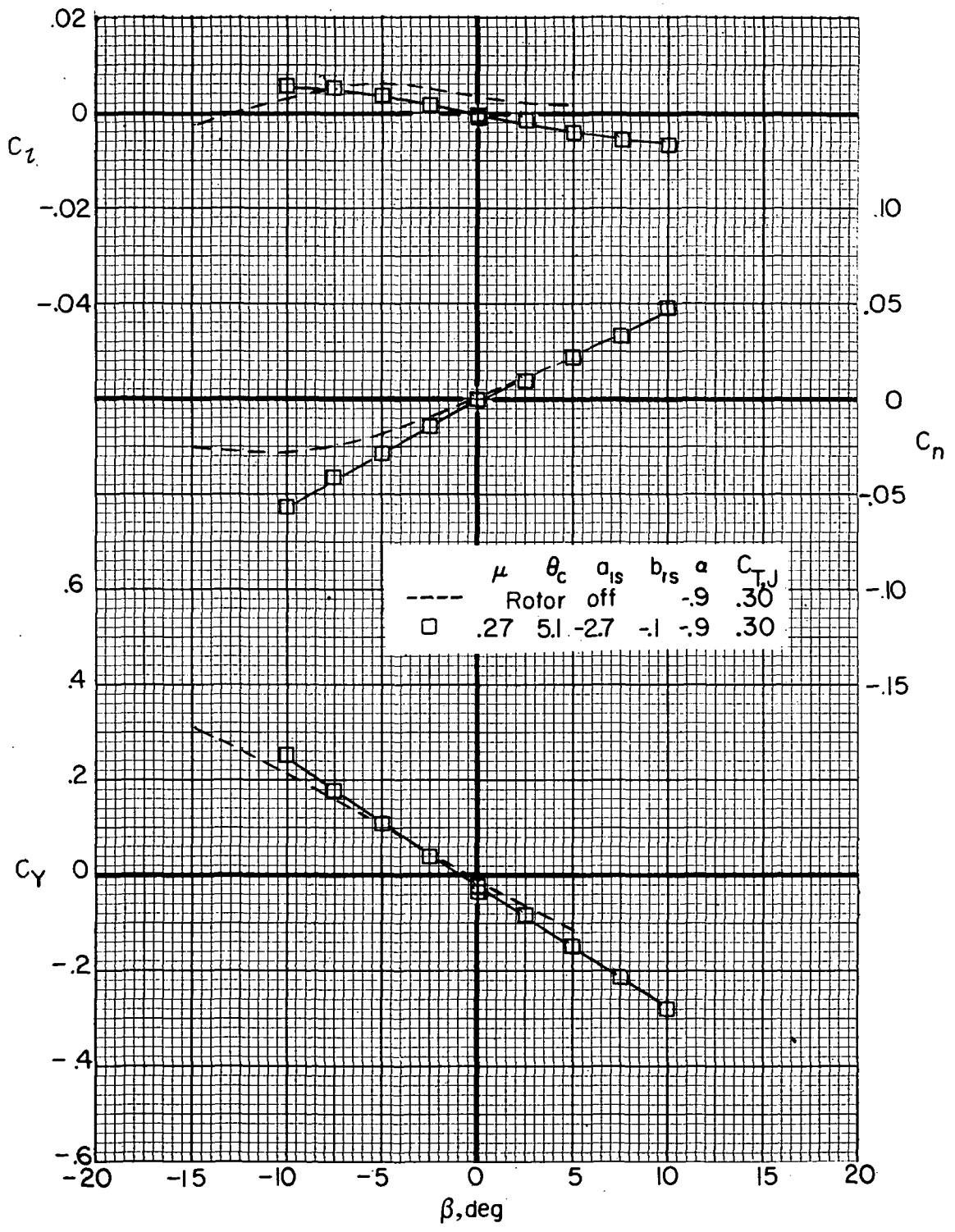

(b) μ = 0.27.

Figure 18.- Continued.

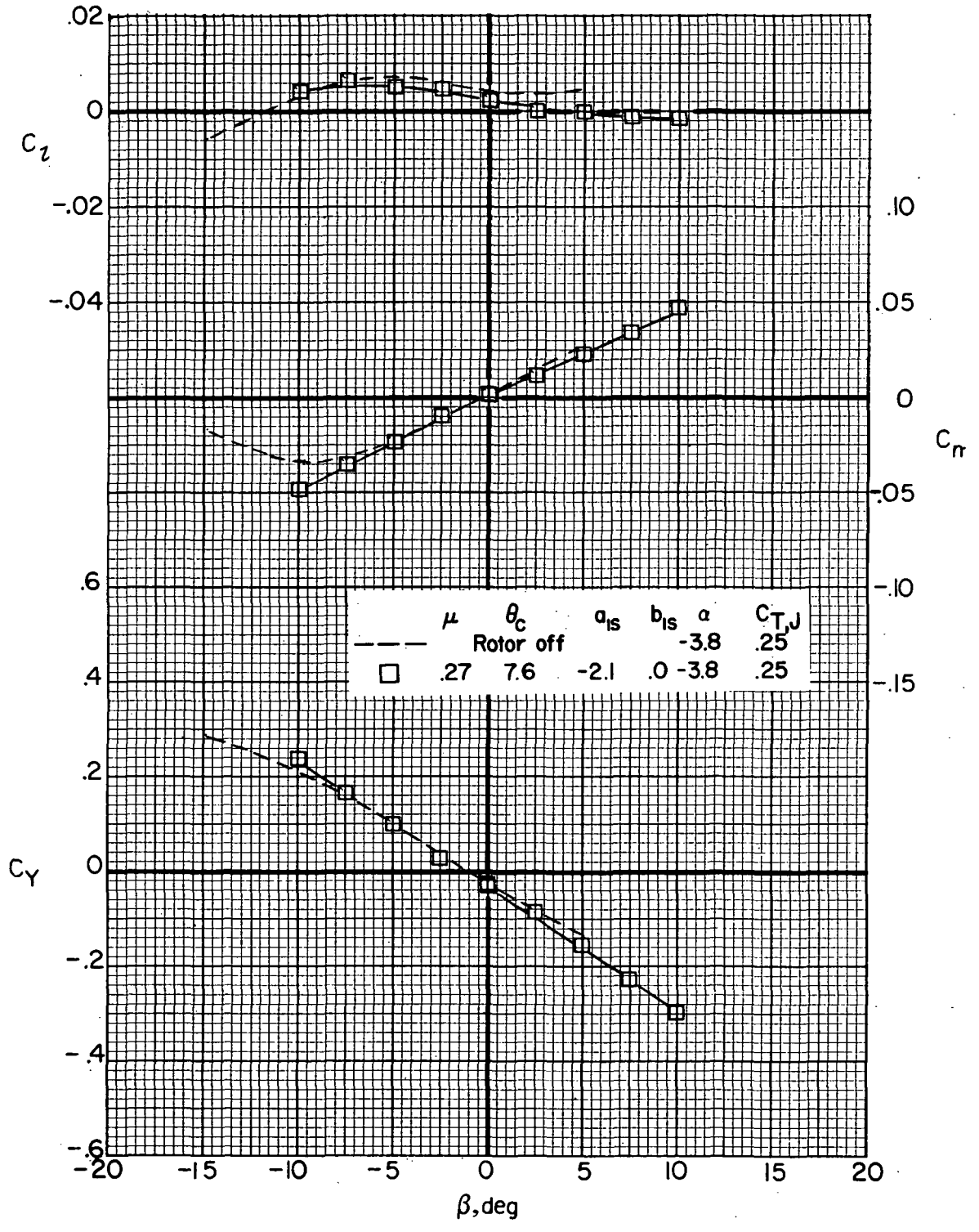

(b) Concluded.

Figure 18.- Continued.

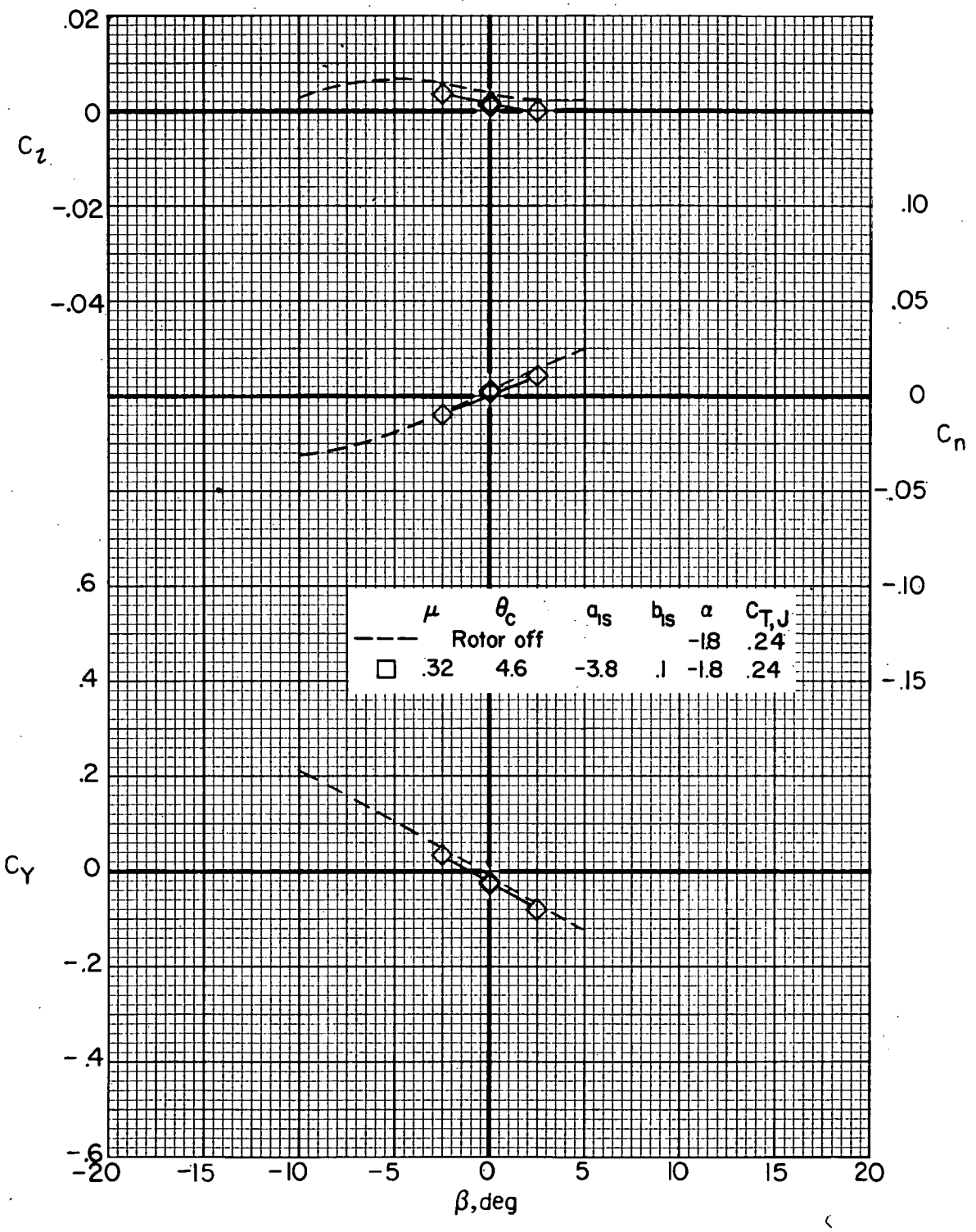

(c) μ = 0.32.

Figure 18.- Continued.

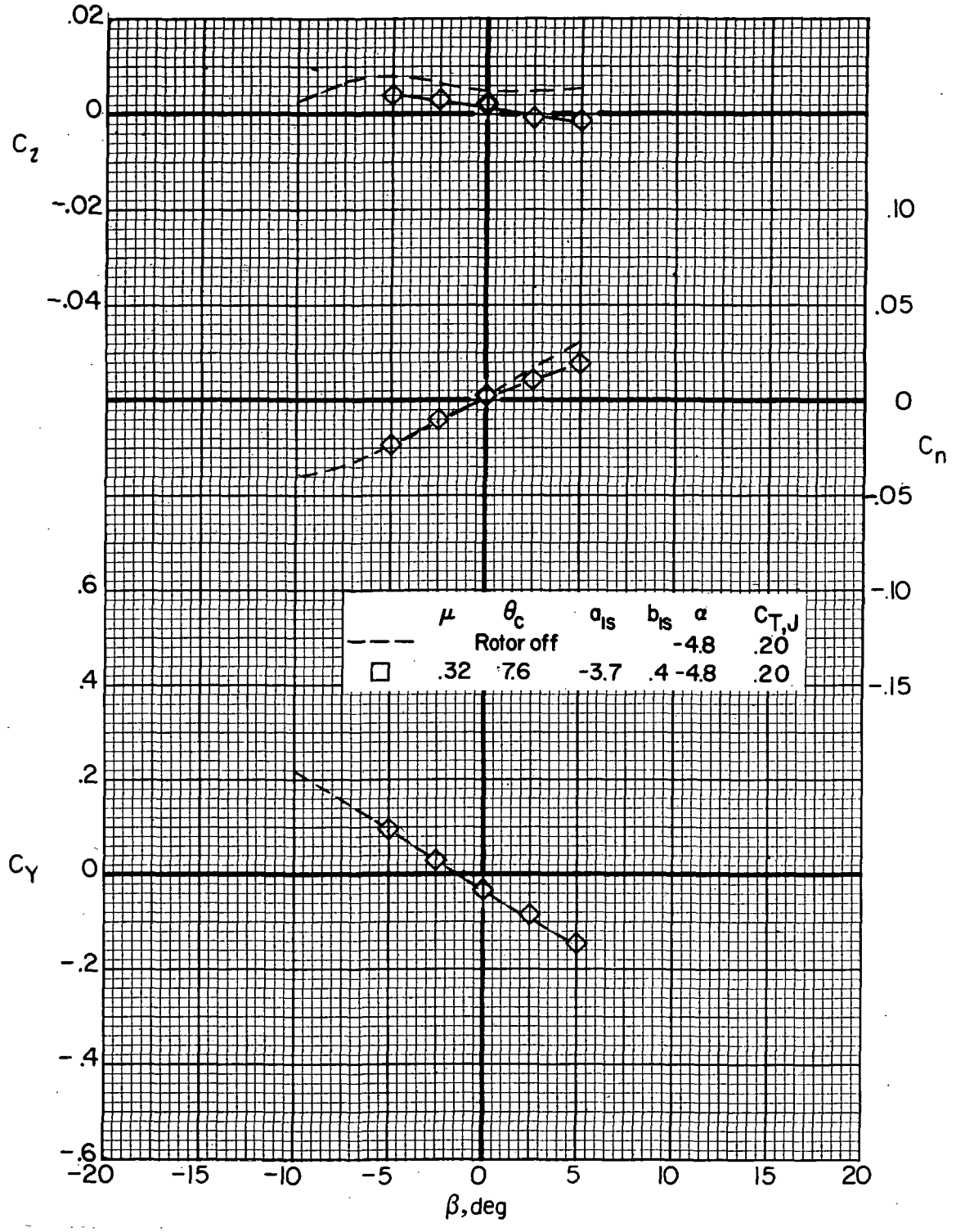

(c) Concluded.

Figure 18.- Concluded.

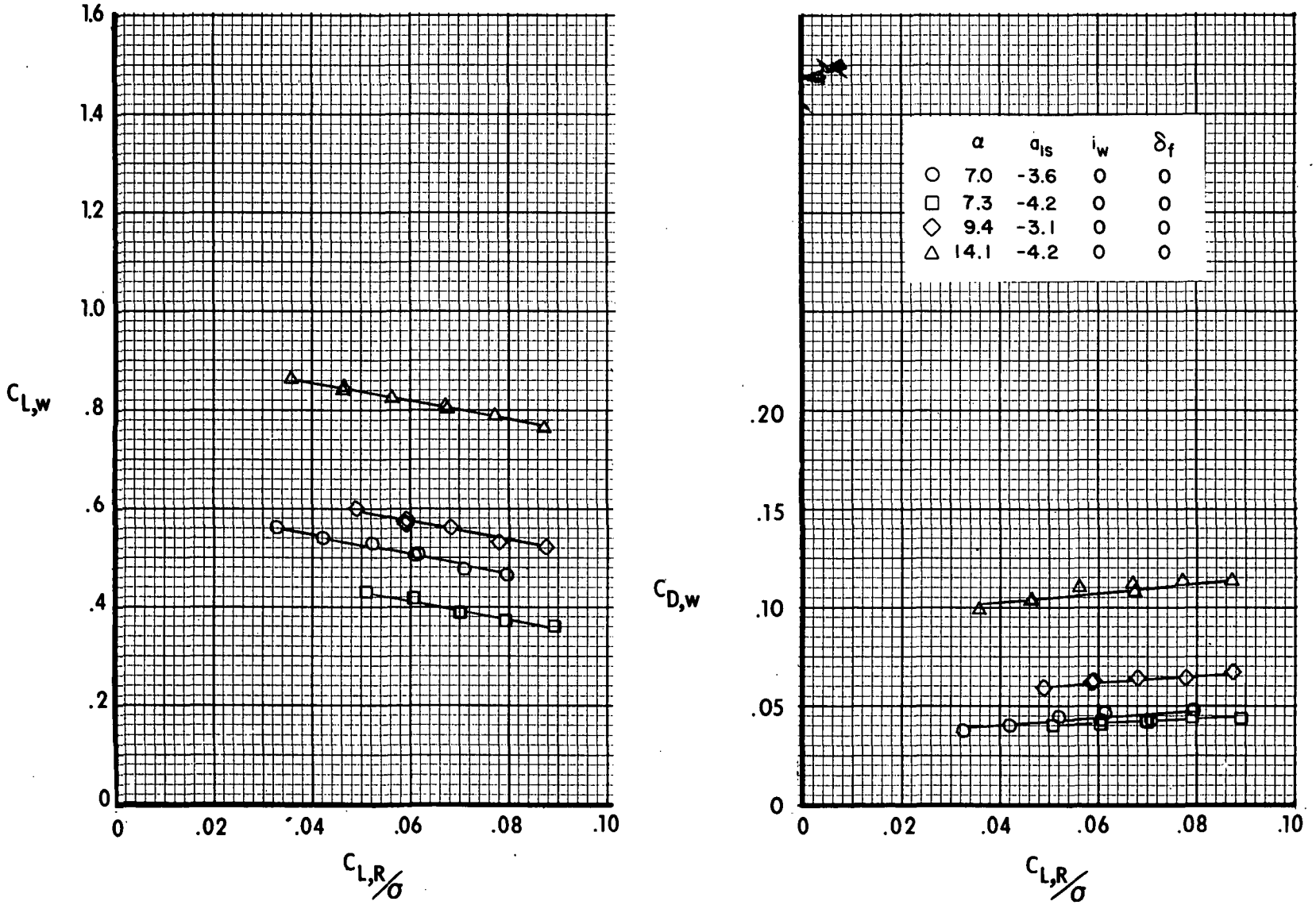

(a) $\mu = 0.14$.

Figure 19.- Variation of wing longitudinal aerodynamic characteristics with rotor lift. (Rotor collective pitch angle varied. α, a_{ls}, i_w, and δ_f are in degrees.)

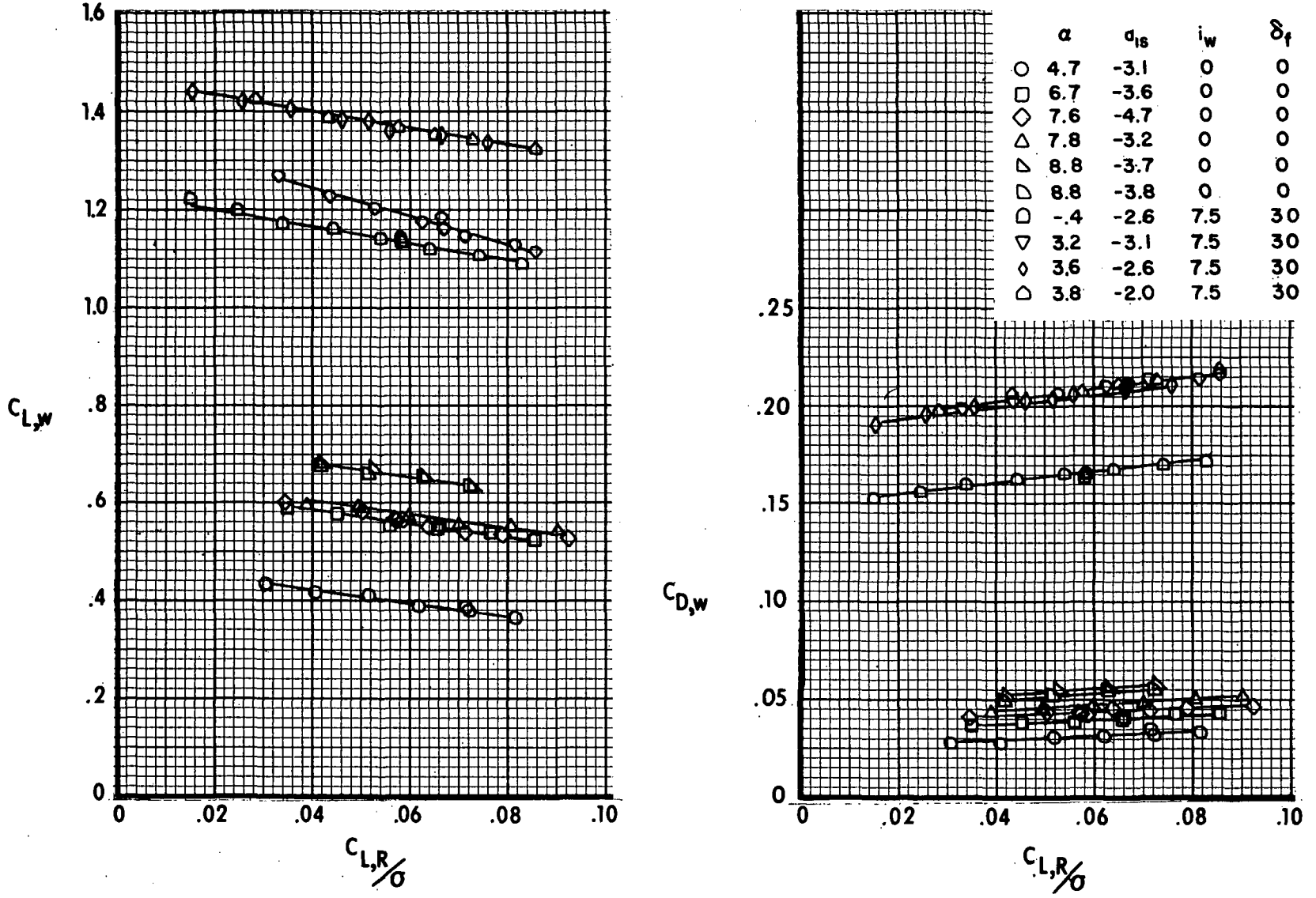

(b) $\mu = 0.20$.

Figure 19.- Continued.

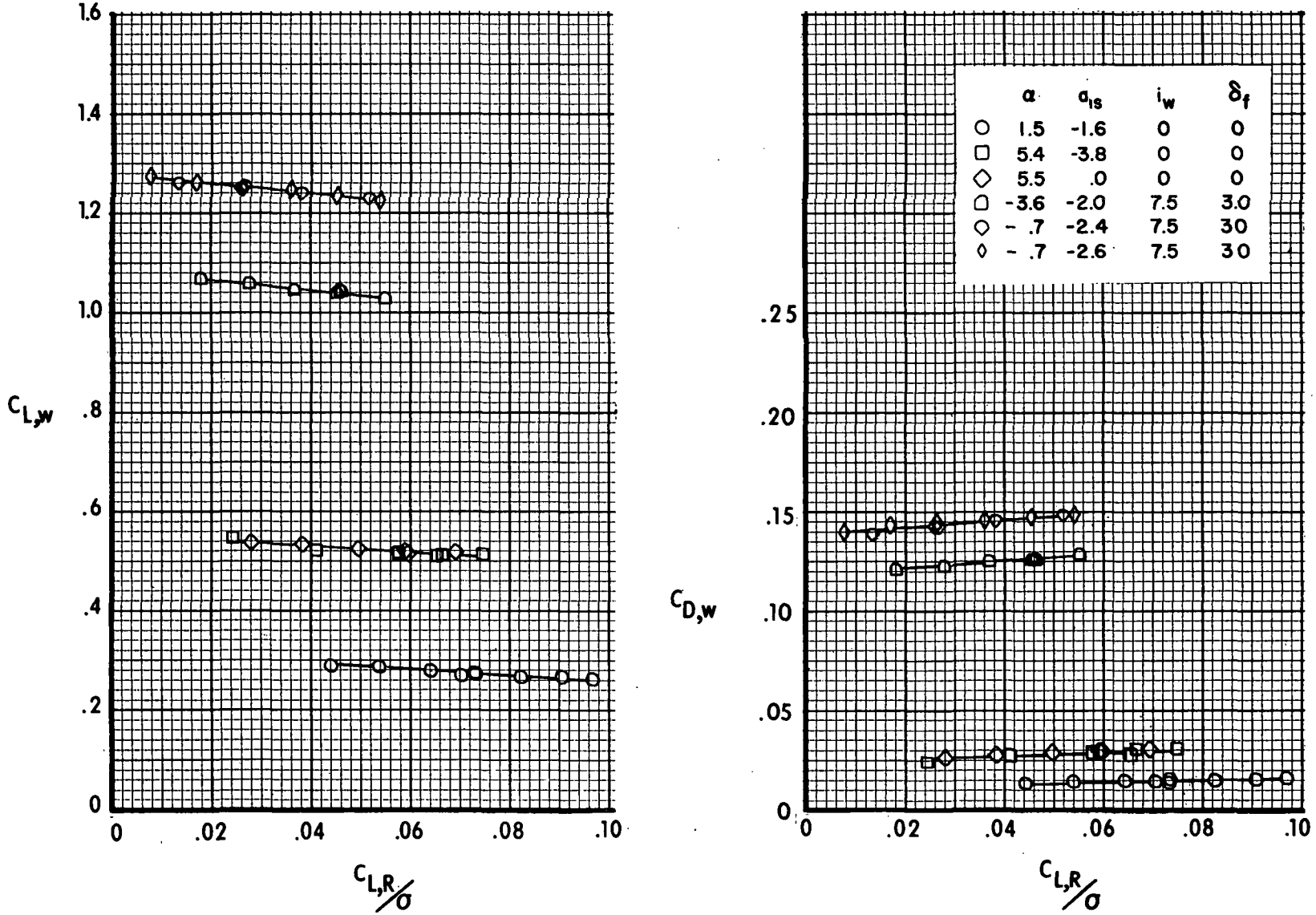

(c) $\mu = 0.27$.

Figure 19.- Continued.

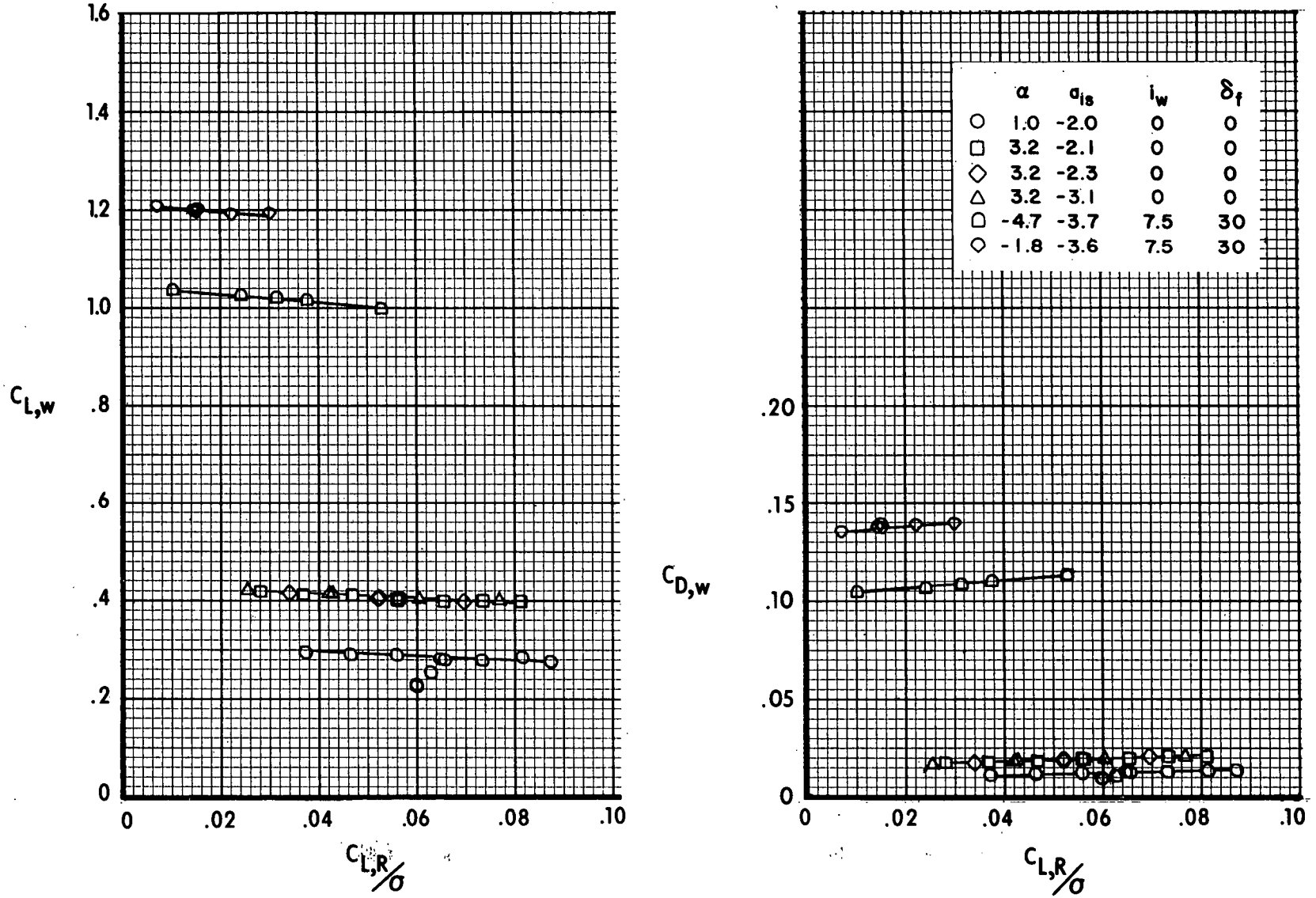

(d) $\mu = 0.32$.

Figure 19.- Concluded.

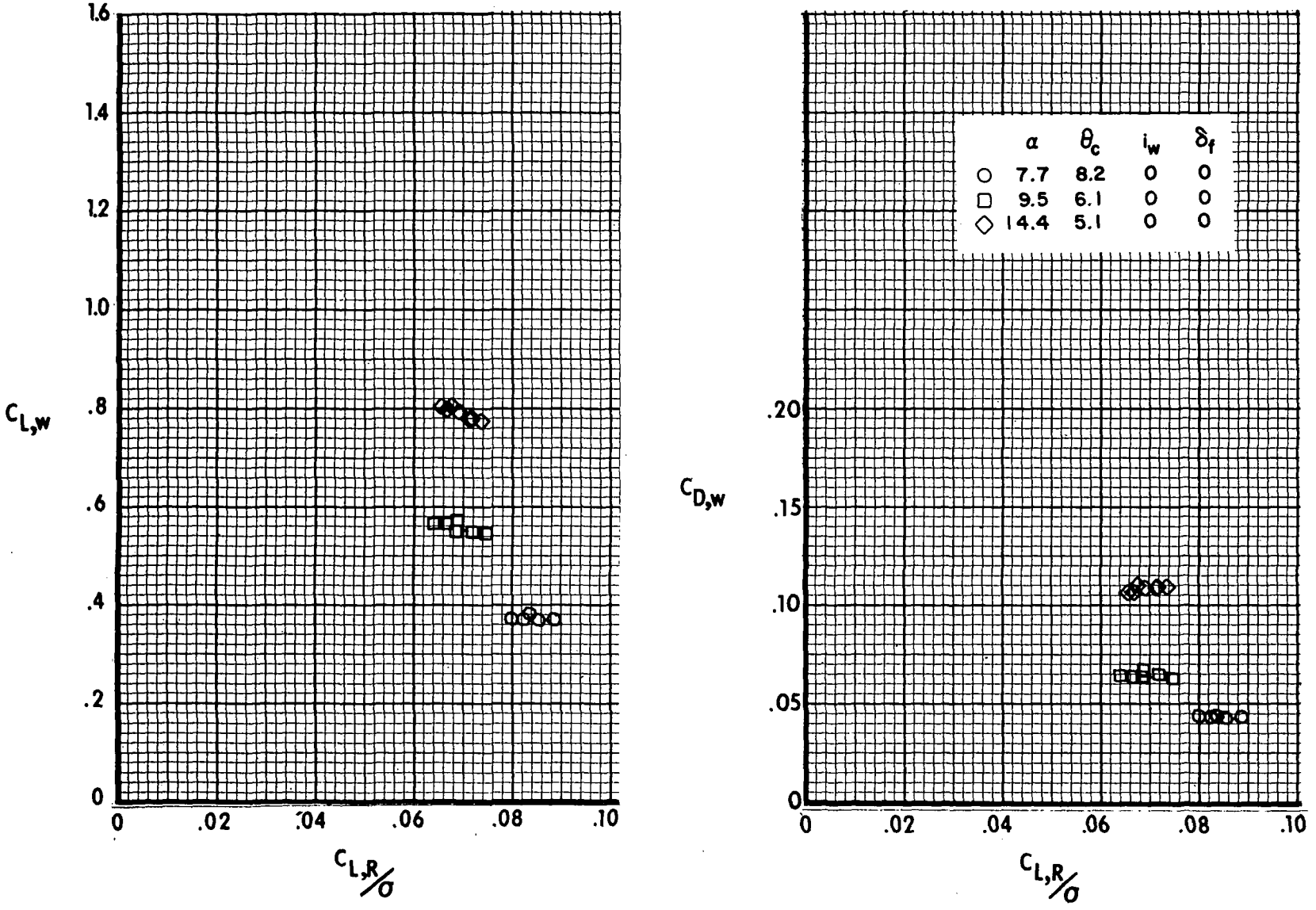

(a) $\mu = 0.14$.

Figure 20.- Variation of wing longitudinal aerodynamic characteristics with rotor lift. (Rotor longitudinal flapping varied. α, θ_c, i_w, and δ_f are in degrees.)

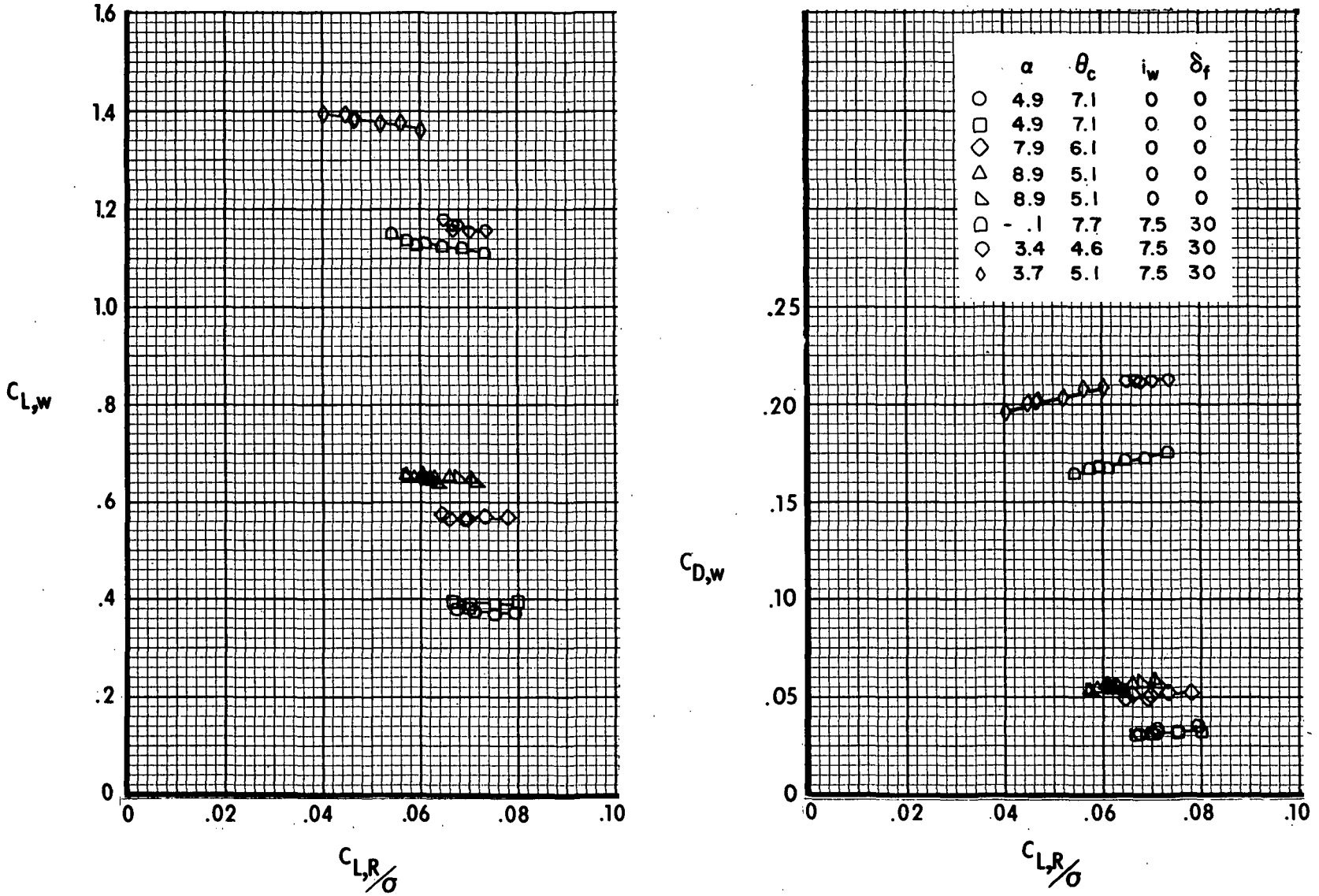

(b) $\mu = 0.20$.

Figure 20.- Continued.

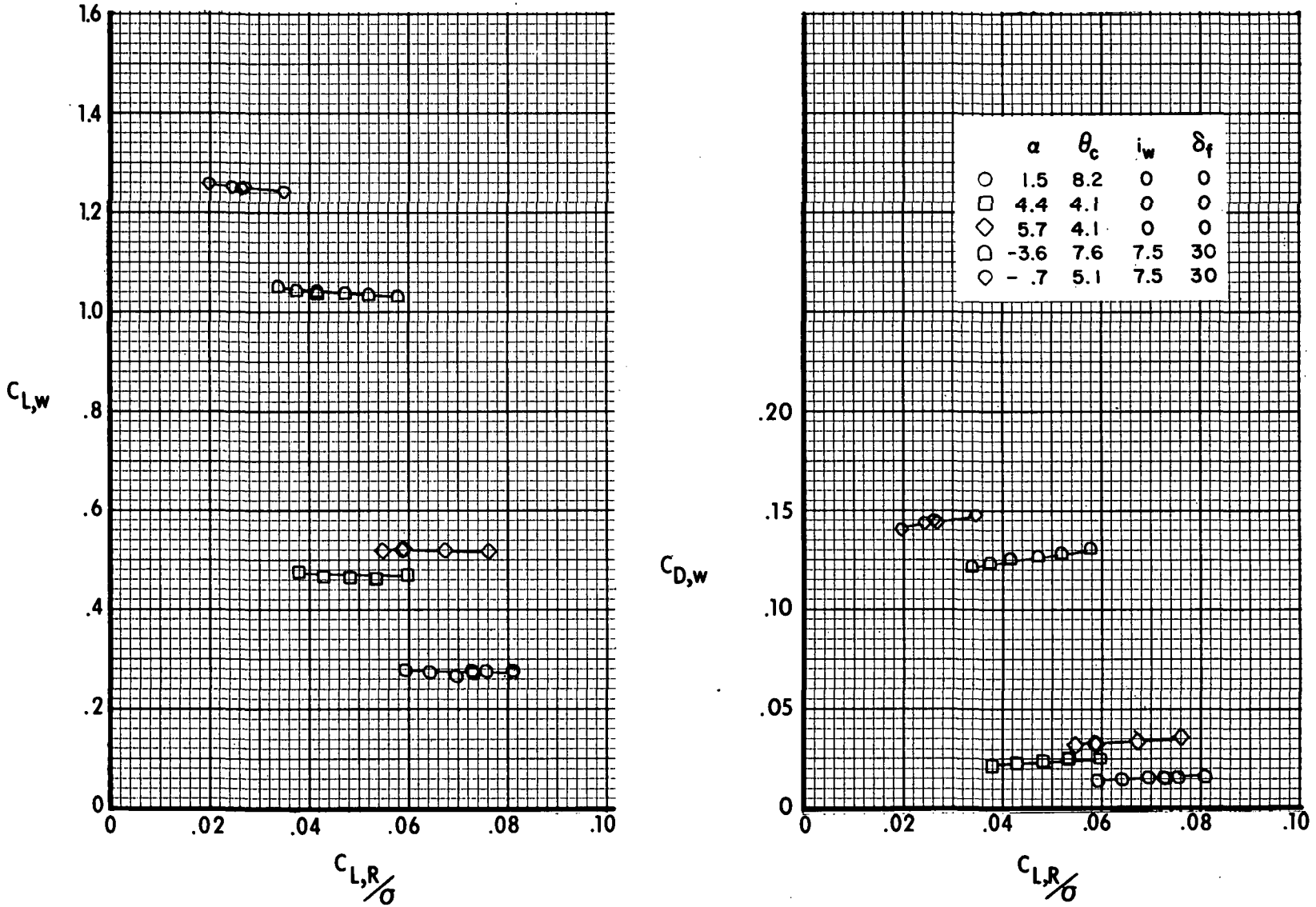

(c) $\mu = 0.27$.

Figure 20.- Continued.

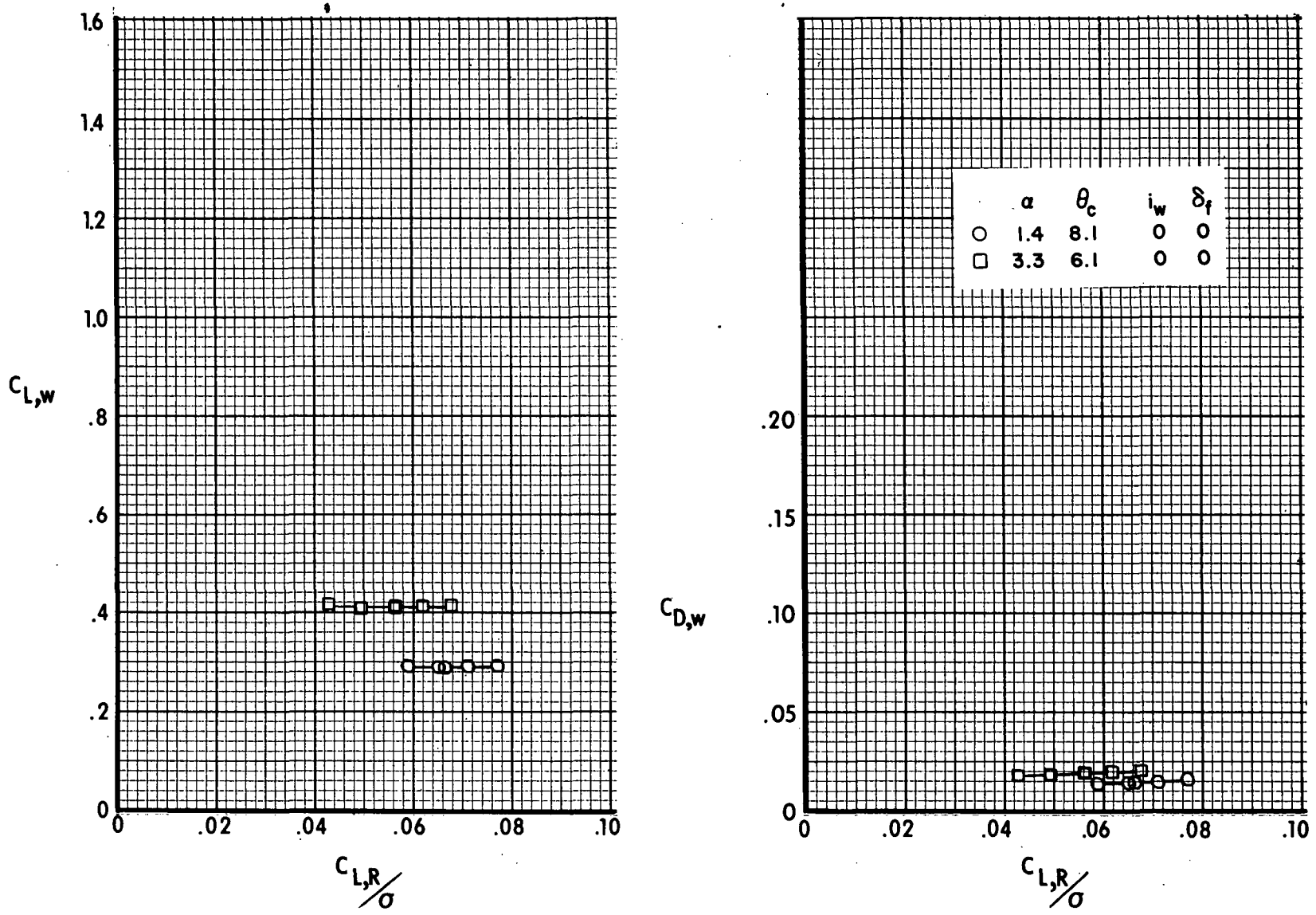

(d) $\mu = 0.32$.

Figure 20.- Concluded.

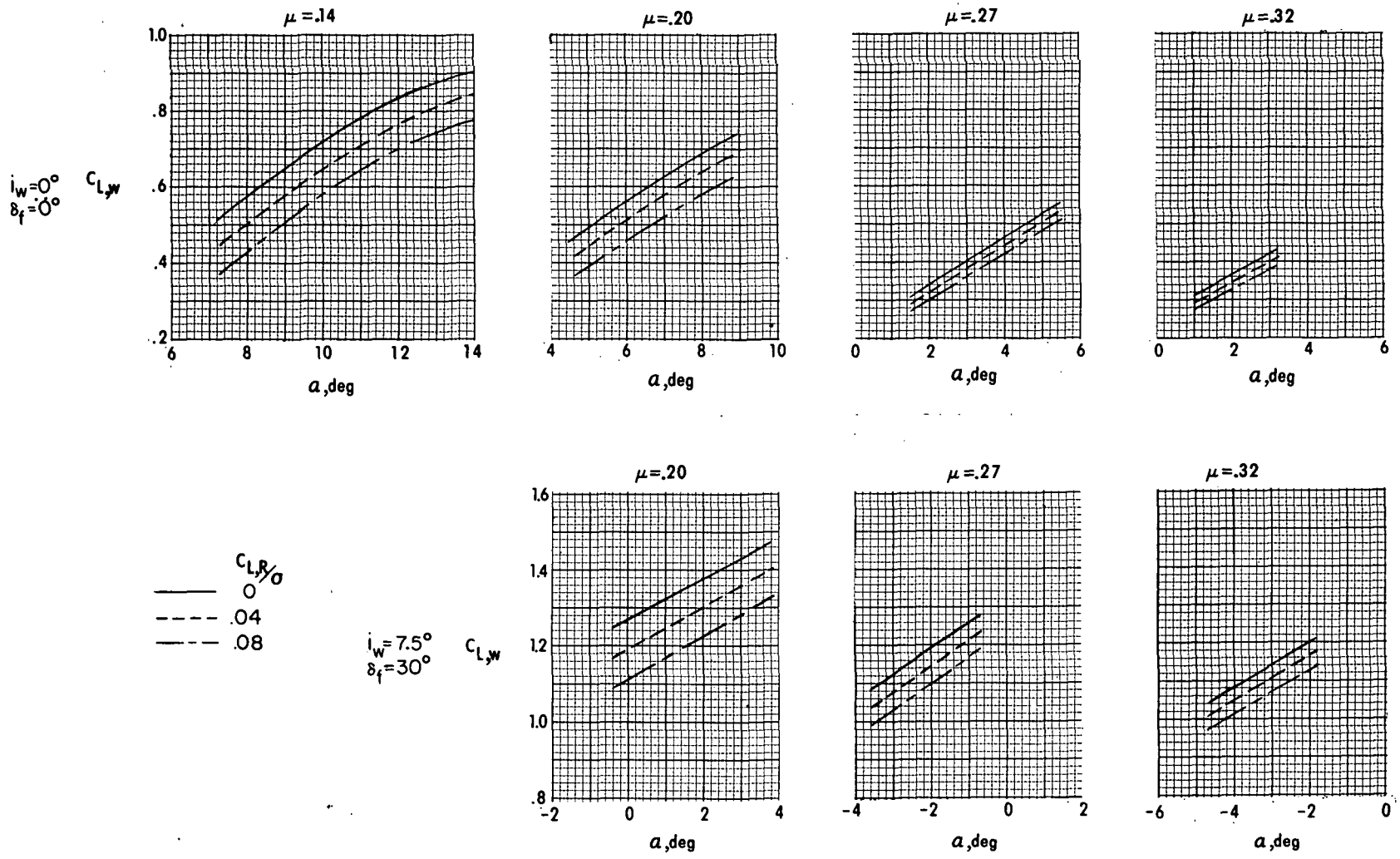

Figure 21.- Effect of rotor lift on wing lift coefficient. (Rotor collective pitch varied.)

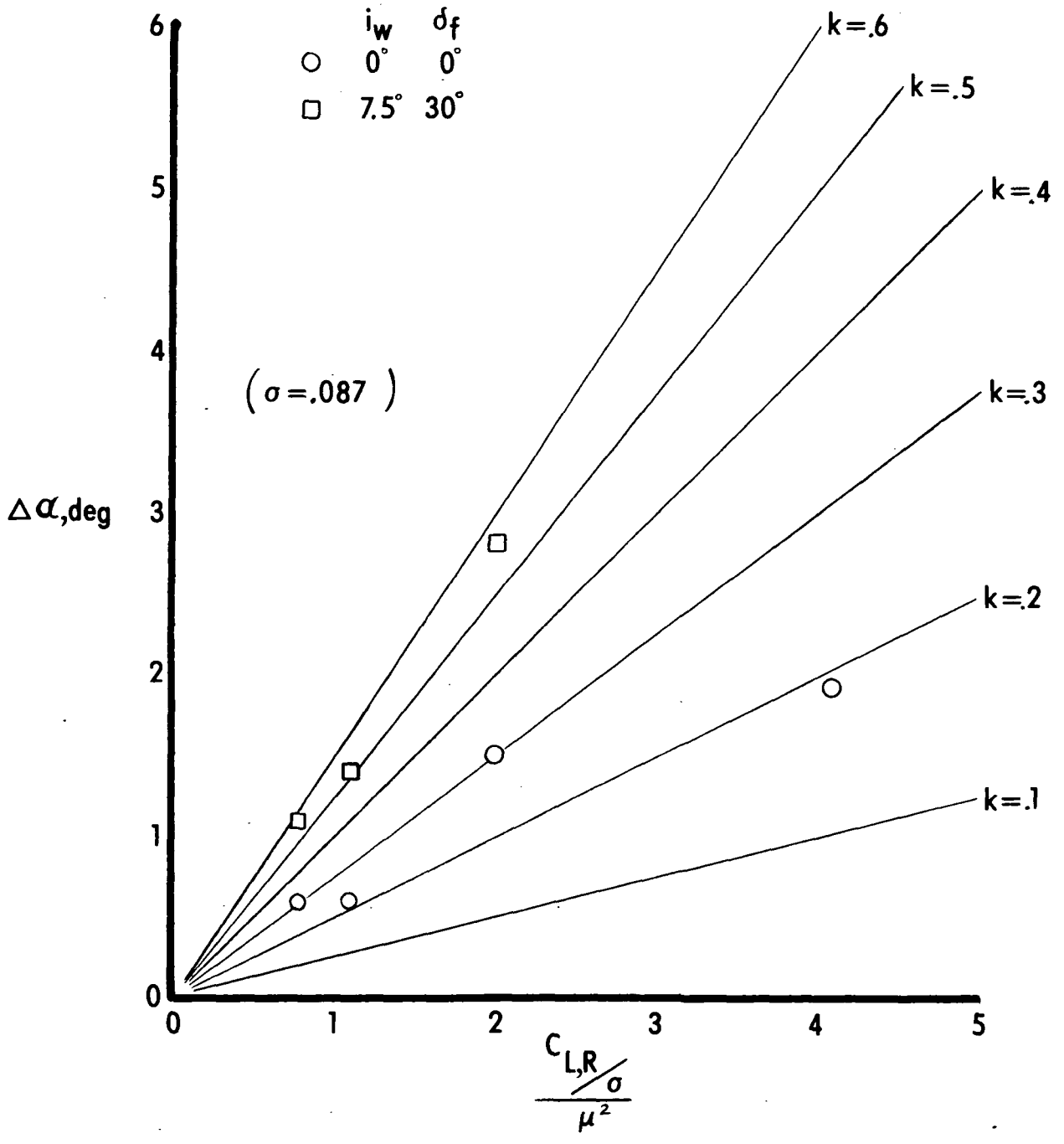

Figure 22.- Variation of change in wing angle of attack with $\frac{C_{L,R}/\sigma}{\mu^2}$.

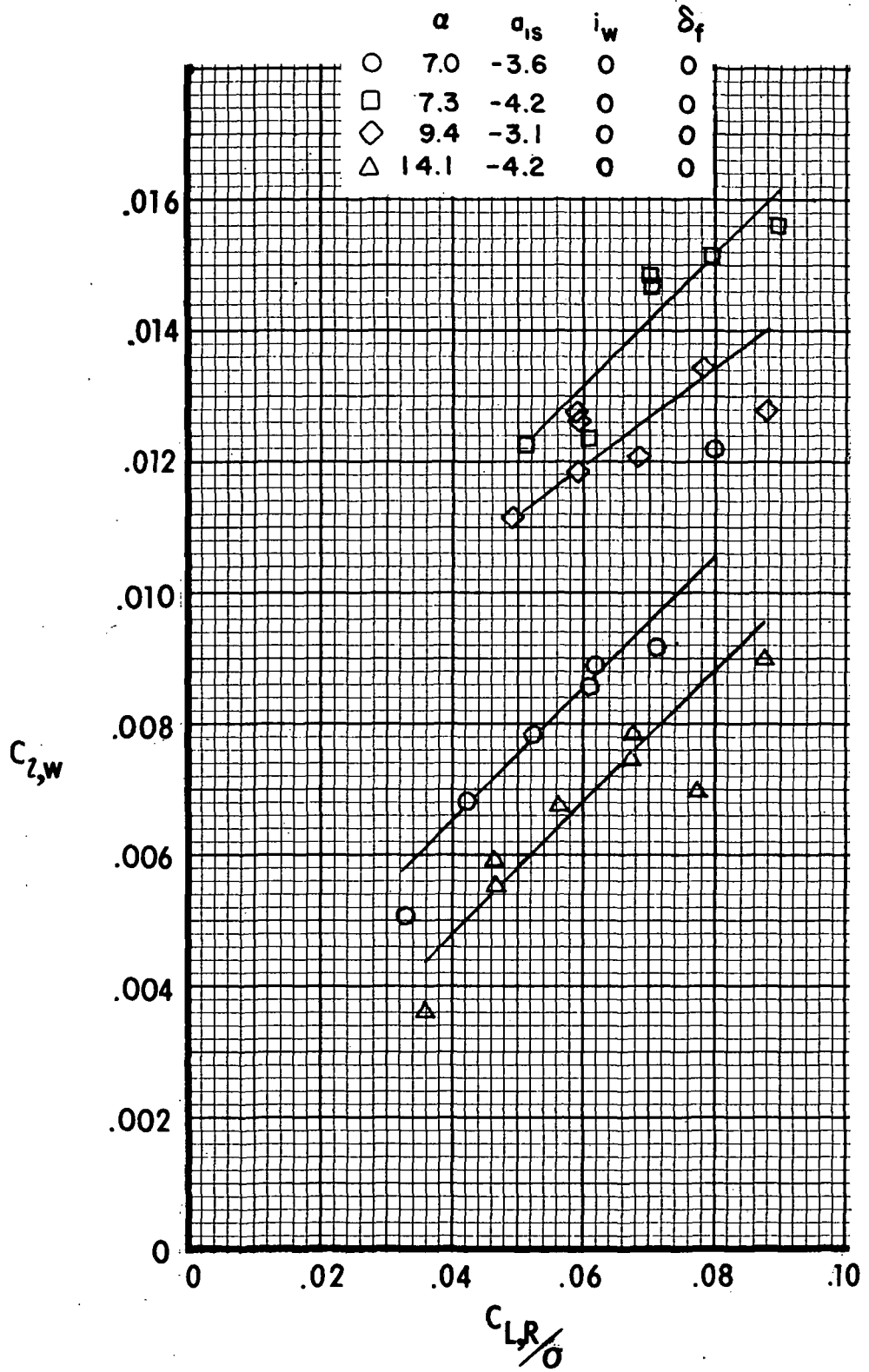

(a) $\mu = 0.14$.

Figure 23.- Variation of wing rolling-moment coefficient with rotor lift. (Rotor collective pitch angle varied. α, a_{ls}, i_w, and δ_f are in degrees.)

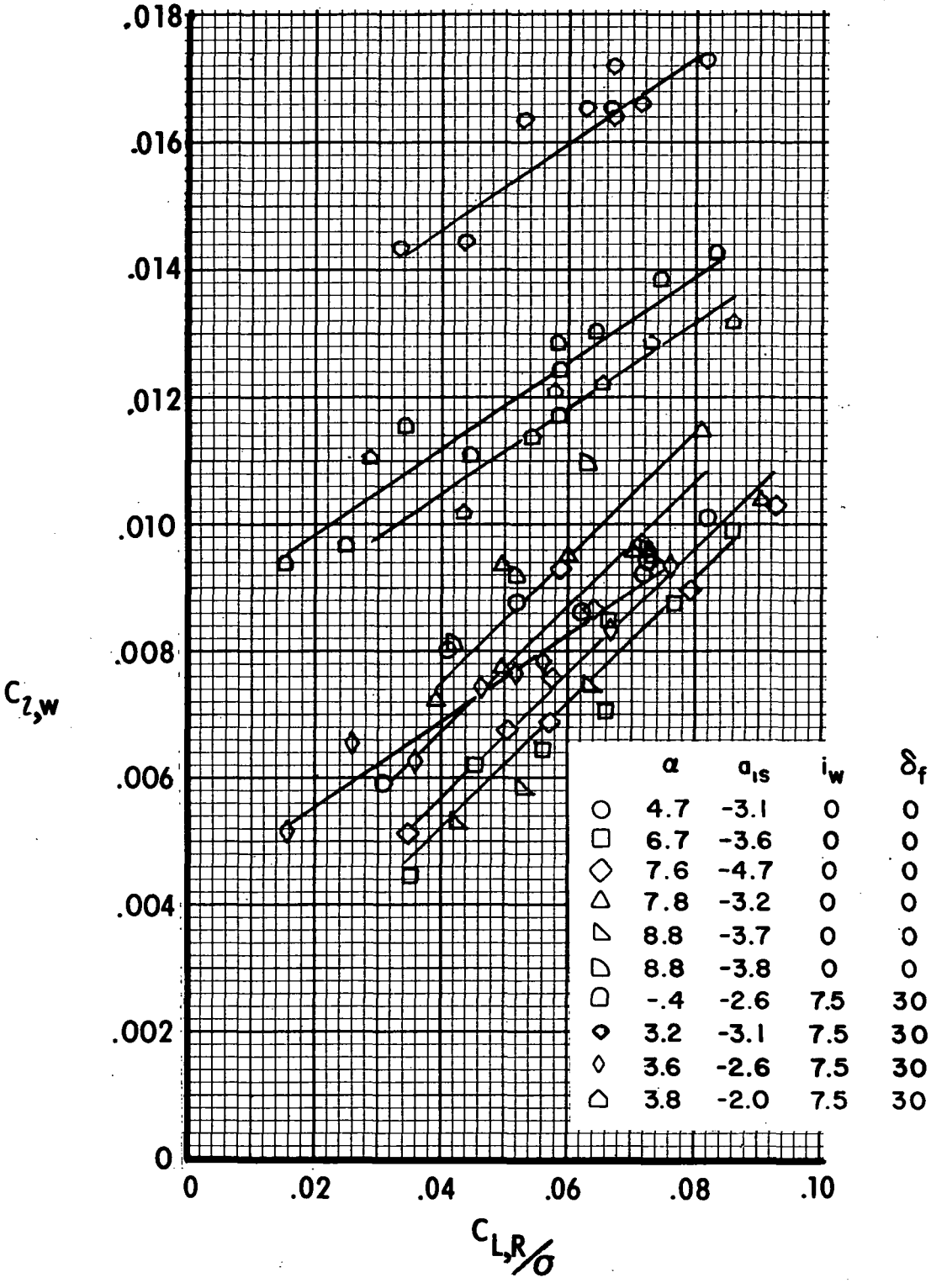

(b) $\mu = 0.20$.

Figure 23.- Continued.

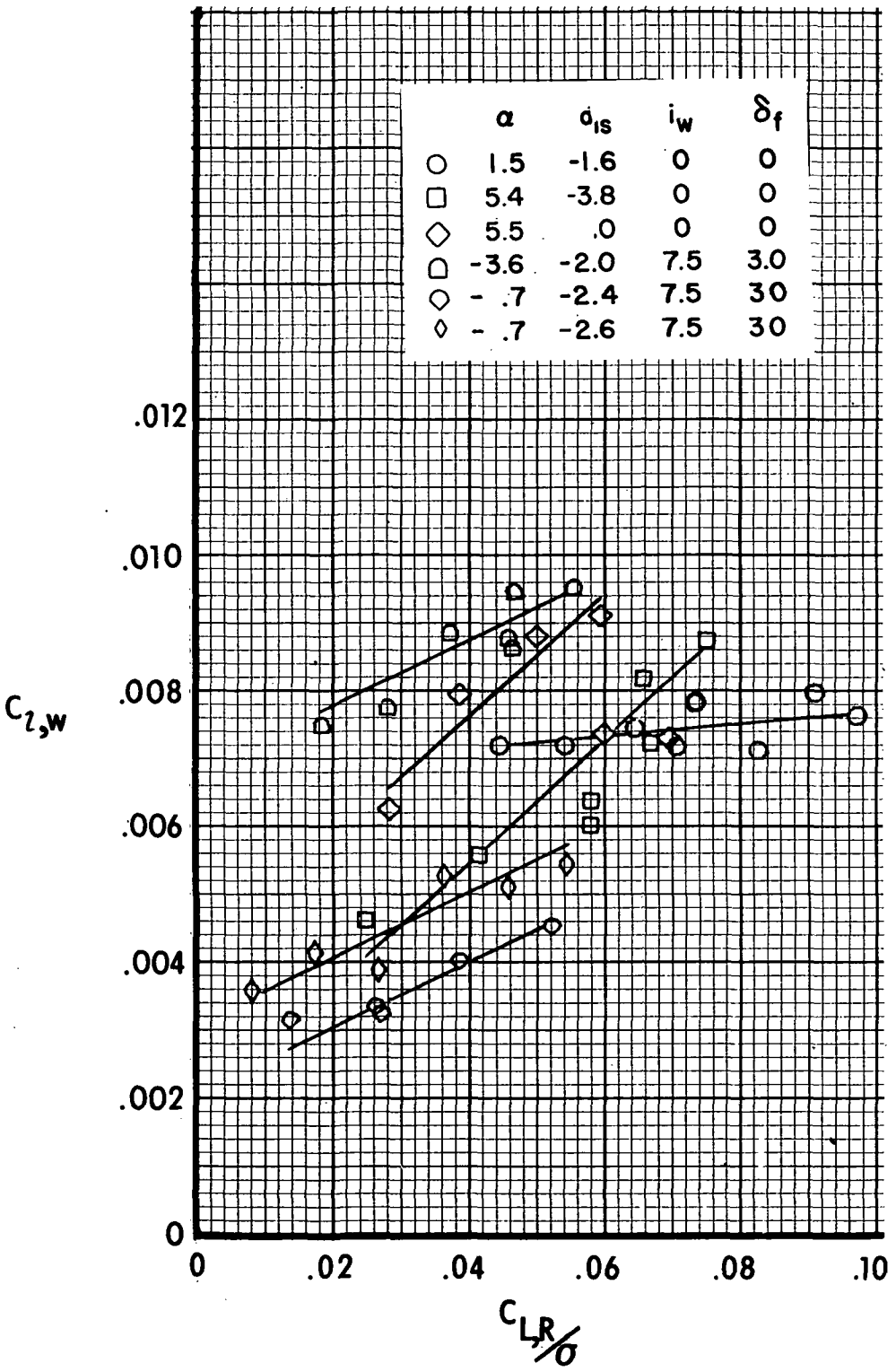

(c) $\mu = 0.27$.

Figure 23.- Continued.

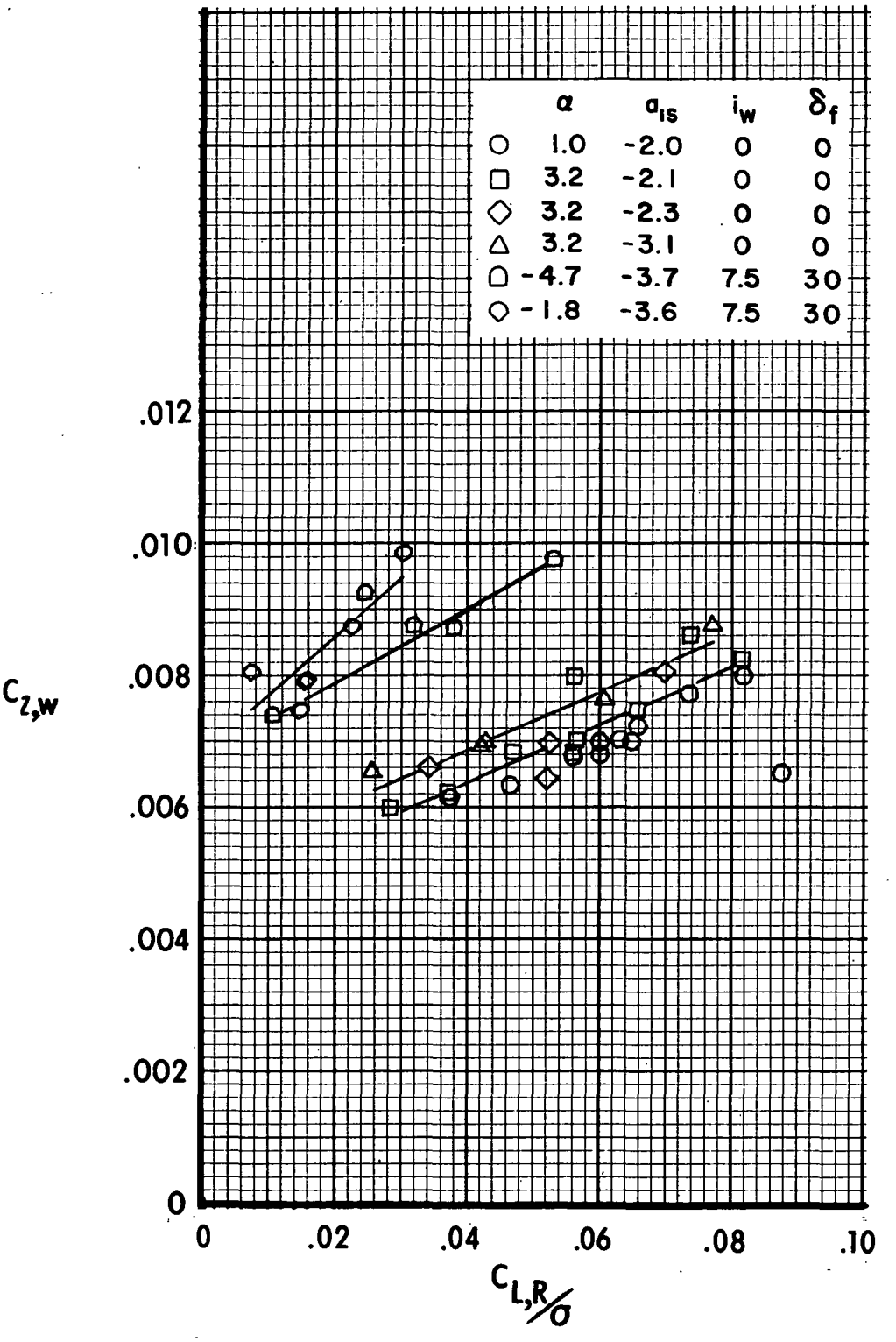

(d) $\mu = 0.32$.

Figure 23.- Concluded.

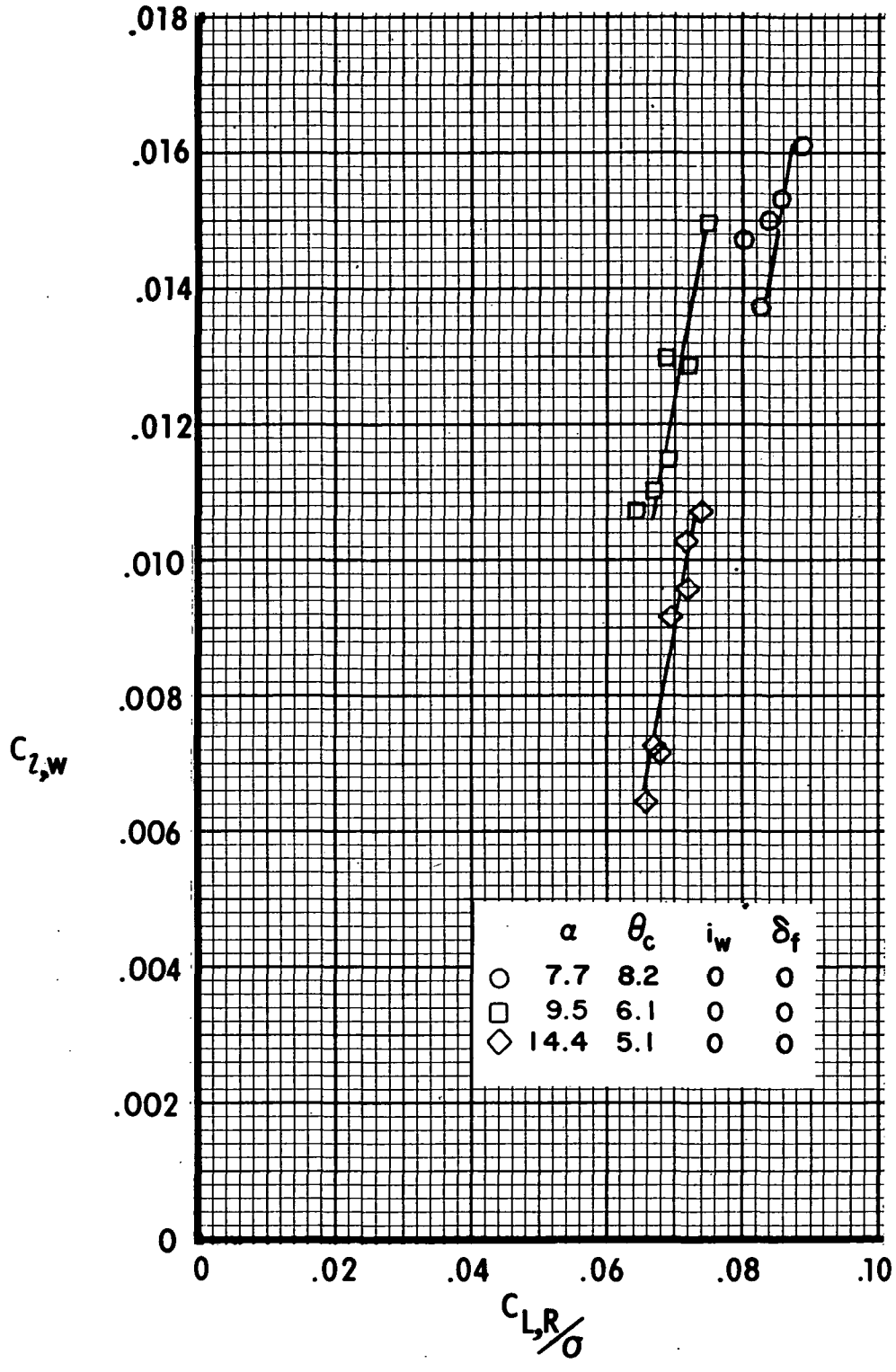

(a) $\mu = 0.14$.

Figure 24.- Variation of wing rolling-moment coefficient with rotor lift. (Longitudinal rotor flapping varied. α, θ_c, i_w, and δ_f are in degrees.)

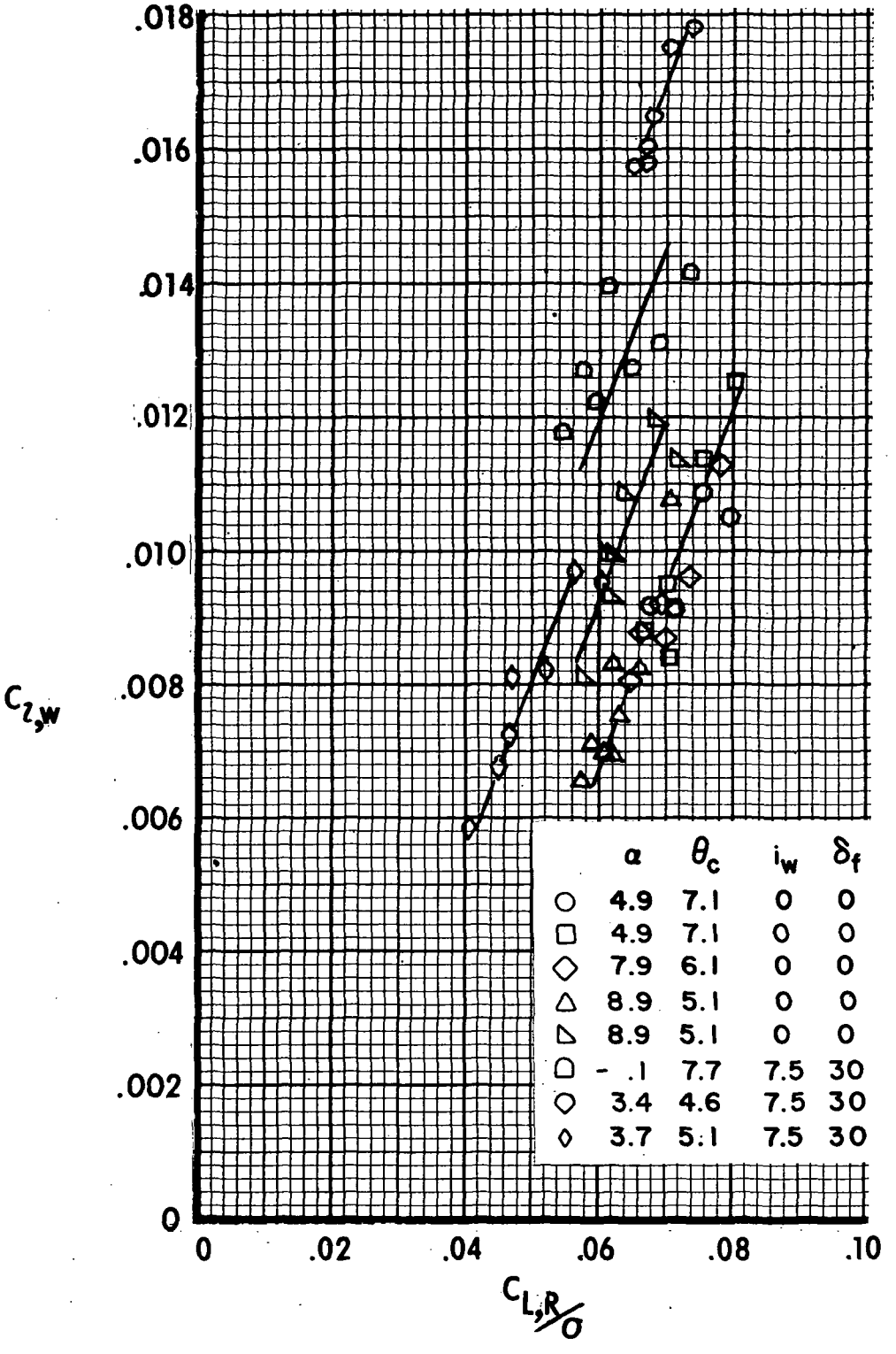

(b) $\mu = 0.20$.

Figure 24.- Continued.

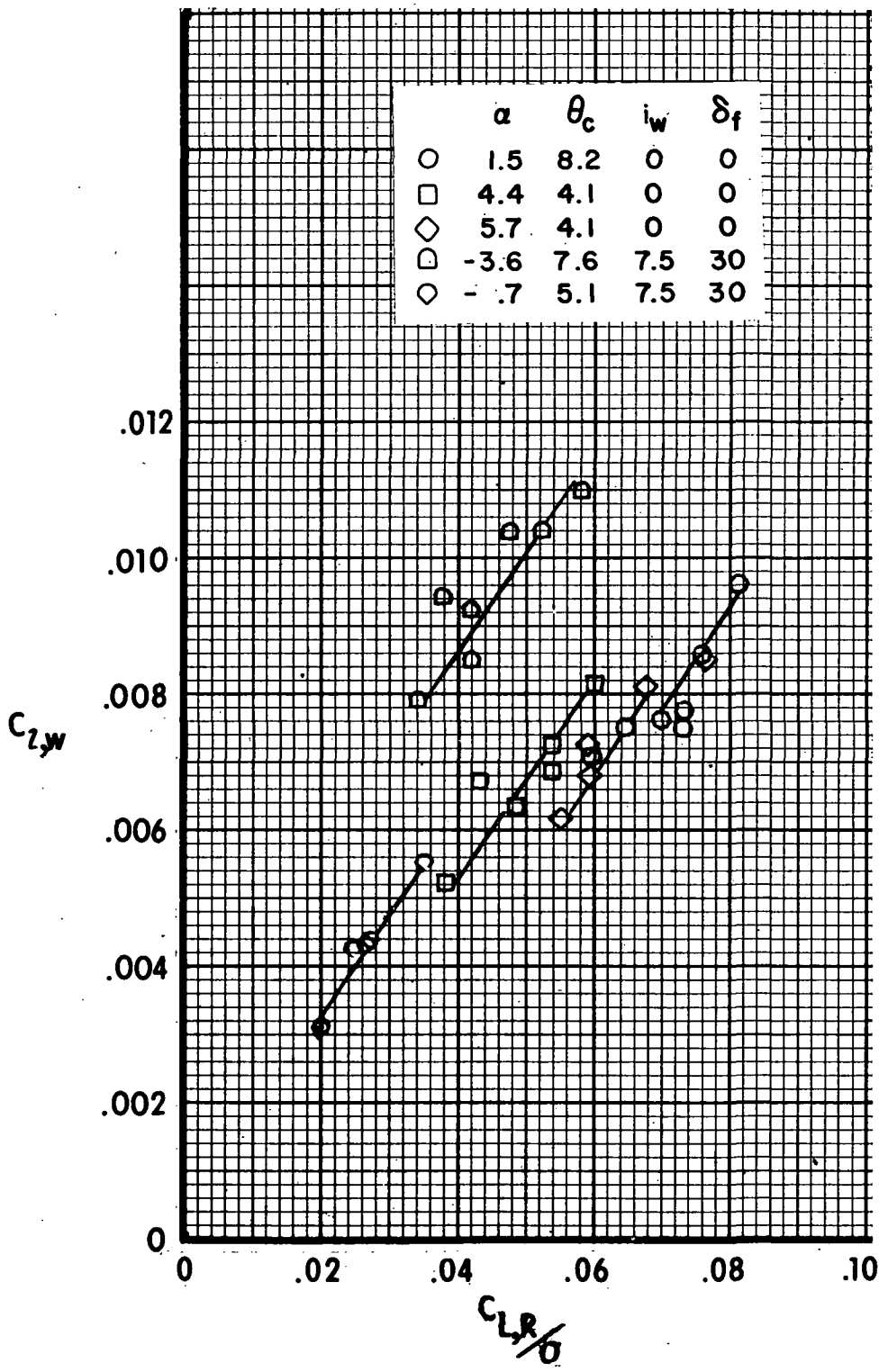

(c) μ = 0.27.

Figure 24.- Continued.

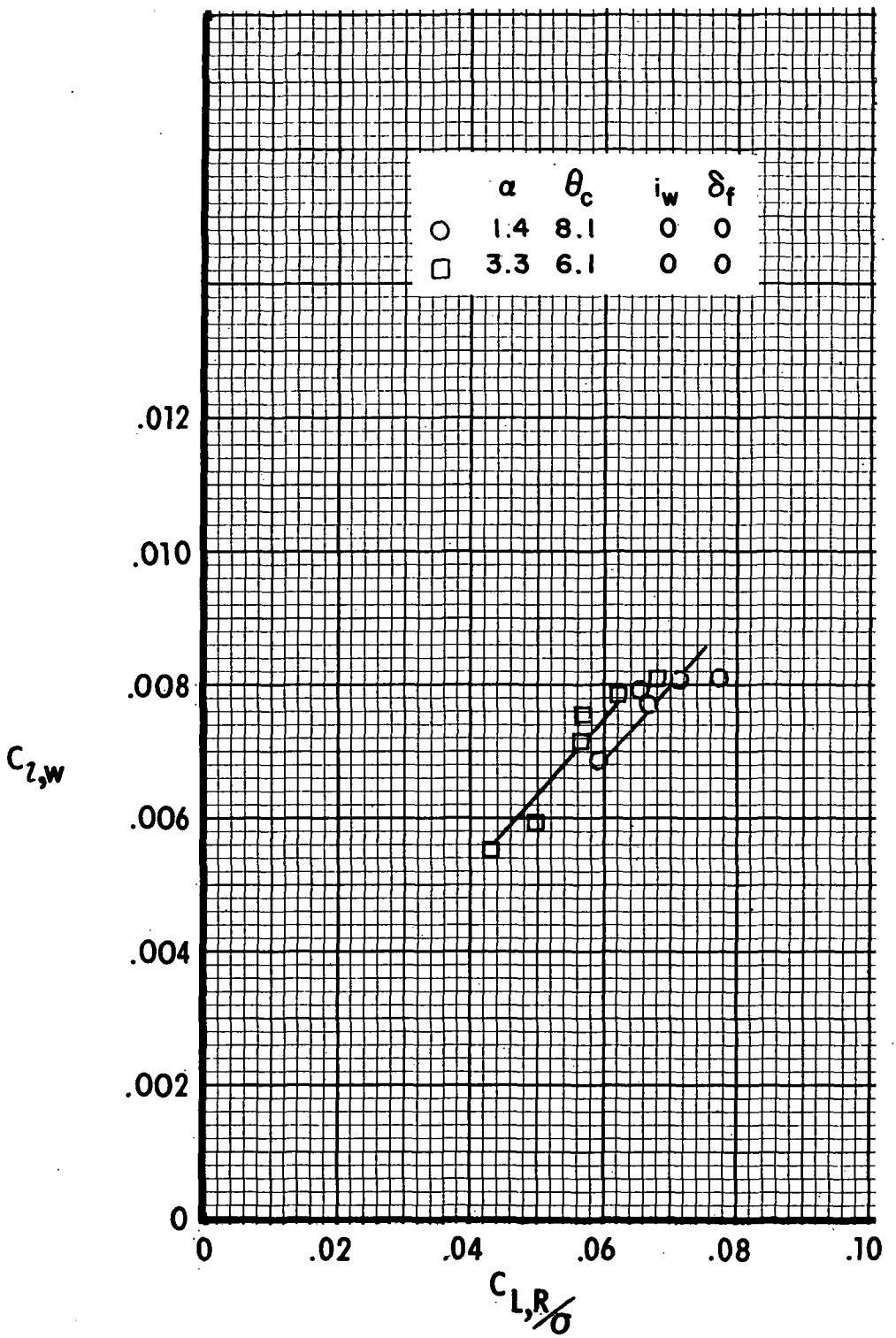

(d) $\mu = 0.32$.

Figure 24.- Concluded.

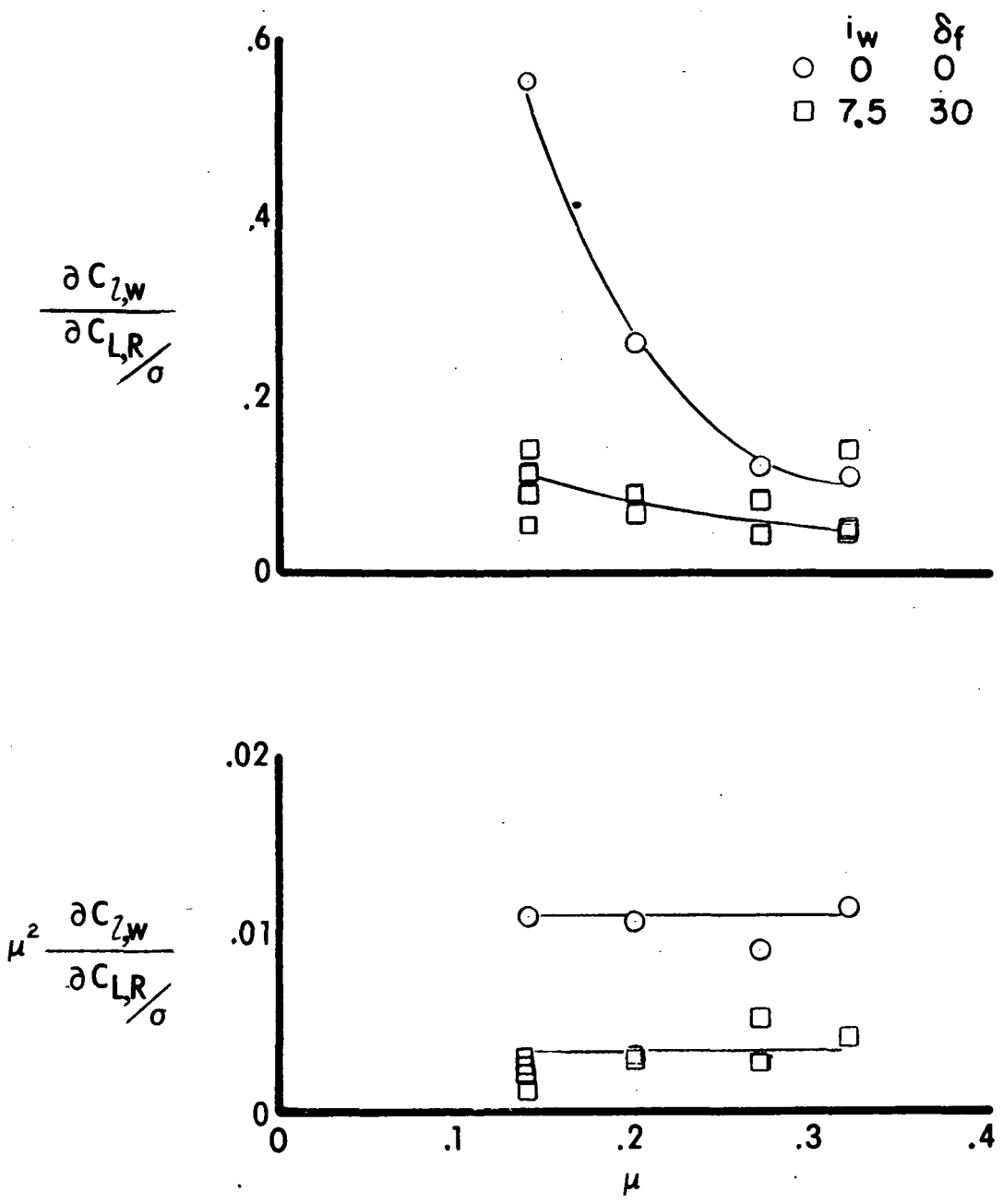

Figure 25.- Variation of wing asymmetrical loading parameter with advance ratio. (i_w and δ_f are in degrees.)

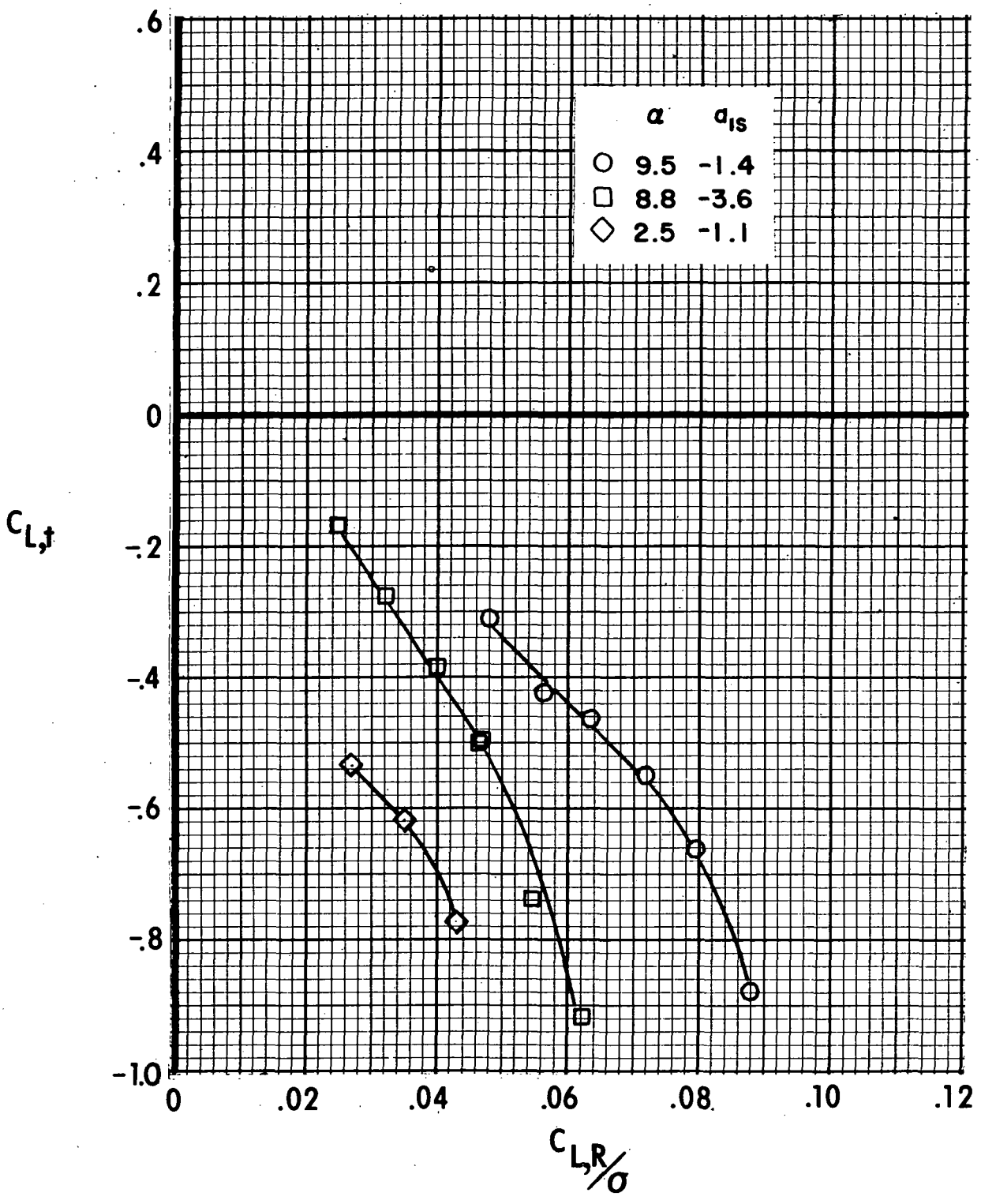

(a) $\mu = 0.07$.

Figure 26.- Variation of tail lift with rotor lift. (Wings and auxiliary thrust engines removed.) $i_t = 0^o$. (α and a_{ls} are in degrees.)

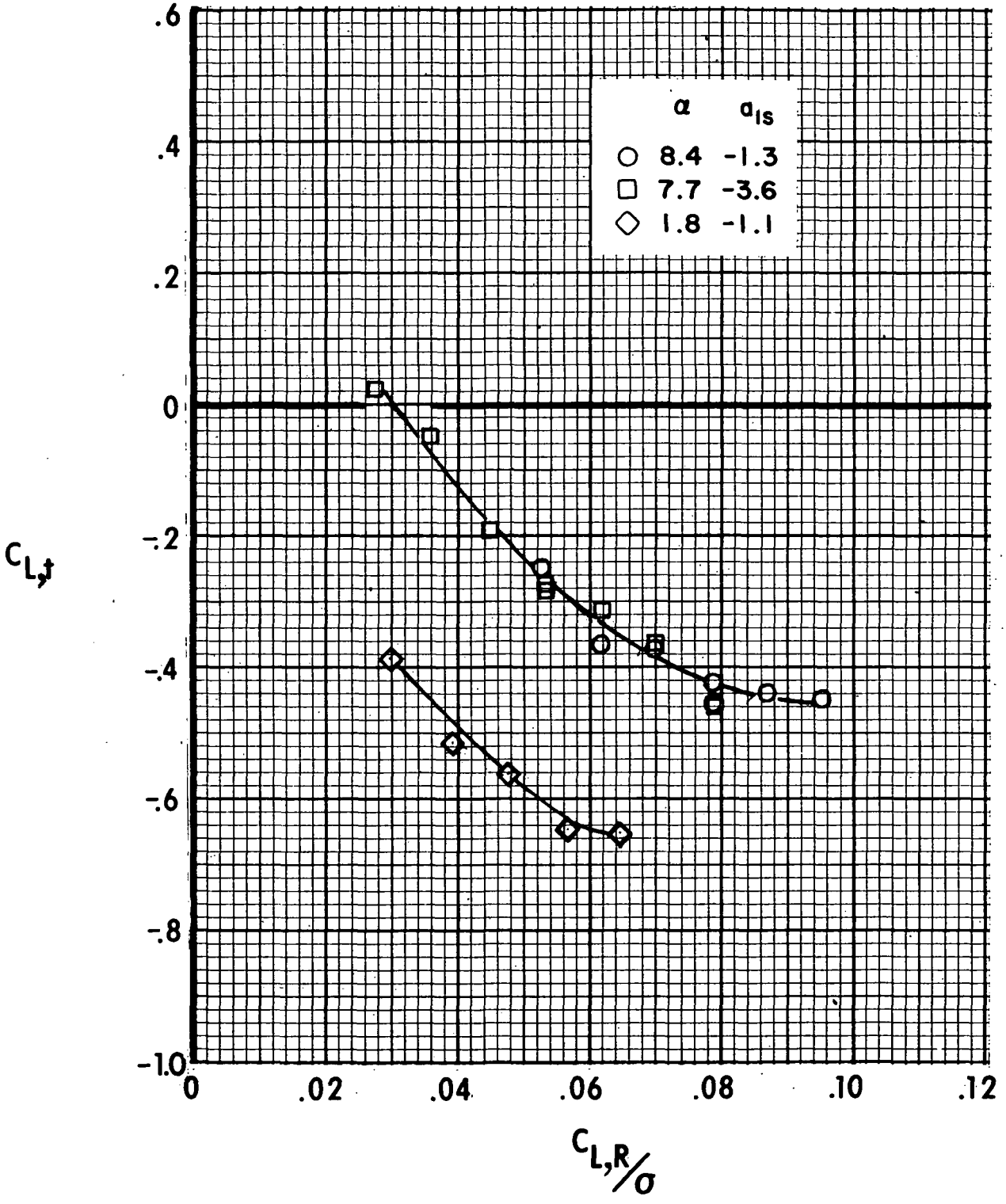

(b) $\mu = 0.10$.

Figure 26.- Continued.

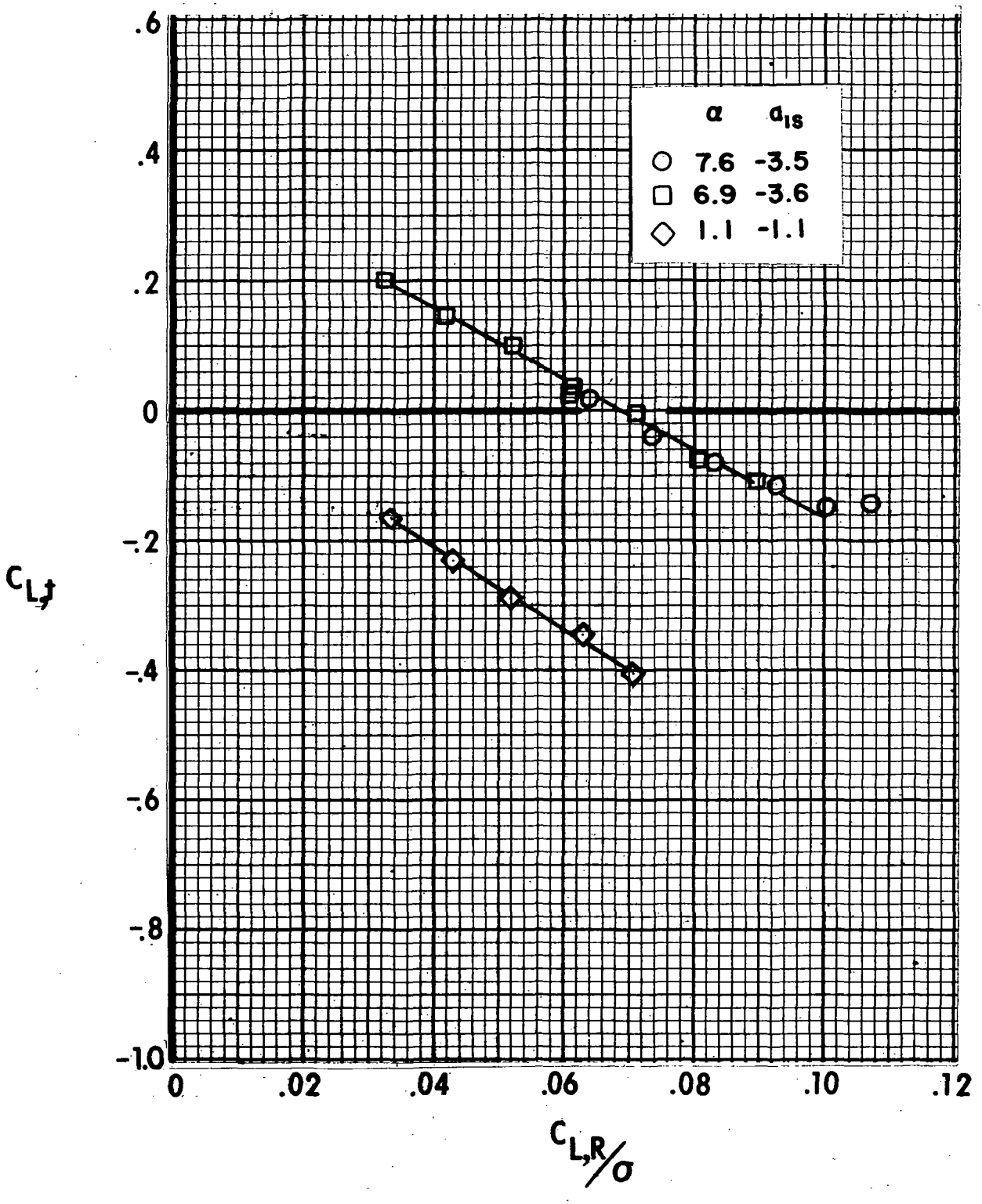

(c) $\mu = 0.14$.

Figure 26.- Continued.

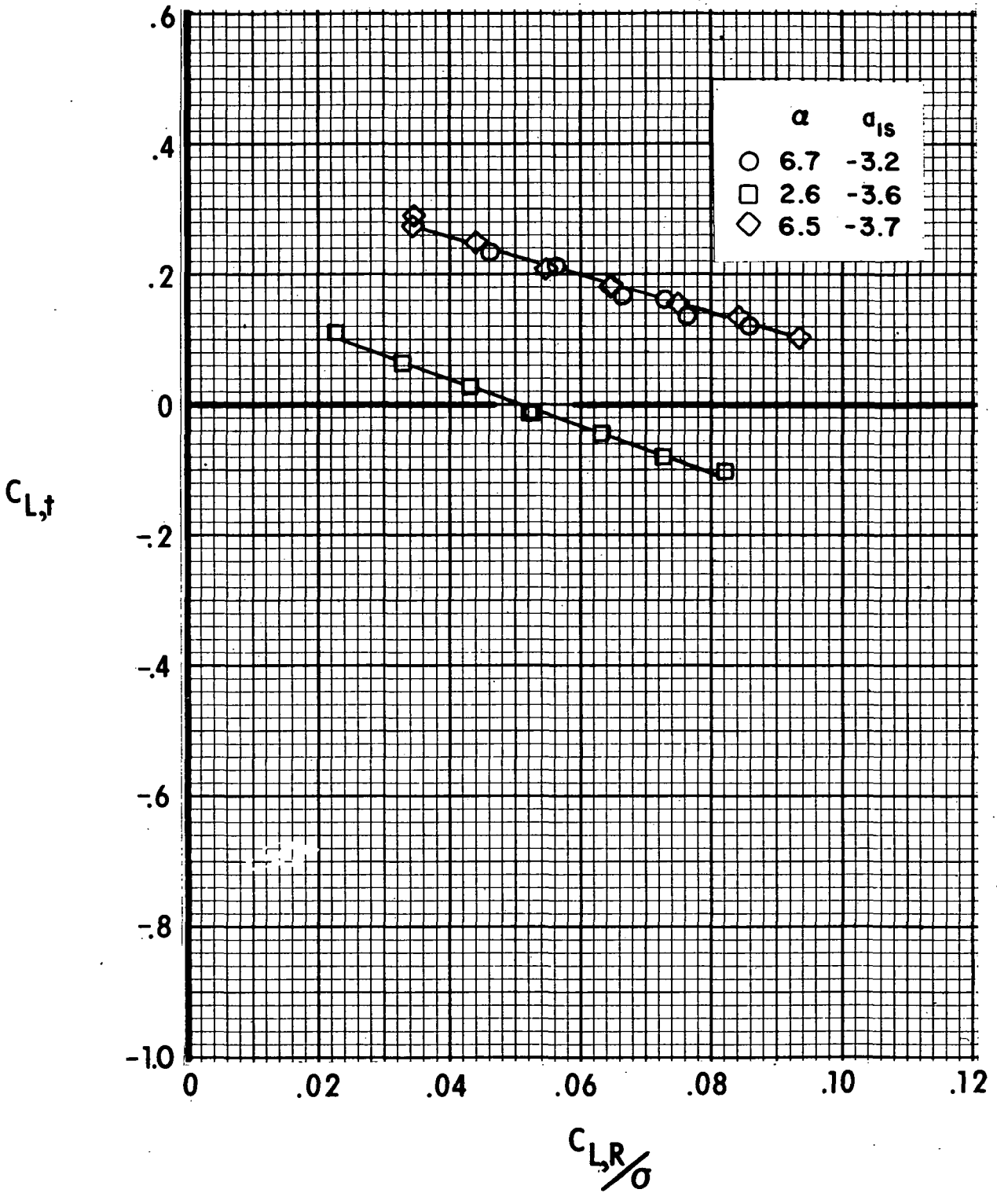

(d) $\mu = 0.20$.

Figure 26.- Continued.

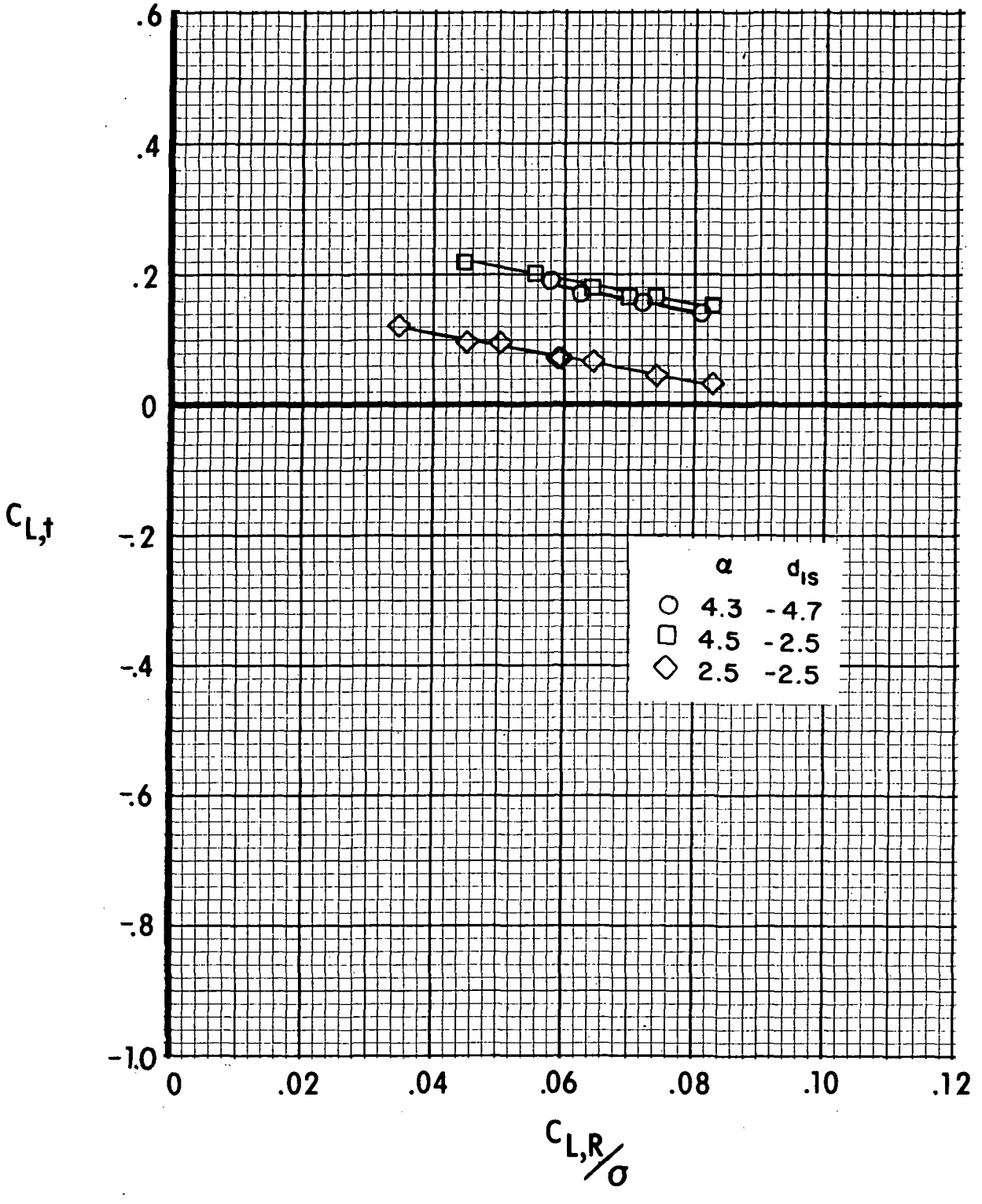

(e) $\mu = 0.27$.

Figure 26.- Concluded.

NASA-Langley, 1977 L-11515

NATIONAL AERONAUTICS AND SPACE ADMINISTRATION
WASHINGTON, D.C. 20546

OFFICIAL BUSINESS
PENALTY FOR PRIVATE USE $300

THIRD-CLASS BULK RATE

POSTAGE AND FEES PAID
NATIONAL AERONAUTICS AND
SPACE ADMINISTRATION
451

U.S.MAIL

POSTMASTER: If Undeliverable (Section 158 Postal Manual) Do Not Return

"The aeronautical and space activities of the United States shall be conducted so as to contribute . . . to the expansion of human knowledge of phenomena in the atmosphere and space. The Administration shall provide for the widest practicable and appropriate dissemination of information concerning its activities and the results thereof."

—NATIONAL AERONAUTICS AND SPACE ACT OF 1958

NASA SCIENTIFIC AND TECHNICAL PUBLICATIONS

TECHNICAL REPORTS: Scientific and technical information considered important, complete, and a lasting contribution to existing knowledge.

TECHNICAL NOTES: Information less broad in scope but nevertheless of importance as a contribution to existing knowledge.

TECHNICAL MEMORANDUMS: Information receiving limited distribution because of preliminary data, security classification, or other reasons. Also includes conference proceedings with either limited or unlimited distribution.

CONTRACTOR REPORTS: Scientific and technical information generated under a NASA contract or grant and considered an important contribution to existing knowledge.

TECHNICAL TRANSLATIONS: Information published in a foreign language considered to merit NASA distribution in English.

SPECIAL PUBLICATIONS: Information derived from or of value to NASA activities. Publications include final reports of major projects, monographs, data compilations, handbooks, sourcebooks, and special bibliographies.

TECHNOLOGY UTILIZATION PUBLICATIONS: Information on technology used by NASA that may be of particular interest in commercial and other non-aerospace applications. Publications include Tech Briefs, Technology Utilization Reports and Technology Surveys.

Details on the availability of these publications may be obtained from:

SCIENTIFIC AND TECHNICAL INFORMATION OFFICE

NATIONAL AERONAUTICS AND SPACE ADMINISTRATION

Washington, D.C. 20546